From individual to collective motion of self-propelled particles: The role of particle shape, orientational ordering and clustering

vorgelegt von Diplom-Physiker

Fernando Peruani

aus Buenos Aires, Argentinien

Von der Fakultät II - Mathematik und Naturwissenschaften
der Technischen Universität Berlin
zur Erlangung des akademischen Grades
Doktor der Naturwissenschaften
Doctor rerum naturalium

genehmigte Dissertation

Promotionsausschuss:

Vorsitzender: Prof. Dr. E. Sedlmayr

Berichter/Gutachter: Prof. Dr. M. Bär (Physikalische Technische Bundesanstalt)

Berichter/Gutachter: Prof. Dr. H. Engel

Tag der wissenschaftlichen Aussprache: 14. Januar 2008

Berlin 2008
D 83

Abstract

Self-propelled particles (SPPs) are non-equilibrium systems and as such they are not forced to obey the fluctuation-dissipation theorem. Moreover, SPPs can exhibit fluctuations in the direction of motion uncorrelated from those in the speed. In this Thesis it is shown that uncorrelated fluctuations lead to a non-Brownian motion characterized by expressions for the mean square displacement and diffusion coefficient that differ from the classical results by additive corrections. It is also indicated that such effects have been observed in cell motility experiments.

Interacting SPPs represent another fascinating kind of systems with remarkable differences with equilibrium system. For instance, while in equilibrium two-dimensional systems with continuum symmetry long-range order is forbidden, SPPs can develop such long-range order. Though it is well known that two-dimensional SPPs with local polar interactions can exhibit such transition to orientational order, a recurring question refers to alternative physical mechanisms that lead to collective motion in SPPs. In this Thesis it is shown that a self-propelling force together with volume exclusion are sufficient to cause collective migration. This is clearly illustrated through a model for self-propelled rod-shaped particles. In particular, it is indicated that the emerging collective patterns depend on the particle elongation. For instance, it is shown that for a given density there is critical particle aspect ratio that triggers non-equilibrium clustering. It is also suggested that those effects might play a major role in the collective motion of gliding bacteria such as myxobacteria.

Volume exclusion represents an apolar interaction. This rises the question how the results known for SPPs with polar interactions change when the interactions become apolar. This issue is addressed in this work and it is shown that though SPPs with apolar interactions can also achieve long-range order, the character of the transition highly depends upon particle density.

Finally, it is shown that the ordering dynamics in SPPs with either polar or apolar interactions can be described with the same continuum theory.

Zusammenfassung

Diese Arbeit untersucht das Verhalten von aktiven getriebenen Teilchen, d. h. Teilchen, die sich unter Verbrauch von Energie gerichtet mit einer gegebenen Geschwindigkeit fortbewegen. Solche Teilchen sind per Definition fernab vom thermodynamischen Gleichgewicht und unterliegen daher nicht dem Fluktuations-Dissipations-Theorem. Darüber hinaus sind die Fluktuationen in der Orientierung solcher Teilchen nicht notwendigerweise mit den Fluktuationen ihrer Geschwindigkeit korreliert. In dieser Arbeit wird gezeigt, dass solche unkorrelierten Fluktuationen für einzelne Teilchen zu nicht-Brownischer Bewegung führen, bei der die analytische Ausdrücke für die mittlere quadratische Abweichung und den effektiven Diffusions-Koeffizienten sich vom klassischen Ergebnis durch additive Korrekturen unterscheiden. Diese Effekte sind unabhängig von unseren Rechnungen in Experimenten zur Bewegung von Zellen gefunden worden.

Wechselwirkende getriebene aktive Teilchen unterscheiden sich ebenfalls stark von analogen Gleichgewichtssystemen. Während zum Beispiel in zwei-dimensionalen Gleichgewichtssystemen mit kontinuierlicher Symmetrie keine langreichweitige Ordnung auftreten kann (Mermin-Wagner-Theorem), zeigen aktive Teilchen Phasenb̈ergänge zu langreichweitiger Ordnung. Bisher wurden vor allem aktive Teilchen mit polaren, ,,ferromagnetischen Wechselwirkungen untersucht. Hier werden insbesondere aktive Teilchen mit apolaren, ,,nematischen Wechselwirkungen studiert. Insbesondere wird in zweidimensionalen Simulationen gezeigt, dass aktive getriebene stäbchenförmige Teilchen, die nur aufgrund von Volumenausschluss wechselwirken, eine starke Tendenz zur Clusterbildung zeigen. Dieses Phänomen tritt weder fr isotrope aktive Teilchen noch für diffusive Stäbchen auf. Der Übergang zur Clusterbildung wird hier mit Hilfe eines Mean-Field-Modells für die Populationsdichte von Clustern verschiedener Größe analysiert. Am Übergang ändert sich die Populationsdichte von einer monotonen zu einer bimodalen Form. Clusterbildung für aktive Stäbchen tritt bei wesentlich geringeren Dichten als die nematische Ordnung fr aktive Stäbchen. Analoge Clusterbildungsphänomene werden experimentell in der kollektiven Bewegung stäbchenförmiger Bakterien auf einem Substrat beobachtet.

Volumenausschluss repräsentiert eine apolare Wechselwirkung. Im letzten Teil der Arbeit wird ein vereinfachtes stochastisches Modell für aktive getriebene Teilchen mit apolaren Wechselwirkungen abgeleitet, das auf Bewegungsregeln analog zum bekannten Vicsek-Modell für aktive getriebene Teilchen mit polarer Wechselwirkung basiert. In

diesem Modell zeigen sich in Simulationen bei kleinen Teilchendichten und abnehmenden Rauschstärke erneut die oben beschriebene Clusterbildung, während bei großen Dichten mit abnehmender Rauschstärke zunächst ein Übergang zu nematischer Ordnung bei homogener Teilchendichte beobachtet wird, auf den eine Dichteinstabilität folgt. Schließlich wird eine Molekularfeld-Theorie hergeleitet, die den Übergang zur nematischer Ordnung, der bei hoher Dichte gefunden wird, vorhersagt.

List of publications

Parts of this work were already published as

- F. Peruani, A. Deutsch, and M. Bär, Phys. Rev. E **74**, 030904(R) (2006).
- F. Peruani and Luis. G. Morelli, Phys. Rev. Lett. **99**, 010602 (2007).
- J. Starruss, F. Peruani, M. Bär, A. Deutsch, *Bacterial Swarming Driven by Rod Shape*, In A. Deutsch, L. Brusch, H. Byrne, G. de Vries and H.-P. Herzel (eds.): *Mathematical Modeling of Biological Systems, Volume I*, p. 169-181, Birkhäuser, Boston, 2007.
- F. Peruani, A. Deutsch, and M. Bär, to appear in European Physical Journal - Special Topics (2007).

Acknowledgments

My gratitude goes first to Markus Bär and Andreas Deutsch for the support and freedom I have enjoyed during these years that allowed me to follow my interests and points of view. I also would like to thank them for their advice, particularly for introducing me to the art of presenting results.

I also would like to extend my gratitude to Luis G. Morelli for all the infinite discussions and coffees we had during these years that have contributed so much to this Thesis. For his idealistic way of doing science, for the fun that is working with him, and for his friendship.

To Niloy Ganguly for all these years of work and friendship. For his hospitality in Kharagpur and for teaching me so many practical aspects of the scientific business. Also for encouraging and promoting generous and fruitful collaborations with his students: Bivas Mitra, Animesh Mukherjee, Abyayanda Maity, Subrata Nandi, Monojit Chaudhuri and Sanjib Sadhu. My gratitude also goes to them. Specially to Bivas Mitra with whom I have already spent near four month of intense work.

To Gustavo Sibona, Haralambos Hatzikirou and Sebastiano de Francicis for all these years of fun, coffees, work and friendship.

To Ernesto Nicola and Tobias Klauss for all the interesting discussions that have helped me so much in the development of this Thesis. To Carsten Svaneborg for all these years of priceless advise on computers and science.

To Hugues Chaté and Francesco Ginelli for recent discussions that have brought a new perspective on some of the results reported in this Thesis. To Harald Engel for accepting to be part of the Thesis committee and helping me so much with the submission to TU Berlin.

To Debasih Chaudhuri, Benjamin Linder, Simon Norrelykke, Uwe Thiele, Giovanni Meacci, Karin John, Jörn Davidsen, Tomasz Polak, Anatole Kenfack, Eduardo Altmann, Rafael Vilela, Detlef Holstein, and Stefan Palzer from the Max Planck Institute for Complex Systems, and David Basanta, Jörn Starruss, Michael Kücken, Lutz Brusch, Joachim Peter, Marco Tektonidis, Anja Voss-Böhme, Perla Zerial, and Edward Flach from TU Dresden, and present and former colleagues, for their helpfulness and creating such a pleasant atmosphere. To Claudia Pönisch, Katrin Lantsch, Sabine Vollheim and Jenny Baumann for helping me surviving the German Bureaucracy.

To all friends and family that came to visit us in the cold, tiny, remote, but beautiful,

Dresden, in order of arrival, Graciela Marchueta and Claudio Tognonato, Marta Shlosberg, Vicky Salías, José Flores (also for the time we spent analyzing the Nibble game!), Diego Bendersky, Gabriela Riguetti, aunt Betty Peruani and uncle Charly Salías, Luciana Pancelli, and Juana San Román and Alejandro Peruani. To my grandmother Petra San Román for making all the way to Sanabria, and to my grandmother Femi Cabezas who insisted me in doing the PhD abroad.

To all the friends in Dresden: Uwe Börner, Torsten Goerke, Olga Acosta and Carlos Viviescas, Ayelen Coccoz and Chiara Morelli, Hyongu Kang, Parinita Samant, Evelyn and Phillipe Labadie, Mariangeles Aguirre, Merchi Moráiz, Sandra Ruíz de Trovarelli, Lina y Carlos Arregocés, León Marín, and all the rest of the ACI gang, for making my life in this Saxonian city so pleasant.

To Willy Dussel, Lidia Szczupak, Silvina Ponce Dawson, and Rita Zorzenon dos Santos for all the support and knowledge I received from them. To Mariano Mario Rodríguez, Ximena Orsi, Nicolás Furman, Mariano Mancuso, Mariano Galvagno, Guillermo Solovey, and the rest of the UBA gang who made of my undergraduate studies a pleasant time to remember.

To all the beloved ones that I left in Buenos Aires during these years. Particularly, to those who could not make it to Dresden, to my great old friend Leonardo Alvarez, Gonzalo Corrado and Hernán Fraind. To my sisters Marina and Ana Peruani (and also to my four-legs sisters Pamela and Corazon), and to my wonderful parents Alejandro Peruani and Juana San Román for all their understanding, support and love.

Finally, to Michi ”Chula” Nakashima for her enjoyable company during these years. For her understanding, support and love.

Contents

Chapter 1

Introduction

Self-propelled particles are ubiquitous in nature, and examples of them range from non-animated matter like running droplets [1–4] to living system like crawling cells [5–9]. The self-propulsion of the particles makes all these systems essentially non-equilibrium systems, and fascinating complex phenomena arise depending on the interactions. For instance, the consumption of energy involved in the propulsion mechanisms and the amount of stored energy allow these active particles to move without obeying the fluctuation-dissipation theorem [10–14]. Since these particles typically carry their own energy and do not require the environment to propel themselves, the statistical movement an ensemble of them can perform is not restricted to classical equilibrium constrains like, e.g., the ones the fluctuation-dissipation theorem imposed. Imagine, for example, a crawling cell migrating in a noise environment and compare its movement with a classical inanimated Brownian particle. The Brownian particle moves each time that gets buffeted by the noise environment, changing simultaneously its direction of motion and modulus of the speed. As it is well known, an ensemble of non-interacting Brownian particles is then well described by an Ornstein-Uhlenbeck process [15]. On the contrary, the crawling cell is subject to environmental fluctuations as well as fluctuations of its propelling engine. Consequently, fluctuations in the direction of motion and speed can follow independent stochastic processes. Moreover, an organism might change its moving direction and speed according to some stochastic processes that optimize, e.g., a random search of nutrients [16–18]. In addition, it has been clearly shown in experiments that the actual random movement exhibited by many microorganisms [5, 7, 9] and animals [19] does not obey a classical Brownian motion. To interpret and understand such experiments it is necessary to rely on a correct phenomenological description of the motion of the organism

which should account for the observed statistical data [20] like fluctuations in the speed and in the direction of motion. Chapter 2 is devoted to non-interacting self-propelled particles and addresses this issue. Particularly, it will be shown that when fluctuations in the speed are uncorrelated with fluctuations in the direction of motion, there are additive corrections to the classical Brownian motion theory for the mean position and mean square displacement. It will be indicated that such kind of non-Brownian motion can explain some recent observations in cell motility experiments.

Interacting self-propelled particles display fascinating phenomena. Their study has applicability in a wide range of systems of different complexity: from autonomous robots [21–23], traffic [24] and human crowds [25], to biological systems of all possible scales as birds [26], bacteria [27, 28], or even down to a molecular level as in the dynamics of actin and tubulin filaments [29–32]. One of the most interesting aspects of interacting active particles is that they can exhibit behaviors forbidden to equilibrium systems. Probably, one of the most remarkable examples is the possibility of long-range orientational order in two-dimensional systems with continuum symmetry. The Mermin-Wagner theorem states that equilibrium systems with these characteristics cannot exhibit long-range order [33]. However, self-propelled particles with continuum symmetry and moving in a two-dimensional space, as shown for the first time by Vicsek *et al.* in [34], can develop long-range orientational order.

The model proposed in [34] consists of point-like particles that move with a velocity vector of constant magnitude and interact by aligning their velocity direction to the local average velocity. It has been proposed that this model might describe the collective motion of birds, fish or even swimming bacteria [35–39]. Though this celebrated model offers a reasonable phenomenological description for many macroscopic patterns observed in some organisms, it does not account for the actual ”microscopic” mechanism that leads the individuals to exhibit such a local alignment. The same applies to other qualitative approaches that focus on the macroscopic description of the observed patterns [40–45]. A key question not addressed by these models refers the simplest physical mechanisms that leads to collective motion in self-propelled particles. Collective motion is defined in this context as a non-zero macroscopic orientational order parameter and is associated to the formation of groups inside which particles move in the same direction. We know that long-range chemical signals can be used by self-propelled entities to sense the environment and coordinate their motion as in bacteria like *E. coli* or amoebae like *D. discoideum* [46]. But, is there a short-range physical mechanism that can produce a similar

behavior? Myxobacteria, for instance, a gram-negative gliding bacteria, coordinate their motion by a membrane-bound signal system, called C-signal, which requires physical cell-to-cell contact to transfer information. Interestingly, during the early stages of their life-cycle these bacteria exhibit a complex collective behavior even without exchanging that signal [27, 28, 47]. This fact suggests that these cells organize their motion by simply pushing each other. Are then self-propelled particles interacting by volume exclusion able to form swarms? In Chapter 3 it will be shown that such simple physical interactions of self-propelled rod-shaped objects lead to collective motion and clustering. Moreover, it will be explained how the particle shape influences the emerging patterns. Remarkably, there is a critical particle aspect ratio that triggers clustering. It will be also indicated that those effects might play a major role in the collective motion of some gliding bacteria as myxobacteria.

While volume exclusion may represent the most basic and simplest physical mechanism leading to collective motion in systems of self-propelled particles, the resulting alignment mechanism is intrinsically different from that proposed by Vicsek *et al.*. The interaction of elongated self-propelled objects, as it will be shown in Chapter 3, can cause particles to locally align parallel as well as antiparallel to each other, i.e., the alignment mechanism is apolar. On the contrary, in Vicsek model as well as in other self-propelled particle models [35, 37, 39–44], the involved alignment mechanism is polar, i.e., it induces particles to locally point in the same direction. It is worth to notice that apolar alignment mechanisms have previously only been used with apolar particles. Apolar particles are particles whose ”head” and ”tail” are indistinguishable. In contrast, the self-propelled particles are by definition polar, since in this case we can define a particle ”head” and ”tail”. Interestingly, all known systems in two-dimensions, either equilibrium or non-equilibrium systems, with apolar particles and apolar interaction lack long-range order [33, 48–50]. On the other hand, polar particles with polar interaction, as mentioned above, can exhibit long-range order. But, what happens in a system of polar particles with apolar interactions such as myxobacteria? In Chapter 4 this question will be addressed. It will be shown that such a system can exhibit long-range order, with a phase transition whose character changes from high to low particle density. Surprisingly, at high density the system can reach an ordered state that is neither pure nematic nor polar, but an interesting mixture of both.

Since self-propelled particles can interact by either a polar or apolar alignment mechanisms, the further understanding of self-propelled particle dynamics requires a

common theoretical framework to describe both possible alignment mechanisms. In Chapter 5 it will be shown that some basic differences of the ordered states under both alignment mechanisms can be captured by a simple mean-field description. Moreover, it will be explained why in self-propelled particles with polar interactions, the transition to orientational order occurs at larger values of the noise intensity than for the analogous system with apolar interactions.

The physics of interacting and non-interacting self-propelled particles in two-dimensions is a complex and fascinating topic whose study might help to understand fundamental open questions in non-equilibrium statistical physics, ecology and developmental biology. We hope through this Thesis to shed some light on some of the questions and aspects of this novel field.

Outline of the thesis:

Chapter 2

General aspects of two-dimensional self-propelled particle motion, with fluctuations in the speed and direction of motion are studied. It is considered the case in which fluctuations in the speed are not correlated to fluctuations in the direction of motion. Expressions for the mean square displacement and diffusion coefficient are derived.

Chapter 3

A simple model for self-propelled rods interacting by volume exclusion is presented and analyzed. It is shown that this simple physical system can exhibit collective motion. It is also shown that these self-propelled rod-shaped particles, interacting only through short-range repulsive interactions, exhibit a non-equilibrium transition to clustering for sufficient large values of the density and particle aspect ratio. Clustering effects affect speed distribution, particle rotation, and local and global ordering of the particles. The transition to clustering is reproduced by a mean-field description of the cluster size distribution. Far below the transition, the clustering dynamics is explained in term of a maximum entropy principle.

Chapter 4

A model for self-propelled particles interacting through an apolar alignment mechanism is introduced and analyzed. It is shown that these particles exhibit for low enough orientational noise a kinetic phase transition to orientational order. Interestingly, the character of the transition is shown to be strongly dependent on particle density, being continuous at high density and discontinuous at low density. Clustering is proven to be essential to achieved long-range orientational order at low density.

Chapter 5

A common theoretical framework to describe the macroscopic dynamics of self-propelled particles under polar and apolar alignment mechanism is derived. It is shown that at high density the orientation dynamics is captured by a simple mean-field approach which predicts a smaller critical noise amplitude for apolar than for polar interactions.

Chapter 6

A summary of the results obtained throughout the thesis is presented.

Chapter 2

Individual motion: fluctuations in the speed and in the direction of motion

Introduction

The study of cell movement on surfaces can shed light on the processes that underlie cell motility [51]. *In vitro* experiments that characterize cell movement include wound closure assays and individual cell tracking to determine cell trajectories [5–8]. To interpret and understand such experiments it is necessary to rely on a phenomenological description of the motion, providing expressions that allow to fit the experimental observations and compute motility indexes [7, 20].

Persistent motion subject to fluctuations has been described by a class of stochastic processes known as persistent random walk [12, 15, 52–54]. In such processes the direction of motion fluctuates, but on short time scales a persistence to move without turning is observed, Fig. 2.1 (a). Formally, the velocity autocorrelation function $\langle \mathbf{v}(t) \cdot \mathbf{v}(0) \rangle$ exhibits a finite decay time, giving rise to a ballistic regime $\langle \mathbf{x}^2(t) \rangle \sim t^2$ for short times and a crossover to a diffusive regime $\langle \mathbf{x}^2(t) \rangle \sim t$ for long times [15, 53, 54].

A related problem is that of the directed motion of self-propelled particles driven by an external field. Single cells can be directed by external signals in the form of concentration gradients, as in the case of fibroblasts [55] or the amoebae *D. discoideum* [56] (see Fig. 2.1 (b)). Directed motion with fluctuations can be described by another broad class

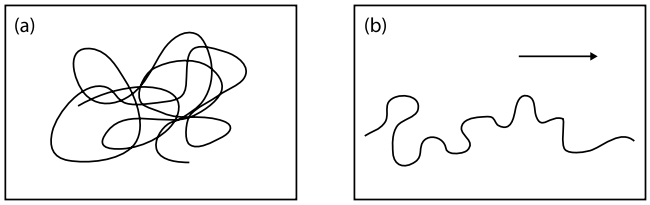

Figure 2.1: Schematic representation of (a) persistent and (b) directed random walks.

of stochastic processes known as the directed random walks [12, 53], which displays a diffusive regime for short times followed by a ballistic regime for long times [55, 57].

Fluctuations in the speed and direction of motion were considered to occur simultaneously, or fluctuations of the speed were simply neglected [12, 15, 17, 52–54, 58, 59]. However, recent cell motility experiments suggest that some cells migrate exhibiting fluctuations in the speed and the direction of motion which apparently are uncorrelated [7]. Motivated by these experiments, this chapter is devoted to the study of two-dimensional self-propelled particles with uncorrelated fluctuations of the speed and the direction of motion. It is assumed that both processes can be described by independent characteristic time-scales. Two different angular dynamics are investigated which correspond to persistent and directed random walks. For these two problems exact expressions for the mean squared displacement, the asymptotic diffusion coefficient, and the velocity autocorrelation are derived. The expressions are valid for arbitrary speed and angular stationary distributions. It is shown that both persistent and directed random motion exhibit a complex transient with a number of alternating regimes of motion. The effects of speed fluctuations introduce an additive correction to the diffusion coefficient, while the velocity autocorrelation becomes a sum of exponential forms. For the particular case of non-fluctuating speed, the classical persistent and directed Brownian motion are retrieved.

2.1 General framework

In this section we first derive a general framework to calculate the average position $\langle \mathbf{x} \rangle$ and mean squared displacement $\langle \mathbf{x}^2 \rangle$ for a system of stochastic self-propelled particles that move in two dimensions. At the end of the section we specialize the general expressions to the case in which fluctuation in the speed and in the direction of motion are independent.

We start by considering that, for a given particle, its velocity $\mathbf{v}(t)$ at time t is represented by an angle $\theta(t)$, and a modulus —the speed— $v(t)$. The dynamics of the velocity

$\mathbf{v}(t)$ is given by a stochastic process which for the moment is not specified. $d(\theta, t)$ is defined as the total distance covered by the particle moving along the direction θ, since the beginning of the trajectory at $t = 0$. Knowing this quantity we can easily express the position of the particle at time t by:

$$\mathbf{x}(t) = \int_{-\pi}^{\pi} d(\theta, t)\check{r}(\theta)d\theta\,, \tag{2.1.1}$$

and its squared displacement by:

$$\mathbf{x}^2(t) = \iint_{-\pi}^{\pi} d\theta' d\theta'' d(\theta', t)d(\theta'', t)\check{r}(\theta') \cdot \check{r}(\theta'')\,, \tag{2.1.2}$$

where $\check{r}(\theta) = \cos(\theta)\check{x} + \sin(\theta)\check{y}$ is the unit vector along the direction θ. We are interested in $\langle \mathbf{x}(t) \rangle$ and $\langle \mathbf{x}^2(t) \rangle$. This implies that $\langle d(\theta, t) \rangle$ and $\langle d(\theta', t)d(\theta'', t) \rangle$ have to be calculated. Notice that given a particular trajectory characterized by $\tilde{\theta}(t)$ and $\tilde{v}(t)$, the distance $d(\theta, t)$ can be expressed as

$$d(\theta, t) = \int_0^t dt' \int_0^{\infty} dv\, v\, \delta(v - \tilde{v}(t'))\delta(\theta - \tilde{\theta}(t'))\,. \tag{2.1.3}$$

Thus, the ensemble average of this distance is

$$\langle d(\theta, t) \rangle = \int_0^t dt' \int_0^{\infty} dv\, v\, p(\theta, v, t')\,, \tag{2.1.4}$$

where we have introduced the probability density to find the particle moving in the direction θ with speed v at time t, which by definition is $p(\theta, v, t) = \langle \delta(v - \tilde{v}(t))\delta(\theta - \tilde{\theta}(t)) \rangle$ [60]. $\langle \ldots \rangle$ denotes ensemble averages. On the other hand, $d(\theta', t)d(\theta'', t)$ takes the form:

$$\begin{aligned} d(\theta', t)d(\theta'', t) = & \int_0^t dt' \int_0^t dt'' \\ & \int_0^{\infty} dv' \int_0^{\infty} dv'' v' v'' \quad \delta(v - \tilde{v}(t'))\delta(v - \tilde{v}(t''))\delta(\theta - \tilde{\theta}(t'))\delta(\theta - \tilde{\theta}(t''))\,. \end{aligned} \tag{2.1.5}$$

The ensemble average of these delta distributions is by definition: $p(\theta', v', t'; \theta'', v'', t'') = \langle \delta(v - \tilde{v}(t'))\delta(v - \tilde{v}(t''))\delta(\theta - \tilde{\theta}(t'))\delta(\theta - \tilde{\theta}(t'')) \rangle$. Then, the correlations $\langle d(\theta', t)d(\theta'', t) \rangle$

between these distances can be written in terms of the joint probability distribution as follows:

$$\langle d(\theta',t)d(\theta'',t)\rangle = \int_0^t dt' \int_0^t dt'' \int_0^\infty dv' \int_0^\infty dv'' v' v'' \quad p(\theta',v',t';\theta'',v'',t'')\,. \tag{2.1.6}$$

Using Eq. (2.1.4) the mean value of the position is expressed as:

$$\langle \mathbf{x}(t)\rangle = \int_{-\pi}^{\pi} \langle d(\theta,t)\rangle \check{r}(\theta) d\theta\,, \tag{2.1.7}$$

while through Eq. (2.1.6) the mean square displacement takes the form:

$$\langle \mathbf{x}^2(t)\rangle = \iint_{-\pi}^{\pi} d\theta' d\theta'' \langle d(\theta',t)d(\theta'',t)\rangle \check{r}(\theta') \cdot \check{r}(\theta''). \tag{2.1.8}$$

Eqs. (2.1.4) to (2.1.8) provide a general way to calculate the mean value of the position and the mean square displacement, which so far does not involve any assumptions. In the following, we consider the special case in which the fluctuations in the speed v are not correlated with the fluctuations in the direction θ. As a consequence, $p(\theta,v,t) = p(\theta,t)p(v,t)$ and $p(\theta',v',t';\theta'',v'',t'') = p(\theta',t';\theta'',t'')p(v',t';v'',t'')$. This can be the case if, for example, fluctuations in the speed are due to a noise associated to the propelling engine of the particles, while fluctuations in the direction of motion reflect the interaction with a noise environment. Beyond these theoretical considerations, there are biological examples in which the time scales associated to the speed and direction of motion fluctuations differ considerably. This strongly suggests that in such kind of experiments the assumption of the independence of both fluctuations is reasonable [7]. At this point we restrict the problem to a situation in which the velocity fluctuations are in the stationary state, with an arbitrary speed distribution $p(v,t) = \rho(v)$ and the joint probability given by

$$\begin{aligned} p(v',t';v'',t'') &= \rho(v')\delta(v'-v'')e^{-\beta|t'-t''|} \\ &+ \rho(v')\rho(v'')\left(1-e^{-\beta|t'-t''|}\right)\,. \end{aligned} \tag{2.1.9}$$

This expression for the joint probability distribution $p(v',t';v'',t'')$ implies that the speed correlations decay exponentially, as

$$\langle v(t)v(0)\rangle - \langle v\rangle^2 = (\langle v^2\rangle - \langle v\rangle^2)e^{-\beta t}. \tag{2.1.10}$$

Here $\langle v \rangle$ and $\langle v^2 \rangle$ are the first and second moments of the stationary speed probability distribution $\rho(v)$. In other words, through Eq. (2.1.9) it is assumed that the speed cannot instantaneously change, i.e., there is a characteristic time β^{-1} during which particles "remember" their speed. After that characteristic time particles "forget" about their initial speed (at time t''), and so, the speed of a particle at times t' and t'' far apart are independent. This is reflected by the speed correlations in Eq. (2.1.10). One example of a stochastic process leading to such kind of correlation is given by $v(t) = \widetilde{\eta}(t)$, where the value of the noise $\widetilde{\eta}(t)$ is taken from a distribution ρ at times given by a Poisson process of rate β, and kept constant in between. This can be expressed as $\partial_t p(v,t) = -\beta p(v,t) + \beta \rho(v)$.

Under these assumptions Eqs. (2.1.4) and (2.1.6) can now be simplified performing the integrals on the speed

$$\langle d(\theta,t) \rangle = \langle v \rangle \int_0^t dt' p(\theta,t') \tag{2.1.11}$$

$$\begin{aligned} \langle d(\theta',t) d(\theta'',t) \rangle &= \langle v \rangle^2 \iint_0^t dt' dt'' p(\theta',t';\theta'',t'') \\ &+ (\langle v^2 \rangle - \langle v \rangle^2) \iint_0^t dt' dt'' p(\theta',t';\theta'',t'') e^{-\beta |t'-t''|} \end{aligned} \tag{2.1.12}$$

Notably Eq. (2.1.11) does not differ from the corresponding expression for constant speed, so the mean total distance is not affected by speed fluctuations. Introducing the time spent by a particle moving along direction θ as $\langle T(\theta,t) \rangle = \int_0^t dt' p(\theta,t')$, $\langle d(\theta,t) \rangle$ is expressed as $\langle d(\theta,t) \rangle = \langle v \rangle \langle T(\theta,t) \rangle$. On the other hand, speed fluctuations do affect the distance correlations, Eq. (2.1.12), as an additive correction proportional to the speed variance $\sigma^2 = \langle v^2 \rangle - \langle v \rangle^2$.

We are now left with the one-dimensional problem of angular fluctuations on the ring, i.e., the direction of motion. In the next two chapters we will consider two situations which differ only in the dynamics of the direction of motion.

2.2 Persistent random walk

As a first application, we consider the case of a persistent random walk, see Fig. 2.1 (a). We study a problem in which the angular probability distribution function obeys the

diffusion equation characterized by the diffusion constant κ. A simple example of a stochastic process leading to such equation is a dynamics for direction of motion given by $\dot{\theta}(t) = \eta(t)$, where $\eta(t)$ is a white noise. Another example is an angular dynamics described by discrete turning events. If the rate of angular jumps are characterized by α, and the length of the jumps ϕ obey a symmetric distribution $\rho(\phi)$, then the diffusion coefficient can be expressed as $\kappa = \langle\Gamma\rangle\alpha$, where $\Gamma = \int \phi^2\rho(\phi)d\phi$.

Since initially the ensemble of particles is concentrated at $\mathbf{x}(t=0) = \mathbf{0}$ and starts to move in all possible direction, then $p(\theta, t) = 1/2\pi$. Notice that the dynamics of the direction of motion of each individual particle starts with a particular direction, and smoothly explores other directions, which implies that we have to wait some characteristic time before finding the particle pointing with equal probability in any direction. This fact is reflected by $p(\theta', t'|\theta'', t'')$ which obeys the diffusion equation:

$$\partial_{t'} p(\theta', t'|\theta'', t'') = \kappa\partial_{\theta'\theta'} p(\theta', t'|\theta'', t'')$$

with the initial condition $p(\theta', t'|\theta'', t'') = \delta(t' - t'')\delta(\theta' - \theta'')$. To guarantee the conservation of the probability inside the ring the following periodic boundary conditions are imposed: $p(\pi, t'|\theta'', t'') = p(-\pi, t'|\theta'', t'')$ and $\partial_{\theta'} p(\pi, t'|\theta'', t'') = \partial_{\theta'} p(-\pi, t'|\theta'', t'')$. Taking all this into account we obtain the solution for the conditional probability:

$$p(\theta', t'|\theta'', t'') = \frac{1}{2\pi} + \frac{1}{\pi}\sum_{m=1}^{\infty} \cos(m(\theta' - \theta''))\, e^{-(m^2\kappa|t'-t''|)} \tag{2.2.1}$$

From this expression we learn that the particles loose the information about the direction of motion in a characteristic time. In particular, as $|t' - t''| \to \infty$ the information about the direction of motion at time t'' is completely absent, and each particle points with equal probability in any direction. The slowest mode $m = 1$ sets a characteristic time-scale κ^{-1} that separates two distinct regimes. For $t \ll \kappa^{-1}$ the conditional probability has a maximum, because the particles still "remember" their direction of motion at time t''. For $t \gg \kappa^{-1}$ the slowest mode decays and there is no information about the orientation at time t'' .

Recalling that $p(\theta, t'; \theta', t'') = p(\theta, t'|\theta', t'')p(\theta', t'')$, and then using Eq. (2.2.1) to calculate Eqs. (2.1.11) and (2.1.12), and finally inserting these expressions into Eqs. (2.1.7) and (2.1.8) it is obtained that $\langle\mathbf{x}(t)\rangle = \mathbf{0}$ and

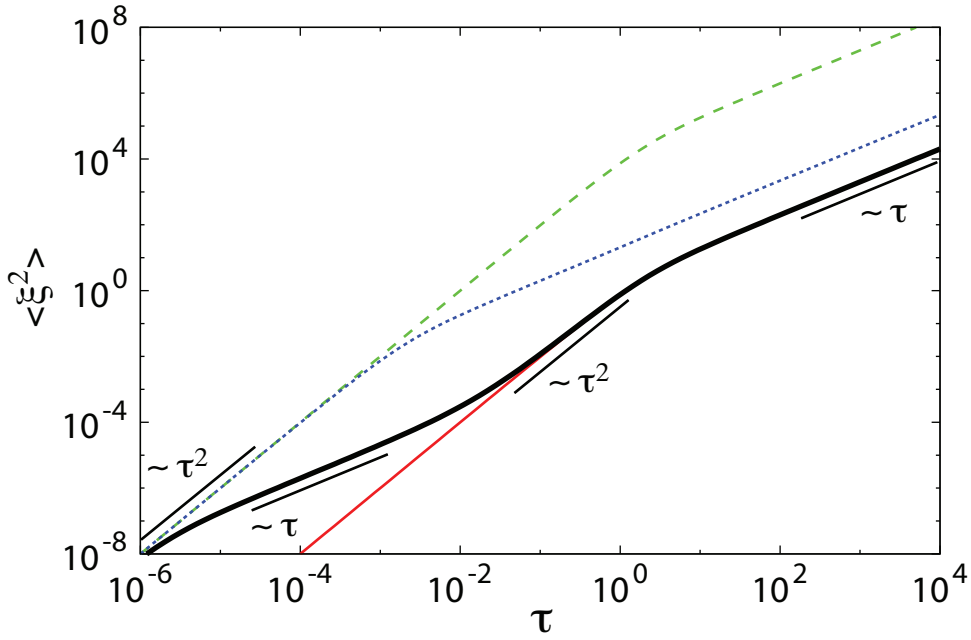

Figure 2.2: Scaled mean squared position as a function of scaled time for persistent random walks. The lines correspond to Eq. (2.2.2) for rescaled variables. The thin solid red line corresponds to $\mu = 0$, and $\mu = 100$ for the other curves, with $\gamma = 10^{-3}$ (dashed green line), $\gamma = 10^{3}$ (dotted blue line) and $\gamma = 10^{6}$ (thick solid black line).

$$\begin{aligned} \langle \mathbf{x}^2(t) \rangle &= 2\frac{\langle v \rangle^2}{\kappa^2}\left(\kappa t - 1 + e^{-\kappa t}\right) \\ &+ 2\frac{\langle v^2 \rangle - \langle v \rangle^2}{(\kappa+\beta)^2}\left((\kappa+\beta)t - 1 + e^{-(\kappa+\beta)t}\right) \end{aligned} \tag{2.2.2}$$

In the absence of speed fluctuations, the speed variance $\sigma^2 = \langle v^2 \rangle - \langle v \rangle^2$ vanishes and Eq. (2.2.2) reduces to the well known result of "Brownian" particles moving at constant speed [53, 54], which exhibits a single crossover at $t \sim \kappa^{-1}$, see red curve in Fig. 2.2. When fluctuations become relevant, depending on the relative values of κ and β and the value of the speed variance σ^2, a number of crossovers can unfold separating up to four alternating regimes of motion, see black curve in Fig. 2.2.

In order to unveil the different regimes that Eq. (2.2.2) permits, we introduce non-dimensional variables $\xi = x\kappa/\langle v \rangle$ and $\tau = \kappa t$, and parameters $\mu^2 = \sigma^2/\langle v \rangle^2$ and $\gamma = \beta/\kappa$. For $\gamma \ll 1$ there is a single crossover at $\tau \sim 1$, see green curve in Fig. 2.2. For

any other values of γ, solutions lie between the green and red curves. For $\tau \ll (1+\gamma)^{-1}$ it is observed that $\langle \xi^2 \rangle \simeq (1+\mu^2)\tau^2$. This ballistic regime at short time-scales is a consequence of the exponential decay in the correlations of the speed. A first crossover occurs at $\tau_1 \sim (1+\gamma)^{-1}$. For larger times, it may happen that the separation of time-scales is such that $(1+\gamma)^{-1} \ll \tau \ll 1$. In this case $\langle \xi^2 \rangle \simeq \tau^2 + 2\mu^2\tau/(1+\gamma)$. If μ^2 is sufficiently large, a second crossover might be observable at $\tau_2 \sim 2\mu^2/(1+\gamma)$ separating a transient diffusive regime from a second ballistic regime. Finally, for $\tau \gg 1$ the asymptotic diffusive regime emerges with $\langle \xi^2 \rangle \simeq 2(1+\mu^2/(1+\gamma))\tau$, after the third crossover at $\tau_3 \sim 1$. Such asymptotic regime can be described in terms of an effective diffusion coefficient, defined as

$$\mathcal{D} = \lim_{t\to\infty} (\langle \mathbf{x}^2(t) \rangle - \langle \mathbf{x}(t) \rangle^2)/2t \,. \tag{2.2.3}$$

From Eq. (2.2.2), we obtain:

$$\mathcal{D} = \langle v \rangle^2 \kappa^{-1} + \left(\langle v^2 \rangle - \langle v \rangle^2 \right) (\kappa + \beta)^{-1} \,. \tag{2.2.4}$$

Speed fluctuations introduce an additive correction to the well known diffusion coefficient for constant speed [54].

We stress that it can be observed up to four consecutive regimes of motion separated by three crossovers, while in the absence of speed fluctuations only one crossover is found [53, 54]. To obtain an heuristic understanding of this result, notice that the second term in Eq. (2.2.2) is proportional to the speed variance σ^2 and exhibits the first crossover from a ballistic to a diffusive regime at $t \sim (\kappa+\beta)^{-1}$. The first term is proportional to the squared mean value of the speed and exhibits a crossover from a ballistic to a diffusive regime at a later time $t \sim \kappa^{-1}$. If the separation of time-scales allows it another crossover could be observed between these two, when the diffusive regime of the second term turns into the ballistic regime of the first as in the black curve in Fig. 2.2. Note that for this to happen the speed variance must be sufficiently large.

The effects of the speed fluctuations are also exposed in the velocity autocorrelation function which takes the form:

$$\langle \mathbf{v}(t) \cdot \mathbf{v}(0) \rangle = \langle v \rangle^2 \, e^{-\kappa t} + \left(\langle v^2 \rangle - \langle v \rangle^2 \right) e^{-(\beta+\kappa)t} \,. \tag{2.2.5}$$

The velocity autocorrelation function of the classical Brownian motion has a single exponential form, while now, due to the speed fluctuations, it becomes a sum of two exponentials.

Notice that in Fig. 2.2 it is used a large speed variance and $\langle \mathbf{x}^2(t) \rangle$ is plotted over a huge range to illustrate all the features of Eq. (2.2.2). In the concluding remarks section it is discussed the effects of the experimental constraints in the observation of the phenomena described here.

2.3 Directed persistent random walk

As a second example we consider the directed random walk, in which the particles have some preferred direction of motion. This could be the case for particles moving in a symmetry-breaking field or subject to an external force. An example of such kind of stochastic process is $\theta(t) = \eta(t)$, where the value of the noise $\eta(t)$ is taken from a distribution ρ at times given by a Poisson process of rate α, and kept constant in between. This can be expressed as $\partial_t p(\theta, t) = -\alpha p(\theta, t) + \alpha \rho(\theta)$. This implies that angular fluctuations are also in the stationary state, $p(\theta, t) = \rho(\theta)$. We describe the presence of an external field by assuming that $\int_{-\pi/2}^{\pi/2} \rho(\theta) d\theta > 1/2$, together with the symmetry requirement $\rho(-\theta) = \rho(\theta)$, setting a preferred direction of motion along $\theta = 0$. The Poissonian nature of the angular fluctuations imply that the time correlations decay exponentially with a characteristic time α^{-1}

$$\begin{aligned} p(\theta', t'; \theta'', t'') &= \rho(\theta')\delta(\theta' - \theta'')e^{-\alpha|t'-t''|} \\ &+ \rho(\theta')\rho(\theta'')\left(1 - e^{-\alpha|t'-t''|}\right) . \end{aligned} \tag{2.3.1}$$

Using this expressions for the angular probability distributions together with Eqs. (2.1.11) and (2.1.12) in the expressions (2.1.7) and (2.1.8) we arrive at the following expressions for the mean value of the position

$$\langle \mathbf{x}(t) \rangle = \sqrt{c} \langle v \rangle t \, \check{x} \tag{2.3.2}$$

and the mean square displacement

$$\begin{aligned} \langle \mathbf{x}^2(t) \rangle &= \langle v \rangle^2 \left[ct^2 + 2(1-c)\varphi_\alpha(t) \right] \\ &+ 2\left(\langle v^2 \rangle - \langle v \rangle^2 \right) \left[(1-c)\varphi_{\alpha+\beta}(t) + c\varphi_\beta(t) \right] \end{aligned} \tag{2.3.3}$$

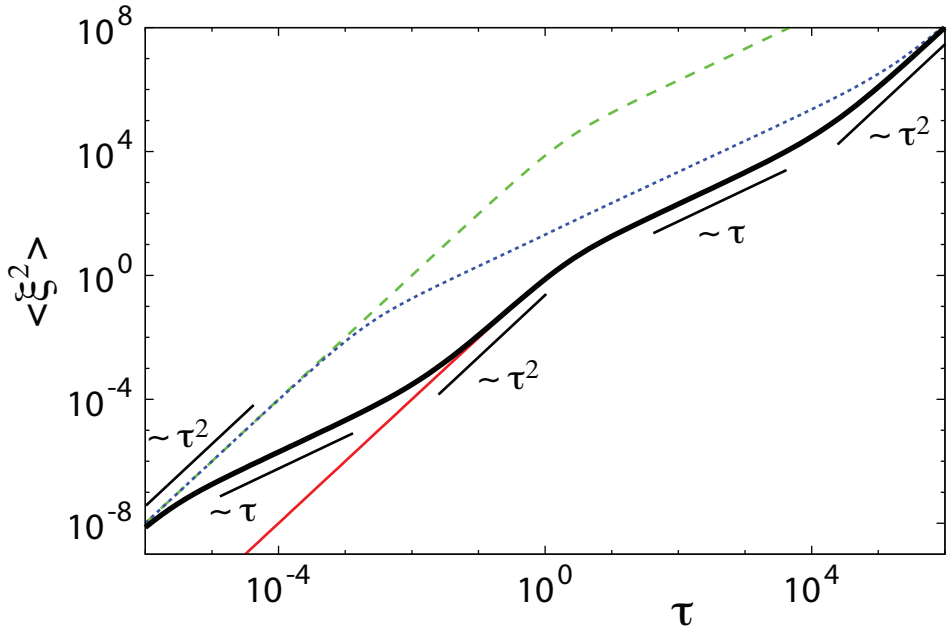

Figure 2.3: Scaled mean squared position as a function of scaled time for directed random walks. The lines correspond to Eq. (2.3.3) for the rescaled variables, with $c = 10^{-4}$. The thin solid red line corresponds to $\mu = 0$. The other curves correspond to $\mu = 100$, with $\gamma = 10^{-3}$ (dashed green line), $\gamma = 10^3$ (dotted blue line) and $\gamma = 10^6$ (thick solid black line).

where $c = \langle \cos\theta \rangle^2$ and $\varphi_\alpha(t) = \alpha^{-2}\left[\alpha t - (1 - e^{-\alpha t})\right]$.

The mean value of the position grows linearly with time, as occurs when the speed is constant [53]. The angular distribution affects the constant $c = \langle \cos\theta \rangle^2$. This constant can vanish in the extreme situation where the angular distribution $\rho(\theta)$ is uniform in the interval $[-\pi, \pi]$. Such situation corresponds to a persistent random walk in its asymptotic regime, after the non-constant modes of the angular distribution have settled down. The mean square displacement on the other hand can portray a range of complex behaviors for transient times.

We introduce the non-dimensional variable $\xi = x\alpha/\langle v \rangle$ and a non-dimensional parameter $\delta = \beta/\alpha$. In the absence of speed fluctuations, the second line in Eq. (2.3.3) vanishes. In such case, a ballistic regime is observed at short times $\tau \ll 1$. For $1 \ll \tau$ the non-dimensional mean square displacement follows $\langle \xi^2 \rangle \simeq c\tau^2 + 2(1-c)\tau$. Thus, a second crossover might be observable if $c < 2/3$, separating a transient diffusive regime from the asymptotic ballistic regime dominant for very large times.

When speed fluctuations are present, the additional time-scale β which describes

speed correlations can give rise up to four crossovers, if the adequate conditions hold, depending on the value of μ and $\delta = \beta/\alpha$.

As an illustration, it considered here $\delta \ll 1$, corresponding to a case where speed fluctuations occur much slower than angular fluctuations. For short times $\tau \ll 1 \ll \delta^{-1}$ there is a ballistic regime $\langle \xi^2 \rangle \simeq (1+\mu^2)\tau^2$. $\tau_1 \sim 1$ marks the crossover to a second regime, visible for $1 \ll \tau \ll \delta^{-1}$, and characterized by $\langle \xi^2 \rangle \simeq c(1+\mu^2)\tau^2 + 2(1-c)(1+\mu^2)\tau$. Here, a second crossover could appear at $\tau_2 \sim 2(c^{-1}-1)$ between the diffusive regime and a second ballistic regime. Note that c should be such that $1 \ll \tau_2$. Finally, for $1 \ll \delta^{-1} \ll \tau$, the non-dimensional mean square displacement follows $\langle \xi^2 \rangle \simeq c\tau^2 + 2[(1-c)(1+\mu^2) + \mu^2 c\delta^{-1}]\tau$. This describes a second transient diffusive regime, and the asymptotic ballistic regime observed for very large times, with a crossover at $\tau_4 \sim 2c^{-1}[(1-c)(1+\mu^2) + \mu^2 c\delta^{-1}]$.

As observed for the persistent random walk, speed fluctuations in the directed random walk also introduce a new time scale, which together with the angular fluctuation time scale can lead up to five different regimes of motion, and four crossovers separating the ballistic and diffusive regimes. In the absent of speed fluctuations the behavior of the mean square displacement reduces to two regimes with a single crossover [57].

Also in this example the effective diffusion coefficient $\mathcal{D}$ can be derived. Applying the definition given by Eq. (2.2.3), the following expression is obtained:

$$\mathcal{D} = (1-c)\langle v \rangle^2 \alpha^{-1} + (\langle v^2 \rangle - \langle v \rangle^2)[(1-c)(\alpha+\beta)^{-1} + c\beta^{-1}]\,. \tag{2.3.4}$$

The presence of an external field decouples the time-scale of speed fluctuations and the velocity autocorrelation results in a sum of three exponentials:

$$\begin{aligned} \langle \mathbf{v}(t)\cdot\mathbf{v}(0)\rangle &= \langle v\rangle^2[c + (1-c)e^{-\alpha t}] \\ &+ c(\langle v^2\rangle - \langle v\rangle^2)e^{-\beta t} + (1-c)(\langle v^2\rangle - \langle v\rangle^2)e^{-(\alpha+\beta)t}\,. \end{aligned} \tag{2.3.5}$$

2.4 Concluding remarks

We have studied self-propelled particle motion in two dimensions in the presence of fluctuations. Assuming that both the direction of motion and the speed fluctuate with independent characteristic times, we have considered persistent and directed random walks.

In both cases, the interplay of speed and angular fluctuations gives rise to a sequence of ballistic and diffusive regimes, revealing a complex transient not observed when speed fluctuations are absent. We have obtained analytical expressions for the mean value of the position and for the mean squared displacement, and calculated the crossover times and the effective diffusion coefficient describing the asymptotic regimes.

The occurrence of such a complex transient in the mean squared displacement can wreck the interpretation of experimental observations, due to the constrains imposed by resolution and finite size limitations. Particle size sets the smallest accessible length-scale, while the field of the experimental setup sets the largest. Similarly, the frequency of observations sets the smallest observable time-scale, and the duration of the measurement sets the largest time-scale. If the window of observation is limited to a part of the complex transient, anomalous diffusion could be wrongly interpreted. Superdiffusion has been repeatedly reported from experimental data [9, 19]. However, distinguishing true superdiffusion from a persistent or directed random walk is a subtle task [61].

The results derived in this section suggest that in some cases the observed anomalous behavior could be related to one or more of the reported crossovers. That is why it becomes essential to consider speed fluctuations when interpreting experimental data. Neglecting speed fluctuations could result in a misleading estimation of the time-scales of the problem and a wrong understanding of the system.

In Fig. 2.4 (a) displays $D(\tau) = (\langle \xi^2(\tau) \rangle - \langle \xi(\tau) \rangle^2)/2\tau$ for a persistent random walk, using time and space ranges which are reasonable for current experimental setups [5, 7]. Furthermore, we choose $\mu = 1.31$ according to data reported in [7], and values of γ within experimental ranges. The solid red line is the result without speed fluctuations. Dots correspond to numerical simulations performed with $\mu = 1.31$ and $\gamma = 10$. In the simulations speeds are chosen at a rate $\beta = 4.0\ \mathrm{h}^{-1}$ from a speed distribution $\rho(v) \sim v^{-3/2}$ for $v \in [1, v_c]$ and zero otherwise, with v_c such that $\mu = 1.31$. Angles are chosen at a rate $9.6\ \mathrm{h}^{-1}$ from a uniform distribution of width 1 rad centered around the direction of motion, and so yielding $\kappa = 0.4\ \mathrm{h}^{-1}$. Error bars are the standard deviation from the mean value obtained for 100 realizations with 100 particles each. This means that a particular 100 particles experiment should fall within the range of such error bars. Fig. 2.4 (a) suggests that for a system that exhibits realistic speed fluctuations as reported in [7], the diffusion coefficient shows a slight, but still observable, deviation from the coefficient of a classical (constant speed) persistent random walk. Fig. 2.4 (b) shows that realistic fluctuations in the speed can produce in the velocity autocorrelation a remarkable devi-

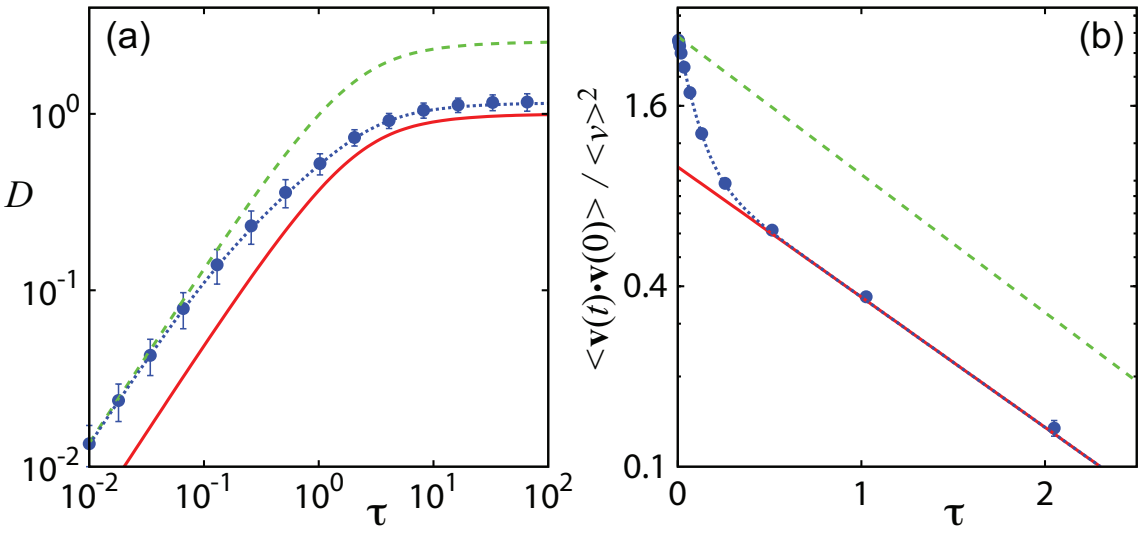

Figure 2.4: (a) Re-scaled mean squared displacement and (b) velocity autocorrelation as a function of scaled time for persistent random walks. The lines in (b) correspond to Eq. (2.2.5) for rescaled variables. In both panels, the solid red line corresponds to $\mu = 0$. For the other curves $\mu = 1.31$, with $\gamma = 10^{-1}$ (dashed green line) and $\gamma = 10$ (dotted blue line). Dots correspond to numerical simulations as described in the text.

ation from the Brownian motion. The velocity autocorrelation function of a Brownian particle is a single exponential. Due to the speed fluctuations the velocity autocorrelation becomes the sum of two exponentials. Such autocorrelations have been observed in cell motility experiments, but the microscopic origin of the fast time-scale has not been established [7]. Fast intracellular processes could give rise to such fluctuations in speed with small characteristic time-scales [62, 63].

To conclude, the simulations suggest that fluctuations in speed as the ones observed in experiments might be enough to cause visible deviations from the classical result [15].

Chapter 3

Collective motion driven by particle shape

Introduction

The study of the collective behavior of self-propelled particles has applications in a wide range of systems. We observe patterns of interacting self-driven entities in autonomous robots [21–23], traffic [24] and human crowds [25]. At the biological level, patterns of self-propelled particles are manifested in all possible scales, from herds, bird flocks, and fish schools [26] to bacterial swarms [27, 28], and even down to a molecular level in the dynamics of actin and tubulin filaments [29–32]. A recurrent question is how these entities coordinate their behavior to form groups which move collectively. At a theoretical level, several qualitative approaches have been made to incorporate the diverse collective behaviors of such different systems in a common framework [34, 40–45]. While these models may satisfactorily explain the phenomenology of some of the observed patterns, due to their generality they usually fail to reveal the actual mechanism used by the entities to coordinate their movement.

Models for bacteria like *E. coli* as well as for amoebae like *D. discoideum* [46], have been based on chemotaxis, a long-range cell interaction mechanism according to which individual cells move in response to chemical signals produced by all other cells. However, in some bacteria there is no evidence for chemotactic cues and cells coordinate their movement by cell-to-cell signaling mechanisms in which physical contact between bacteria is needed [27, 28, 47, 64, 65]. How these bacteria sense their environment, and which

information they transmit constitute intriguing questions. Clearly, aggregation of these bacteria requires an alternative mechanism of gathering to the long-range chemotactic signaling.

The absence of diffusive chemical signals poses interesting questions. Can non-diffusive short-range physical interactions transmit the necessary information to cause aggregation? More specifically, can the self-propulsion and anisotropic shape of bacteria be enough to produce clustering? How important is the shape of bacteria for their collective motion? And finally, why are gliding bacteria rod-shaped objects? In this Chapter it is shown that self-propelled, sufficiently elongated particles in a simple model form clusters and therefore do not require such long-range communication for aggregation. Instead, aggregation depends crucially on the particular shape of the moving objects.

For swimming bacteria it has been proven that the cell shape is essential for individual motion [66–69]. In contrast, the role of cell shape in the collective behavior has remained unexplored. It has been shown experimentally [70] that migrating elongated cells exhibit alignment similar to liquid crystals [71, 72]. A prominent example for collective behavior with no apparent long range interactions are the striking patterns observed during the life-cycle of gliding myxobacteria, see e.g. [27, 28, 47]. Earlier modeling work has reproduced many of these patterns in three dimensions assuming either perfect alignment [73] or a phenomenological alignment force [64, 65]. These models have all considered patterns resulting from exchange of chemical signals, that are absent in an early stage of the myxobacterial life cycle. Nevertheless, a trend from initial independent motion towards formation of larger clusters of aligned bacteria is often observed (see Fig. 3.1). Moreover, aligned motion of self-propelled rods (=polar particles) with apolar interactions is an important example for an "active nematic" phase, that has different properties from the nematic phase observed in two-dimensional driven systems [31, 48]. For instance, while the interaction of self-propelled elongated rods by volume exclusion can result in either parallel or antiparallel local alignment of the particles, as illustrated in Fig. 3.2, these active particles can form coherently moving polar clusters as shown in Fig. 3.3.

In this chapter we introduce a model for self-propelled rods moving in a two-dimensional space in which interactions are based explicitly on particle shape (see Fig. 3.3). Hydrodynamics interactions are neglected. The latter assumption is justified for densely packed objects in very viscous media like bacterial films. The moving rods have exclusively repulsive excluded volume interactions. We find that elongated particles form groups inside which particles are aligned and moving in the same direction (see Fig. 3.3).

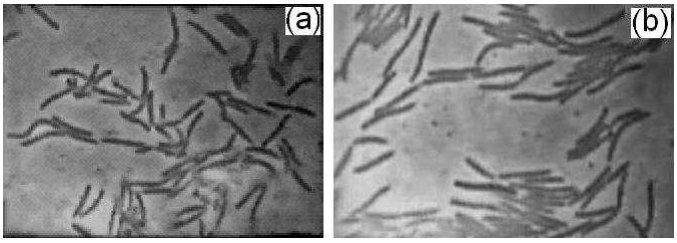

Figure 3.1: Example for clustering of myxobacteria (*M. xanthus*) in the early stage of the life cycle. (a) Immediately after maturation of spores. (b) Afterwards, during the vegetative phase. Snapshots are taken from a movie (Ref. [74], see also [75]), the frame size is 40 x 30 μm^2. Similar phenomena were seen in other bacterial species .

We show multiple evidence for this process. At the level of the speed distribution, we notice that for large values of the particle aspect ratio κ, the distribution becomes sharp and centered around the active speed. This is due to the confinement of particles inside densely packed clusters in which fluctuations are highly restricted. Interestingly, in absence of fluctuations collisions among pure active particles induce a speed distribution which resemble a Maxwell-Boltzmann distribution. We also show that the average square angular velocity, a direct measure of particle rotation, is a non-monotonic function of the κ which exhibits a maximum at an intermediate value of κ. Through the study of the two-body correlation function, we find that particles are locally arranged in a side-by-side and head-to-tail manner. We learn, by analyzing a kind of spin-spin correlation function, that polar local ordering is facilitated by κ. The numerical evidence indicates that elongated particles succeed in forming swarms, while isotropic particles fail in producing local polar ordering. Through the study of the ferromagnetic and liquid crystal order parameter we show that κ also induces global orientation ordering.

In addition, we find that the interplay of rod geometry, self-propulsion, and repulsive short-range interaction is sufficient to facilitate aggregation into clustering. In simulations of an individual based model, clustering of self propelled particles is observed for large enough packing fraction η or aspect ratio κ of the rods (see Figs. 3.3 and 3.5). We define the onset of clustering by the transition from a unimodal to a bimodal cluster size distribution. A mean-field approximation for the cluster size distribution is derived and reproduces the change from a unimodal to a bimodal shape upon increase of either η or κ. The mean-field yields a simple equation $\kappa_c = C/\eta - 1$ for the critical rod aspect ratio, κ_c, at the onset of clustering in line with the individual-based simulation results. We also show that the transition is reflected in the crossover of the probability of the maximum

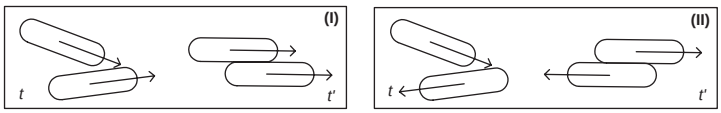

Figure 3.2: The scheme illustrates the possible alignments resulting from a binary collision of self-propelled (polar) particles. Note the alignment can be parallel (I) as well as antiparallel (II).

cluster size, M_T, between a power-law and a logarithmic tail. As a consequence, κ_c is located at the maximum growth rate of M_T with κ. Alternatively, the transition to clustering can be defined as the point at which cluster entropy H_C takes its maximum value. We show that far below the transition, the clustering properties of the system obey the maximum entropy principle applied to H_C, which allow us to describe the system in terms of the total number of clusters. If diffusion is added to the active motion (active-Brownian rods), the clustering transition is shifted to higher values of κ, whereas clustering is absent for pure diffusive motion (Brownian rods) as well as for isotropic particles with $\kappa = 1$. Hence, clustering of particles with excluded volume interaction requires both active motion, i. e. a non-equilibrium system, and elongated particles (= rods).

3.1 The individual based model

We consider rod-shaped particles moving on a plane. Each particle is equipped with a self-propelling force acting along the long axis of the particle. We assume that particles are submerged in a viscous medium. The rod shape of the particles requires three different friction coefficients [72, 76, 77] that correspond to the resistance exerted by the medium when particles either rotate or move along their along and short axis. We consider an overdamped motion of the particles, i.e., inertial terms are neglected. Velocity and angular velocity are proportional to the force and torque, respectively, and the state of a particle is given exclusively by the position of its center of mass, and the orientation of its long axis. Consequently the movement of the ith rod is governed by the following equations for the velocity of its center of mass and angular velocity:

$$(v_{\parallel}^{(i)}, v_{\perp}^{(i)}) = \left(\frac{1}{\zeta_{\parallel}}(F - \frac{\partial U^{(i)}}{\partial x_{\parallel}}), -\frac{1}{\zeta_{\perp}}\frac{\partial U^{(i)}}{\partial x_{\perp}}\right) \tag{3.1.1}$$

$$\dot{\theta}^{(i)} = -\frac{1}{\zeta_{\theta}}\frac{\partial U^{(i)}}{\partial \theta} \tag{3.1.2}$$

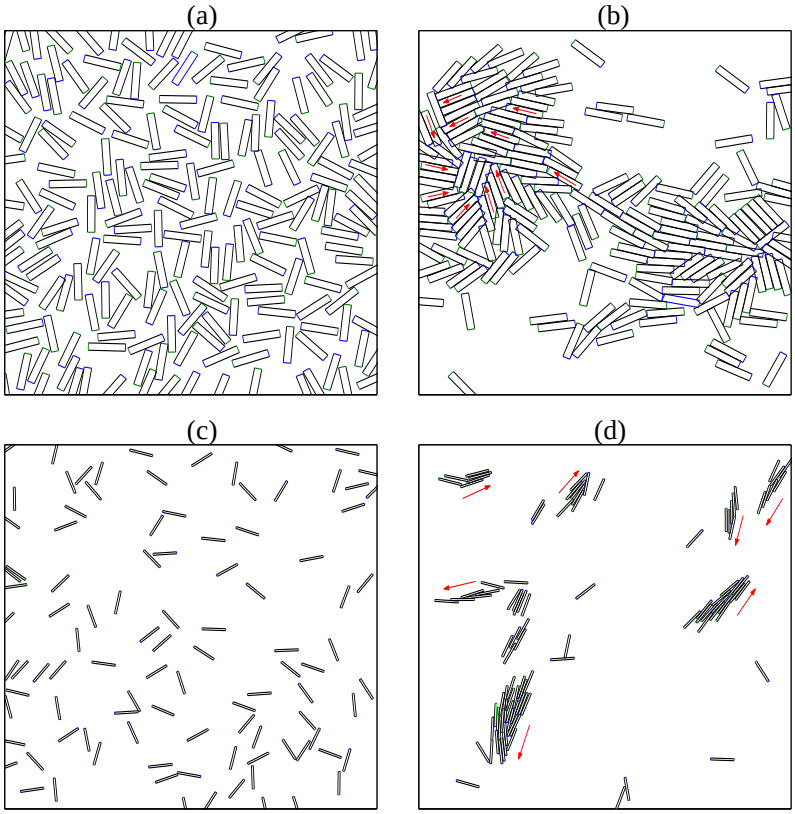

Figure 3.3: Example of the time evolution the individual-based simulations - Snapshots of simulations with periodic boundary condition for various times at high and low density. (a) and (b) correspond to simulations performed with $N = 200$ active particles of aspect ratio $\kappa = 5$ at a packing fraction $\eta = 0.40$ (high density). The initial condition of the simulation is shown in (a), while (b) depicts the system at a later time $t = 1000$. Snapshots shown in (c) and (d) correspond to a simulation performed with $N = 100$ active particles of $\kappa = 12$ at $\eta = 0.034$ (low density). (c) shows the initial state of the system, while (d) refers to $t = 1200$. Arrows indicate directions of motion. Note in (b) the formation of a sporadic vortex-like structure. Typical polar-oriented moving clusters in their characteristic arrow formation are shown in (d).

where $v_{\parallel}^{(i)}, v_{\perp}^{(i)}$ refer to the velocities along the long axis and short axis of the particle, respectively, ζ_i indicates the corresponding friction coefficients (ζ_θ is related to the friction torque), $U^{(i)}$ refers to the energy of the interaction of the ith rod with all other nodes, and F is the magnitude of the self-propelling force. Notice that Eq. (3.1.1) is formulated in a coordinate system that is oriented along the long axis of the particle. This implies that Eqs. (3.1.1) and (3.1.2) are coupled. The motion of the center of mass $\dot{\mathbf{x}}^{(i)} = (v_x^{(i)}, v_y^{(i)})$ of the ith rod is given by

$$\begin{aligned} v_x^{(i)} &= v_{\parallel}^{(i)} \cos\theta^{(i)} + v_{\perp}^{(i)} \sin\theta^{(i)} \\ v_y^{(i)} &= v_{\parallel}^{(i)} \sin\theta^{(i)} - v_{\perp}^{(i)} \cos\theta^{(i)} \end{aligned} \tag{3.1.3}$$

Notice that the velocity direction and the orientation of the particle are not necessarily parallel to each other.

3.1.1 Interaction potential

Particles interact by "soft" volume exclusion, i.e., by a potential that penalize particle overlapping. The potential is defined as follows:

$$U^{(i)}(\mathbf{x}^{(i)}, \theta^{(i)}, \mathbf{x}^{(j)}, \theta^{(j)}) = \phi \sum_{j=1, j\neq i}^{N} \left((\gamma - a_o(\mathbf{x}^{(i)}, \theta^{(i)}, \mathbf{x}^{(j)}, \theta^{(j)}))^{-\beta} - \gamma^{-\beta} \right) \tag{3.1.4}$$

where $a_o(\mathbf{x}^{(i)}, \theta^{(i)}, \mathbf{x}^{(j)}, \theta^{(j)})$ is the overlap area[1] of the rods i and j, γ is a parameter which can be associated to the maximum compressibility, β controls the stiffness of the particle, and ϕ is the interaction strength.

In the limit of β going to infinity we recover the classical hard-core potential. The reasoning is the following. Assume $\gamma = 1$ equal to the volume of the particles, then the potential can be expressed for a small overlapping area ϵ as: $U(\epsilon) = \beta\epsilon$. For the limit of β going to infinity any finite value of ϵ produces a divergence. In consequence, to avoid the divergence ϵ has to be $\epsilon = 0$, and so we obtain a hard-core potential.

It is worth noticing that since the derivative of the overlapping area depends on how particles are colliding, the potential provides different forces and torques upon the spatial arrangement of the particles at the moment of the collision, see Fig. 3.4.

[1]The numerical estimation of the overlap area is the bottleneck of the simulations. In Appendix A a brief explanation about an efficient numerical calculation is provided.

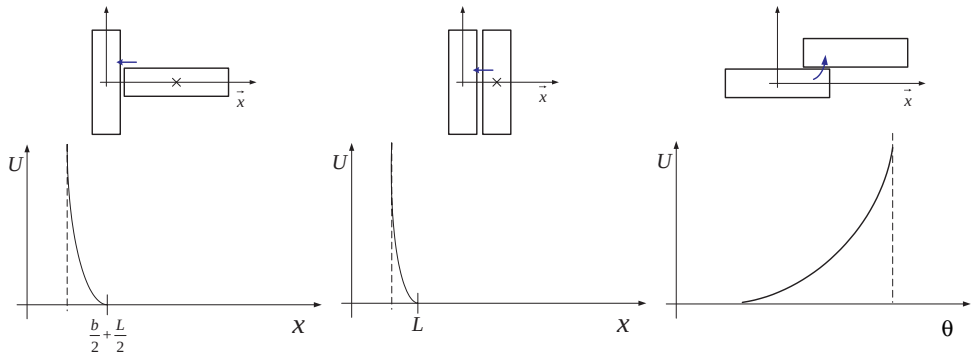

Figure 3.4: The scheme shows that the potential provides different forces and torques depending on how particles are colliding. This is owed to the different derivatives of the overlapping area for each case.

3.1.2 Fluctuations

We study the effects of fluctuations by inserting additive noise terms $R_\perp(t), R_\parallel(t)$ in Eq. (3.1.1) and $R_\theta(t)$ in Eq. (3.1.2). The stochastic motion of the ith particle is then given by:

$$\begin{aligned}(v_\parallel^{(i)}, v_\perp^{(i)}) &= \left(\frac{1}{\zeta_\parallel}(R_\parallel^{(i)} + F - \frac{\partial U^{(i)}}{\partial x_\parallel}), \frac{1}{\zeta_\perp}\left(R_\perp^{(i)} - \frac{\partial U^{(i)}}{\partial x_\perp}\right)\right) \\ \dot{\theta}^{(i)} &= \frac{1}{\zeta_\theta}\left(R_\theta^{(i)} - \frac{\partial U^{(i)}}{\partial \theta}\right)\end{aligned} \tag{3.1.5}$$

where the white noise terms are of the form:

$$\begin{aligned}\langle R_A^{(i)}(t)\rangle &= 0 \\ \langle R_A^{(i)}(t) R_B^{(i)}(t')\rangle &= \epsilon_{A,B}\delta_{i,j}\delta(t-t')\end{aligned} \tag{3.1.6}$$

where A and B stand for $\parallel$, $\perp$, and θ, $\delta(t-t')$ is a Dirac delta function, $\delta_{i,j}$ is Kronecker delta function, and $\epsilon_{A,B}$ is defined as follows. For $A \neq B$, $\epsilon_{A,B} = 0$, while for $A = B$, $\epsilon_{A,A}$ represents the noise strengths which are three constants: $\epsilon_{\parallel,\parallel}$, $\epsilon_{\perp,\perp}$ and $\epsilon_{\theta,\theta}$. If we want fluctuations to represent a thermal noise, the noise strengths have to satisfy the following relation in order to define a unique temperature in the system [78]:

$$\frac{\langle R_\parallel(t)^2\rangle}{2\zeta_\parallel} = \frac{\langle R_\perp(t)^2\rangle}{2\zeta_\perp} = \frac{\langle R_\theta(t)^2\rangle}{2\zeta_\theta} = K_B T$$

where K_B is the Boltzmann constant and T is the absolute temperature.

Type of particle	active force F	$\langle R_{\parallel}^{(i)}\rangle^2/\zeta_{\parallel}$	$\langle R_{\perp}^{(i)}\rangle^2/\zeta_{\perp}$	$\langle R_{\theta}^{(i)}\rangle^2/\zeta_{\theta}$
pure active	0.4	0	0	0
active-Brownian	0.4	0.0833	0.0833	0.0833
pure Brownian	0	0.0833	0.0833	0.0833

Table 3.1: Active force and noise intensities for pure active, active Brownian, and pure Brownian particles

3.1.3 Simulation parameters and boundary conditions

All simulations were performed with a particle area $a = 0.2$ and the friction coefficients: $1/\zeta_{\parallel} = 0.1$, $1/\zeta_{\perp} = 0.04$, and $1/\zeta_{\theta} = 0.5$. The parameters associated with the potential given by Eq. (3.1.4) are: $\gamma = 0.16$, $\phi = 0.16$ and $\beta = 1$. Three "types" of particles have been studied: pure *active*, *active-Brownian*, and *Brownian* particles. The corresponding values of active force and noise intensities are given in Table 3.1.

Typically simulations were run with $N = 50$, 100 and 200 particles, and during 10^4 integration steps, using an integration step $\Delta t = 0.1$.

Most of the simulation results presented in this chapter correspond to simulations performed placing initially the N particles at random inside a box of area A and periodic boundary conditions (see Fig. 3.3), but reflecting boundary conditions were also studied (see Figs. 3.14 and 3.15). Unless otherwise indicated, assume periodic boundary conditions.

As a general observation, for the explored densities, the systems never freeze, i.e., never reach a state in which particles do not move. Another important remark is that collisions among particles lead to local alignment, but contrary to what occurs in [34, 40, 41, 44], particles can also point in opposite directions, and in consequence the emergent dynamics differs from that of those models (see Fig. 3.2).

There are three key parameters which control the dynamics: i) persistence of particle motion, regulated by the active force F and the noise strengths, ii) the packing fraction η, i.e., the area occupied by rods divided by the total area ($\eta = Na/A$), and iii) the length-to-width aspect ratio κ ($\kappa = L/W$, where L is the length and W is the width of the rods) (see Fig. 3.5).

In the following, we study quantitatively the impact of these three parameters in the dynamics of the self-propelled rods and cluster size distribution.

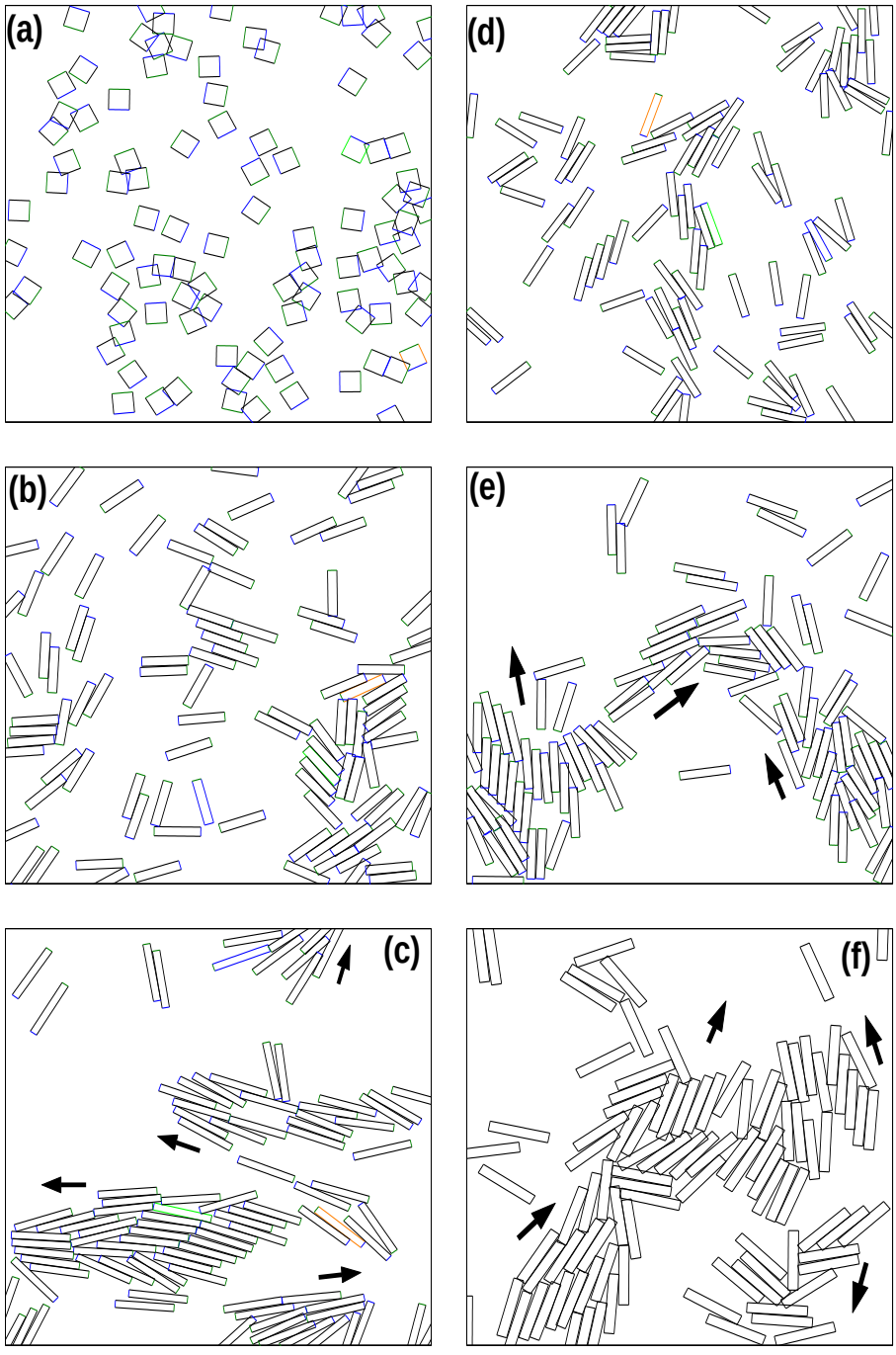

Figure 3.5: Simulation snapshots of the steady states for different particle anisotropy κ and the same packing fraction η (a-c), and the same κ and different η (d-f). Fixing $\eta = 0.24$: (a) before the transition, $\kappa = 1$; (b) almost at the transition, $\kappa = 5$; (c) after the transition, $\kappa = 8$. Fixing $\kappa = 6$: (d) before the transition, $\eta = 0.18$; (e) just crossing the transition, $\eta = 0.24$; (f) after the transition, $\eta = 0.34$. All cases correspond to simulations with $N = 100$ active particles of fixed area $a = 0.2$. The arrows indicate the direction of motion of some of the clusters.

3.2 Dynamics: particle speed, angular velocity and spatial arrangement of particles

This section is devoted to the study of particle motion, characterized by the particle speed and angular velocity, and the spatial arrangement of particles, including local and global orientation.

3.2.1 Particle speed

Collisions among pure active particles lead naturally to a dispersion of the speed distribution. In this case particles are driven only by the self-propelling force F, and in absence of interactions or at very low densities, we expect the speed distribution to be a Dirac delta function. We refer to this speed as the active speed and symbolize it as $\tilde{v} = |\mathbf{F}|/\zeta_{\parallel}$. Fig.3.6(a) and (b) illustrate the effect of collisions by comparing simulations performed at low and high density. Clearly, higher densities correspond to higher collision rates. If the density is high enough, particle interactions induce an extra speed distribution which gets superimposed to the Dirac delta distribution associated to $\tilde{v}$. Surprisingly, at high densities the extra distribution resembles a classical Maxwell-Boltzmann distribution [79] (see Fig. 3.6(b)). Consequently the system exhibits two typical speeds (i.e., a speed distribution with two maxima), one related to the active speed, and the other one associated with particle collisions. There are several remarkable differences between the classical Maxwell-Boltzmann distribution for two-dimensional gas particles, and the one we observe for purely active particles. The most evident difference is the peak associated to $\tilde{v}$ (solid vertical line in Fig. 3.6(a) and (b)) . But beyond this obvious fact, it is worth noticing that the classical Maxwell-Boltzmann distribution emerges in systems where the momentum is conserved, while in the system we analyze here it is not conserved.

To understand the speed distribution of active-Brownian particles, we firstly discuss the speed distribution of simple Brownian particles at low density, i.e., neglecting collisions. Since in this case $v_{\parallel}^{(i)} = R_{\parallel}^{(i)}/\zeta_{\parallel}$, then the probability $f_{\parallel}$ of observing a speed $v_{\parallel}$ along the $\parallel$-axis is $f_{\parallel}(v_{\parallel}) = \left(\sigma_{\parallel}\sqrt{2\pi}\right)^{-1} \exp(-v_{\parallel}^2/(2\sigma_{\parallel}^2))$, where $\sigma_{\parallel}^2 = \langle R_{\parallel}^2/\zeta_{\parallel}^2\rangle$. A similar argument follows for $v_{\perp}$. In consequence, the probability $p(s)$ of observing an speed $s = \sqrt{v_{\parallel}^2 + v_{\perp}^2}$ is expressed as $p(s) = \int_{v_{\parallel}^2+v_{\perp}^2=s^2} f(v_{\parallel}, v_{\perp}) dv_{\parallel} dv_{\perp}$, where $f(v_{\parallel}, v_{\perp}) = f_{\parallel}(v_{\parallel}) f_{\perp}(v_{\perp})$. In active-Brownian particles, the contribution of the self-propelling force F translates simply in a shift of $f_{\parallel}(v_{\parallel})$, which now reads $f_{\parallel}(v_{\parallel}) =$

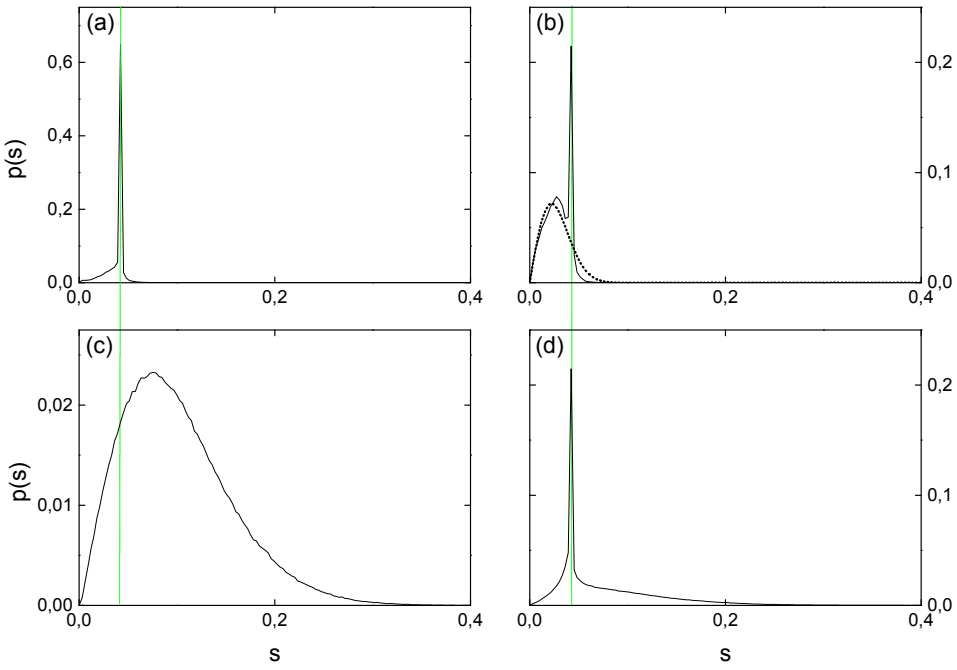

Figure 3.6: Speed distribution $p(s)$ at different packing fractions η and different κ. Top: $p(s)$ at different values of η for purely active particles with a fixed $\kappa = 5$. (a) low ($\eta = 0.16$) and (b) high density ($\eta = 0.40$). The superimposed Maxwell-Boltzmann distribution in (b) corresponds to a fit of the $p(s)$ performed removing the highest peak. Bottom: $p(s)$ at fixed density ($\eta = 0.34$) for active-Brownian particles with different κ. (c) isotropic particles ($\kappa = 1$), (d) anisotropic particles ($\kappa = 10$). Notice how the width of the distribution (associated to the noise) shrinks due to local order formation in elongated particles. The vertical lines indicate the speed induced by F.

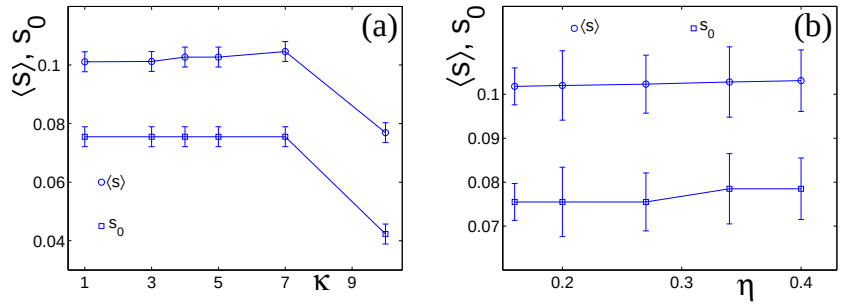

Figure 3.7: Average speed $\langle s \rangle$ and most probable speed s_0 as function of κ (a) and η (b). Simulations with active-Brownian particles. (a) fixed packing fraction $\eta = 0.34$ and box 7.67×7.67. (b) fixed aspect ratio $\kappa = 5$ and box 10×10.

$\left(\sigma_\parallel \sqrt{2\pi}\right)^{-1} \exp(-(v_\parallel - F/\zeta_\parallel)^2/(2\sigma_\parallel^2))$. The speed distribution takes the form: $p(s) = \int_{v_\parallel^2 + v_\perp^2 = s^2} \left(2\pi\sigma_\parallel\sigma_\perp\right)^{-1} \exp(-(v_\parallel - F/\zeta_\parallel)^2/(2\sigma_\parallel^2)) \exp(-v_\perp^2/(2\sigma_\perp^2)) dv_\parallel dv_\perp$. Using this expression we calculate the average speed $\langle s \rangle$, defined as $\langle s \rangle = \int_0^\infty s p(s) ds$, and the most probably speed s_0, i.e., maximum or mode of the distribution $p(s)$. For Brownian particles in absence of interaction we estimate $\langle s \rangle = 0.09577$ and $s_0 = 0.07638$, while for active-Brownian particles, $\langle s \rangle = 0.102$ and $s_0 = 0.08$.

Now we are in condition to explore the effect of collision in active-Brownian particles. Surprisingly, this time the interaction among particles can lead to a shrinking of the speed distribution width. This phenomenon is particularly noticeable comparing particles of very different aspect ratio κ and exposed to the same noise, as it is shown in Figs. 3.6(c) and (d). Fig. 3.6(c) shows the speed distribution of particles with an aspect ratio, $\kappa = 1$. Fluctuations almost entirely shape the distribution. The active speed $\tilde{v}$ is indicated by the solid vertical line. Notice that the maximum of the distribution does not coincide with the active speed. In Fig. 3.6(d) we observe the speed distribution of system identical to the system in Fig. 3.6(c) except for the particle aspect ratio, which now is $\kappa = 10$. It is observed a remarkable shrinking of the width of the distribution, which now exhibits its maximum at the active speed. Particles can reduce the effect of the noise by forming densely packed moving clusters. Inside these structures particles are locally aligned and their movements are highly constrained. In consequence, the speed due to the active force F prevails.

In Fig. 3.7 we show a more systematic study of the dependency of particle speed with the particle aspect ratio κ and packing fraction η. The figures exhibit average speed

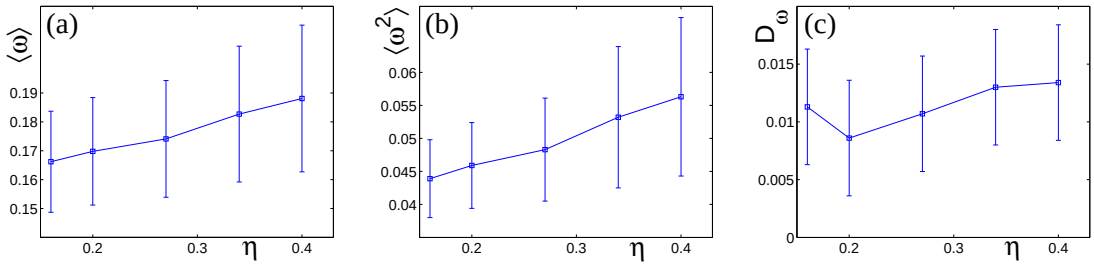

Figure 3.8: Average angular velocity $\langle\omega\rangle$ (a) and average square angular velocity $\langle\omega^2\rangle$ (b), and angular diffusion D_θ as function of η. Simulations with active-Brownian particles of fixed aspect ratio $\kappa = 5$ in a box 10×10.

$\langle s\rangle$, and most probable speed s_0 as function of κ in (a), and η in (b). Simulations were performed in (a) with $N = 100$ active-Brownian particles at a constant packing fraction $\eta = 0.34$ for various values of κ. Simulations in (b) also correspond to active-Brownian particles. This time κ was kept fixed at 5 and the packing fraction η was varied. In (a) it is shown that $\langle s\rangle$ and s_0 remain insensitive to κ for small values of the parameter, while an abrupt drop in both quantities is observed for large values of κ. The jump in $\langle s\rangle$ and s_0 is due to the shrinking of the distribution shown in Fig. 3.6 from (c) to (d). Notice that in general $\langle s\rangle > s_0$, and particularly $\langle s\rangle \geq s_0$. It can be easily observed in Fig. 3.7(a) that for small values of κ, s_0 does not coincide with the active speed $\tilde{v}$, while for large values of κ, $s_0 \sim \tilde{v}$ (compare with Figs. 3.6(c) and (d)). Assuming particles do not get stagnated for larger value of κ, we expect s_0 to be in its minimum, and for larger value of κ only see $\langle s\rangle$ decreasing towards s_0. We speculate that the roughly sharp transition exhibited by s_0 could be correlated to the emergence of strong clustering effects, though not directly to the transition to clustering as it will be defined below. On the other hand, Fig. 3.7(b) shows that $\langle s\rangle$ and s_0 remain constant in the simulated range of η, but presumably they would exhibit a similar transition for larger value of η than the simulated ones.

3.2.2 Angular velocity and angular diffusion

As expected, the angular velocity distribution takes always a Gaussian shape centered around zero. In absence of angular fluctuations, i.e., for active particles, the width of the distribution is entirely determined by the collisions among particles, while for active-Brownian particles there is an additional contribution which comes from the amplitude of the angular noise $\langle R^i_\theta(t)^2\rangle$. In consequence, the maximum or mode of the distribution is

zero, and the average angular velocity and average square angular velocity depend upon angular noise and particle collision rate.

Figs. 3.8(a) and (b) show the average angular velocity $\langle\omega\rangle$ and the average square angular velocity $\langle\omega^2\rangle$, respectively, as function of the packing fraction η. The simulations were performed with active-Brownian particles of fixed aspect ratio $\kappa = 5$ for various values of the packing fraction η. The size of the box was kept constant at 10×10 and the following number of particles were simulated: $N = 80$, 100, 135, 170 and 200, corresponding to $\eta = 0.16$, 0.20, 0.27, 0.34 and 0.40. The figure indicates that as the packing fraction increases, $\langle\omega\rangle$ also increases (see Fig. 3.8(a)). Similarly, $\langle\omega^2\rangle$ grows with η (see Fig. 3.8(b)). Notice that $\langle\omega^2\rangle$ is a measure of the kinetic energy due to particle rotation. As η increases, the collision rate enhances. Since collisions imply rotation of the particles, we expect both, $\langle\omega\rangle$ and $\langle\omega^2\rangle$, to increase with η. Figs. 3.8(a) and (b) prove that this is the case. We conclude that far away from the maximum packing fraction, particle rotation, resp. the kinetic rotation energy, increase with η.

Fig. 3.8(c) shows the angular diffusion D_ω as function of η. It could be argued that an increase in $\langle\omega\rangle$ and $\langle\omega^2\rangle$ would lead to a higher angular diffusion. Fig. 3.8(c) shows this trend for $\eta > 0.2$. The deviation observed at $\eta = 0.16$ is probably due to fluctuations caused by the small number of particles.

Fig. 3.9 shows $\langle\omega\rangle$, $\langle\omega^2\rangle$, and D_ω, but this time as function of the particle aspect ratio κ. The simulations were performed with $N = 100$ active-Brownian particles at a fixed packing fraction $\eta = 0.34$ and for various values of κ. The figure reveals a complex response of $\langle\omega\rangle$, $\langle\omega^2\rangle$, and D_ω to variations of κ. For small values of κ, $\langle\omega\rangle$ and $\langle\omega^2\rangle$ grow with κ. As κ increases, the scattering cross section of the particles also increases[2]. Consequently, we expect the collision rate to be enhanced by larger values of κ, which in turn caused an increase in $\langle\omega\rangle$ and $\langle\omega^2\rangle$. However, notice that there are two processes competing. On one hand, as κ gets larger, the number of collisions among randomly moving cluster increases. On the other hand, κ facilitates local ordering. For large values of κ, particles tend to move parallel to each other. As the number of available direction of motion decreases, due to local alignment, the collision frequency also gets reduced. As shown in 3.9(a) and (b), for large values of κ this effect becomes dominant and $\langle\omega\rangle$ and $\langle\omega^2\rangle$ get lower values. In the extreme case of perfect polar ordering in the system, and for active particles, $\langle\omega\rangle$ and $\langle\omega^2\rangle$ vanish. We expect in general $\langle\omega\rangle$ and $\langle\omega^2\rangle$ to exhibit a maximum at intermediate values of κ. Figs. 3.9(a) and (b) confirm that this is the case.

[2] A discussion about the scattering cross section of rods is provided in section 3.3.

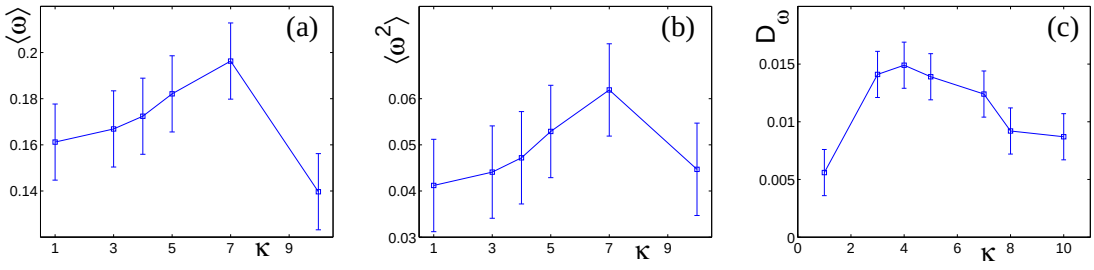

Figure 3.9: Average angular speed $\langle\omega\rangle$ (a) and average square angular speed $\langle\omega^2\rangle$ (b), and angular diffusion D_θ as function of the particle aspect ratio κ. Simulations with active-Brownian particles in a box 7.67×7.67 at $\eta = 0.34$.

Particle rotation, resp. the kinetic rotation energy, exhibit a maximum at intermediate values of the aspect ration, increasing for small values of κ and decreasing for large values of the parameter.

Fig. 3.9(c) shows that the angular diffusion D_ω also has a non-monotonic dependency with κ. Surprisingly, the maximum of D_ω does not coincide with the maximum exhibited by $\langle\omega\rangle$ and $\langle\omega^2\rangle$. It is worth noting that $D_\omega(\kappa)$ has its maximum located near by the value κ_c which denotes the onset of clustering in the system as defined in the next section.

3.2.3 Spatial arrangement of particles and orientation ordering

When particles exhibit large values of κ the local spatial arrangement is such that particles get aligned in a side-by-side and "head-to-tail" manner, allowing the formation of densely packed clusters. This observation can be quantified by measuring the two-body correlation function $p(d)$, which is nothing else than the probability of finding the center of mass of two particles separated by a distance d. Fig. 3.10 shows $p(d)$ measured in simulations performed with $N = 100$ active particles at a fixed packing fraction $\eta = 0.34$ and various aspect ratios κ. In (a) we observe that for isotropic particles, i.e., $\kappa = 1$, $p(d)$ exhibits one single peak at $d = L = W$. The $p(d)$ is zero for $d < L$, indicating particles cannot overlap. Though the single peak evidences that many particles stay in a side-by-side arrangement, they are not aligned, meaning they do not have the active force F pointing in the same direction as shown by Fig. 3.11(a). From Figs. 3.10(b) and (c) we learn that for anisotropic particles, i.e., $\kappa > 1$, $p(d)$ exhibits two peaks. The first one at $d = W$ corresponds to particles arranged in a side-by-side manner, while the second peak at $d = L$ to particles arranged in a head-to-tail manner. Notice that as κ gets larger

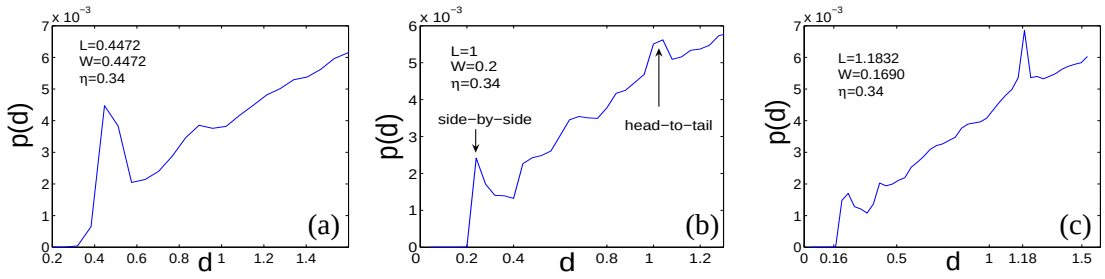

Figure 3.10: The two-body correlation function for $\eta = 0.34$ and various values of κ, $\kappa = 1$ (a), $\kappa = 5$ (b) and $\kappa = 7$ (c). Simulations performed with $N = 100$ active particles in a box 7.67×7.67. Notice the peaks corresponding to particles arranged side-by-side and head-to-tail.

the peak at $d = L$ becomes more pronounced.

Now we want to learn about the orientation of particles inside this arrangements. We look for a measure of the local ordering. Assume $\mathbf{J}_i = (\cos(\theta_i), \sin(\theta_i))$ is a unit vector that represents the orientation of the long axis of the ith-particle, or equivalently, the orientation of its active force F. If $\mathbf{J}(\mathbf{x})$ represents the local orientation or polarization, we want to calculate the quantity $\langle \mathbf{J}(0)\mathbf{J}(d)\rangle$ defined as:

$$\begin{aligned}\langle \mathbf{J}(0)\mathbf{J}(d)\rangle &= \int_A d\mathbf{x} \int_0^{2\pi} d\alpha \int_0^{2\pi} d\theta \int_0^{2\pi} d\theta' \\ &\cos(\theta - \theta')\, p\left(\mathbf{x}, \theta, t; \theta x + d(\cos(\alpha), \sin(\alpha)), \theta', t\right) \ ,\end{aligned} \tag{3.2.1}$$

where A is the area of the system, $\cos(\theta - \theta')$ is the scalar product of the orientation of particles whose long axis are θ and θ', and $p\left(\mathbf{x}, \theta, t; \theta x', \theta', t\right)$ refers to the joint probability of finding at time t a particle at position $\mathbf{x}$ and pointing in direction θ, and simultaneously another particle at $\mathbf{x}'$ and pointing in direction θ'. In simulations we calculate this quantity simply by:

$$\langle \mathbf{J}(0)\mathbf{J}(d)\rangle = \frac{1}{n_d} \sum_{|\mathbf{x}_i - \mathbf{x}_j| = d} \mathbf{J}_i . \mathbf{J}_j \ , \tag{3.2.2}$$

where the sum runs over all pairs of particles in the simulation separated by a distance d, and n_d is the number of such pairs. Notice that the maximum value that $\langle \mathbf{J}(0)\mathbf{J}(d)\rangle$ can take is 1 and corresponds to a situation in which all particles separated by a distance d are perfectly aligned.

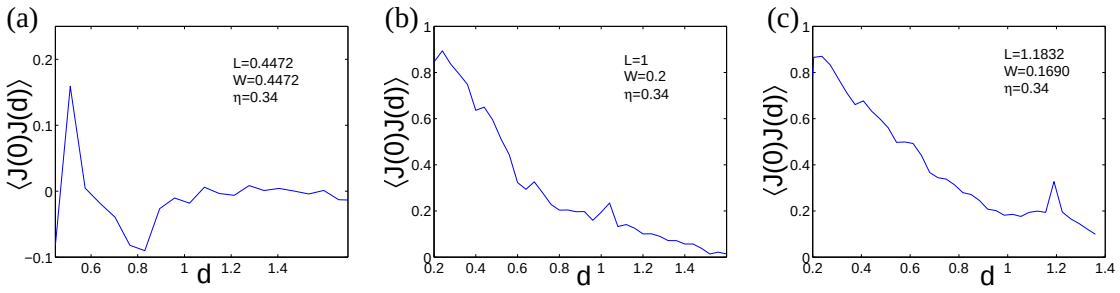

Figure 3.11: Local order. Average of the scalar product of the particle orientation, $\langle \mathbf{J}(0).\mathbf{J}(d)\rangle$, as function of the particle distance d. Simulations with $\eta = 0.34$, $N = 100$ and box 7.67×7.67. Notice that isotropic particle do not order locally (a), while elongated particle do (b)-(c). The small peak at $d = L$ in (b) and (c) indicates many particles arrange themselves in a head-to-tail manner while collectively moving. Compare with Fig. 3.10.

Fig. 3.11 shows $\langle \mathbf{J}(0)\mathbf{J}(d)\rangle$ measured in simulations performed, as before, with $N = 100$ active particles at a fixed packing fraction $\eta = 0.34$ and various aspect ratios κ. For $\kappa = 1$, isotropic particles, $\langle \mathbf{J}(0)\mathbf{J}(d)\rangle$ is roughly zero for all values of d. Compare the high of $\langle \mathbf{J}(0)\mathbf{J}(d)\rangle$ observed in (a) with (b) and (c). The fluctuation at small values of d are presumably due to the finite size of the system. As mentioned above, the peak at $d \sim L = W$ in Fig. 3.10(a) corresponds to particles arranged in a side-by-side manner. The small value taken by $\langle \mathbf{J}(0)\mathbf{J}(d)\rangle$ at $d \sim 0.44$ in Fig. 3.11(a) reveals that roughly half these particles move parallel, while the other half move anti-parallel to each other. In contrast, elongated particles exhibit very high local alignment. $\langle \mathbf{J}(0)\mathbf{J}(d)\rangle$ takes its maximum value at $d = W$ and decay for larger values of d. Particles separated by a distance $d = W$ are densely packed, aligned side-by-side and move in the same direction, as indicated by the high value reached by $\langle \mathbf{J}(0)\mathbf{J}(d)\rangle$ at $d \sim W$ in Figs. 3.11(b) and (c), and peak at $d \sim W$ in Figs. 3.10(b) and (c). The correlation of particle orientation $\langle \mathbf{J}(0)\mathbf{J}(d)\rangle$ does not decay monotonically with the distance d as in the planar XY-model. At $d \sim L$, $\langle \mathbf{J}(0)\mathbf{J}(d)\rangle$ exhibits a kink. In Fig. 3.11(c) it can be easily confused with a fluctuation, but in 3.11(b) the kink is well-defined. Its presence indicates that many particles are aligned head-to-tail and moving in the same direction.

So far, we have discussed about local orientation ordering, and shown that locally κ facilitates ordering. In the following we address briefly the effect on global orientation ordering of κ.

The particle orientation distribution $p(\theta, t)$ exhibits a very dynamical evolution. Fig. 3.12 shows $p(\theta, t)$ for a simulation performed with $N = 100$ active particles of $\kappa = 7$ at

$\eta = 0.34$. The bright patches correspond to the orientation of large clusters. We want to quantify the degree of global orientation ordering in such systems. We use two quantities, the ferromagnetic order parameter $S^F = 1/N\langle|\sum_{i=1}^{N}\exp(i\theta_i)|\rangle$ and the two dimensional scalar liquid crystal order parameter $S^{LC} = 1/N\langle|\sum_{i=1}^{N}\exp(i2\theta_i)|\rangle$, where θ_i refers to the orientation of the long axis of the ith-particle, and $\langle ...\rangle$ denotes temporal average. S^F measures the degree of "polarization" of the system. $S^F = 0$ indicates that particles point with equal probability in any direction, while $S^F = 1$ corresponds to a situation in which all particles pointing in the same direction. On the other hand, S^{LC} quantifies the degree of alignment without distinguishing head and tail of the particles (recall that the self-propelling force defines a "head" and "tail" of the particles). $S^{LC} = 0$ indicates no order, while $S^{LC} = 1$ implies that all particles are aligned to a global director. Notice that if $S^F = 1$ necessarily $S^{LC} = 1$, while the contrary, i.e., $S^{LC} = 1$ does not imply $S^F = 1$.

Fig. 3.13 shows S^F and S^{LC} as function of κ. The simulation were performed with $N = 100$ active particles of $\kappa = 7$ at packing fraction $\eta = 0.34$. It can be observed a systematic increase of S^F and S^{LC} with κ, despite the fact the system size is too small to make any claim about possible phase transitions. Presumably, the increase experienced by S^{LC} is due to polar alignment of particles, though the possibility of true nematic order can not be excluded. It can be conclude that, as expected, for finite systems, large values of κ imply high degree of orientational ordering.

3.3 Clustering

This section is entirely devoted to the study of the clustering dynamics of self-propelled rods. It starts with a survey of the findings in individual-based simulations.

While most of the study is focused on periodic boundary conditions, here we discuss briefly the effect of implementing other types of boundaries. In Fig. 3.14 snapshots at various times of a simulation with a reflecting circular boundary are shown. The simulation was performed with $N = 100$ active-Brownian particles of $L = 1$ and $W = 0.2$ at a packing fraction $\eta = 25$. The diameter of the reflecting ring is 10. Initially particles are placed at random inside the circle and pointing at random direction ($t = 0$). As the simulation runs we observe that particles start to gather around the boundary. At the beginning particles slide on the circular boundary with their long axis parallel to the reflecting wall $t = 150$, but soon after traffic jams of counter migrating particles emerge and aggregates of stalled particles appear on the boundary ($t = 300$ and $t = 450$). At this point the dy-

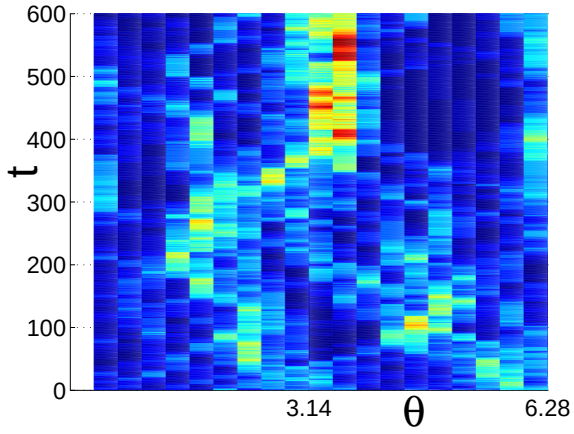

Figure 3.12: Evolution of the particle orientation distribution $p(\theta, t)$. The high of the function $p(\theta, t)$ is color coded: dark blue for 0, and bright red for the maximum value 0.25. Simulation performed with $N = 100$ active particles of $\kappa = 7$ at $\eta = 0.34$ in box 7.67×7.67. The bright patches correspond to the orientation of large clusters.

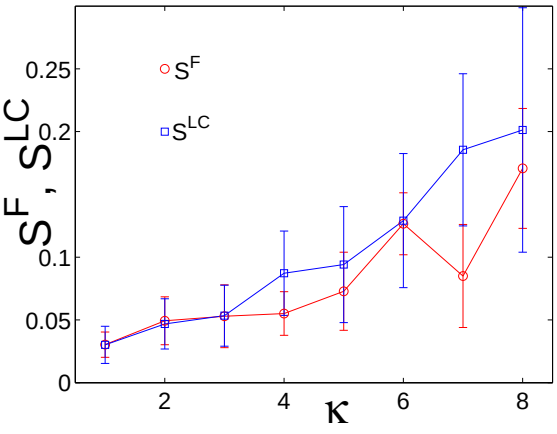

Figure 3.13: Global orientational ordering quantified through the ferromagnetic order parameter S^F and the two dimensional scalar liquid crystal order parameter S^{LC}. Simulation performed with $N = 100$ active particles of $\kappa = 7$ at $\eta = 0.34$. Notice the increase of S^F and S^{LC} with κ.

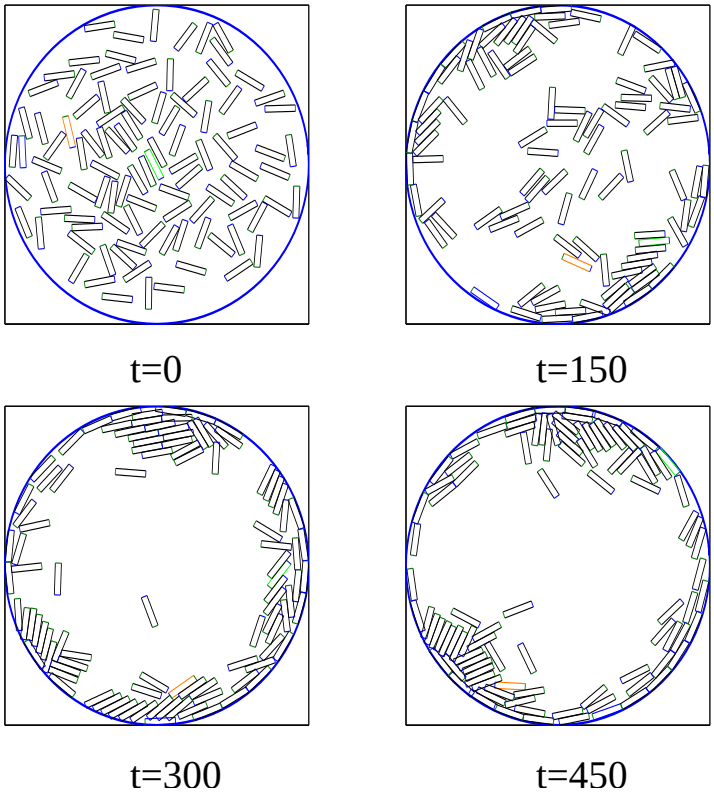

Figure 3.14: Snapshots of a simulation with reflecting boundary conditions at various times. $N = 100$ active-Brownian particles of $L = 1$ and $W = 0.2$; diameter of the reflecting ring 10, and so $\eta = 0.25$. Notice that as time goes, particles gather around the boundary.

namics of the system slows down and we only observe some individual particles traveling from one aggregate to another. If one waits long enough, it can be seen that some initial aggregates disappear while others grow in size. Remarkably, while the boundary is not at all absorbing, particles end up in clusters which are attached to the boundary, and the particle density in the middle of the system drops to zero. Contrary, in simulations for the same system but with Brownian particles, the density never drops to zero, though it is observed slightly higher density on the boundary that on center, and particles do not cluster so much. The self-propelling force F is responsable of such strong non-equilibrium clustering effects on the boundary.

In Fig. 3.15 we test other type of boundary condition. The left and right side of the box are reflecting walls, while the top and bottom side are connected in such a way that a particle leaving the system through the top side emerges at the bottom side. The simulation shown in Fig. 3.15 corresponds to this tube-like boundary condition (box 7.67×7.67) and was performed with $N = 100$ active-Brownian particles of $L = 1$ and $W = 0.2$. As before, the particles are initially distributed at random inside the box and pointing with equal probability in any direction ($t = 0$). As the simulation evolves particles start to aggregate on the reflecting walls, though particle density on the center of the box never drops to zero (see snapshot corresponding to $t = 8534$). Another important difference with respect to simulations with active-Brownian particles and reflecting boundary conditions is that particles never get stalled. Moreover, particles can exhibit sporadic coherent motion by eventually arranging parallel to one of the reflecting walls and pointing in the same direction (see left side of the snapshot corresponding to $t = 8534$).

3.3.1 Clustering induced by persistence in the motion and packing fraction

When fixing κ and η, we observe that the self-propelling force F induces (moving) cluster formation, while, on the other hand, the noise R_A^i, tends to diminish it.

An estimate of particle clusterization is given by M, the mean maximum cluster size divided by the total number of particles. This quantity is defined as follows:

$$M = \frac{1}{N}\frac{1}{(T - t_t)}\int_{t_t}^{T} max(\Theta(n_1(t)), ..., j\Theta(n_j(t)), ..., N\Theta(n_N(t))dt \qquad (3.3.1)$$

where T represents the simulation time, t_t the transient before the "steady state" is reached, and $\Theta(x)$ a Heaviside function. $n_j(t)$ refers to the number of clusters of mass j

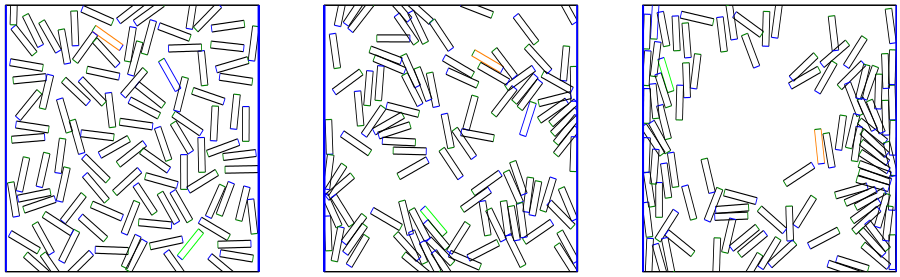

Figure 3.15: Snapshots of a simulation with a tube-like boundary condition at various times. Left and right side are reflecting boundaries, while top and bottom side are connected, i.e., the system is periodic along the vertical direction. $N = 100$, $L = 1$, $W = 0.2$, box 7.67×7.67, and so $\eta = 0.34$. Notice that particles aggregate on the reflecting boundaries where eventually coherent motion emerges (see left side of the snapshot corresponding to $t = 8534$).

at time t. $M \in [0, 1]$. Fig. 3.16 shows M for different ratios between F and the noise amplitudes, i.e., for pure active, active-Brownian and Brownian particles, and different value of the packing fraction η (snapshots of simulations with active particles at fixed κ and various values of η are shown in Fig. 3.5) . As can be observed in the figure, for all η pure active particles exhibit the strongest clustering effect, while pure Brownian particles the weakest. The mean maximum cluster size for active-Brownian particles falls in between these two extreme cases.

Notice that the dependency of M with η is different for these three types of particles. For the range of packing fractions explored, M is almost constant for Brownian particles, exhibits a linear relation with η for active particles, and a non-linear dependency for active-Brownian particles.

Clustering is facilitated by the persistence in the motion exhibited by the particles and not by simply the particle speed. The parameters of these three particle types have been chosen such that without interactions active particles have an average squared speed $\langle \mathbf{v}^2 \rangle = 0.0016$, while in active-Brownian particles $\langle \mathbf{v}^2 \rangle = 0.0132$, and in Brownian particles $\langle \mathbf{v}^2 \rangle = 0.0116$. In consequence, $\langle \mathbf{v}^2 \rangle_{active} < \langle \mathbf{v}^2 \rangle_{Brownian}$, and $\langle \mathbf{v}^2 \rangle_{Brownian} \sim \langle \mathbf{v}^2 \rangle_{active-Brownian}$. Even using such a small F, compared to the noise amplitude, we observe that particles driven only by F exhibit the strongest clusterization, while simultaneously, the smallest average squared speed.

Why do these active particles cluster so much? Active particles when they meet tend

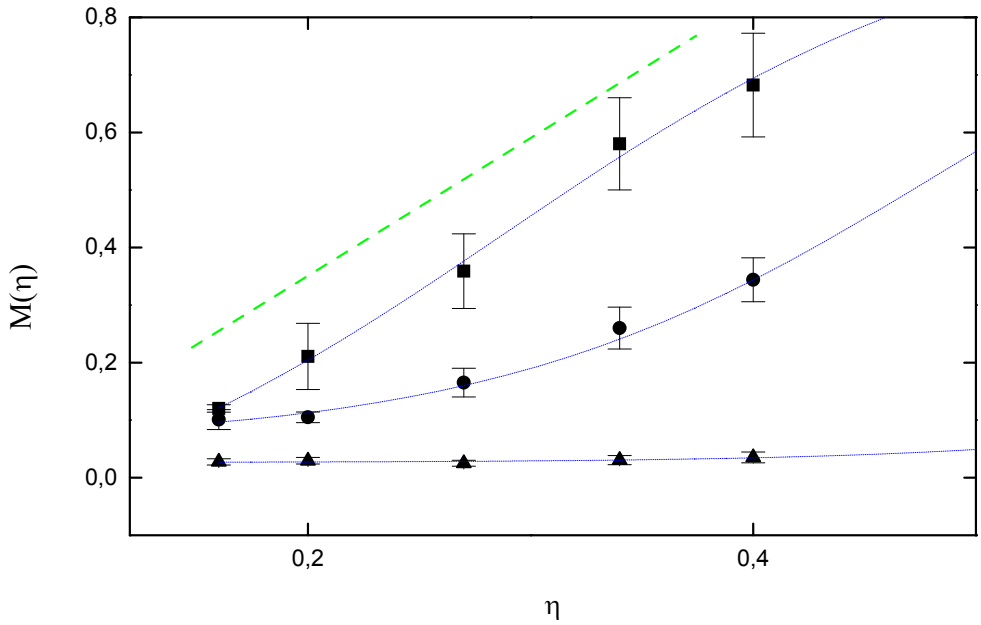

Figure 3.16: Mean maximum cluster size divided by the total number of particles, M, vs. packing fraction, η. $\kappa = 5$. Cases: purely active particle ($square$), Brownian particles ($triangle$) and active-Brownian ($circles$). The dashed line indicates slope 2.5, suggesting that clustering for pure active particles is linear with η even having a smaller $\langle v^2 \rangle$ than Brownian particles.

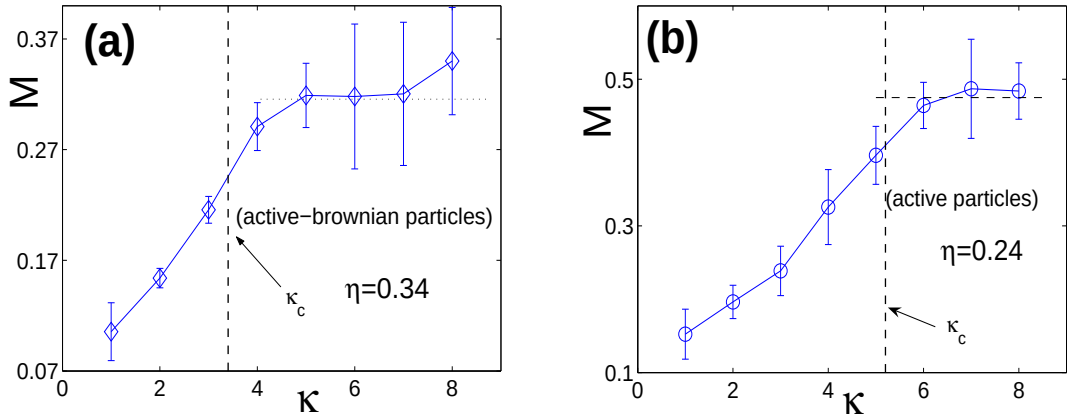

Figure 3.17: The two regimes of M as function of κ. (a)Active-Brownian particles at density $\eta = 0.34$. (b) Active particles at density $\eta = 0.24$.

to align their long axis and move parallel to each other. By doing so, they can form stable dense clusters (see Fig. 3.5). On the other hand, Brownian particles lack the characteristic persistence in the motion of active particle, and collisions among them rarely lead to perfect alignment. In addition, the absence of a self-propelling force does not allow coherent migration of the clusters. In active-Brownian particles, collisions typically do not cause perfect alignment of the particles, but eventually clusters of aligned particles emerge. Inside these clusters, the effect of the noise is highly reduced, and the bias originated by the self-propelling force induces the coherent motion of the cluster. Consequently, clusters of active-Brownian particles are more stable than clusters of Brownian particles.

3.3.2 Clustering induced by the length-to-width aspect ratio

Fixing all parameters and varying only κ, we find that the particle aspect ratio κ is a key parameter that controls the type of the emergent pattern, and particularly clustering (in Fig. 3.5 some snapshots of simulation at fixed η illustrate this phenomenon). We stress that when varying κ we always keep the particle area constant, and so η remains the same.

Moving cluster formation strongly depends on κ. When going from isotropic to anisotropic particles we observe two regimes of the clusterization process. Initially M grows monotonically with κ up to certain point after which M seems to reach a plateau (see Fig. 3.17). The presence of these two regimes suggests the existence of a critical κ_c

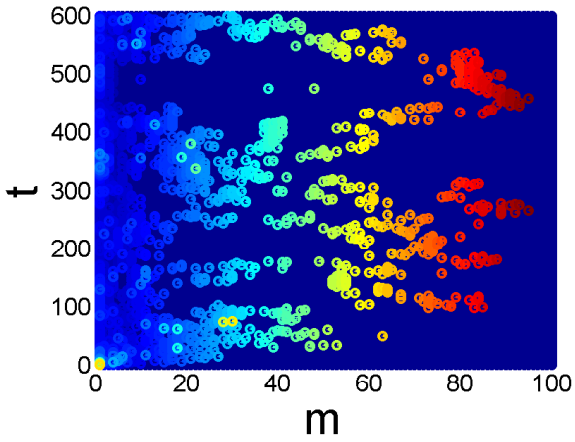

Figure 3.18: Evolution of the weighted cluster size distribution $n_m(t)$. The high of the function $n_m(t)$ is color coded: dark blue for 0, and bright red for the maximum value 90. Simulation performed with $N = 100$, $\kappa = 7$, $\eta = 0.34$, $N = 100$ and a box 7.67×7.67.

after which cluster sizes no longer grow with κ and M saturates.

The "saturation" of M is a robust property of the model that does not depend on either the noise amplitude or the packing fraction. To illustrate this fact, we show in Fig. 3.17 M as function of κ for active and active-Brownian particles at different packing fractions. Notice that Fig. 3.17(a) and (b) exhibit the same qualitative behavior. However, the amplitude of M as well as κ_c, strongly depend on the noise amplitude and η.

Another way to study clustering in the system is through the weighted cluster size distribution $p(m)$, which measures the probability of finding a randomly chosen particle belonging to a cluster of mass m. $p(m)$ is defined as follows:

$$p(m) = \frac{1}{N}\frac{1}{(T - t_t)}\int_{t_t}^{T} n_m(t) m dt \tag{3.3.2}$$

where T represents the simulation time, t_t the transient before the "steady state" is reached, and $n_m(t)$ refers to the number of clusters of mass j at time t. By abuse of notation, we refer to $p(m)$ as cluster size distribution. Notice that the "real time" cluster size distribution, represented by $n_m(t)$, exhibits a very dynamical evolution in which clusters are created and disintegrated constantly (see Fig. 3.18). Though this is true, the temporal average of $n_m(t)$, through $p(m)$, provides a good characterization of the clustering properties of the system. The distribution $p(m)$ has proved to be highly reproducible

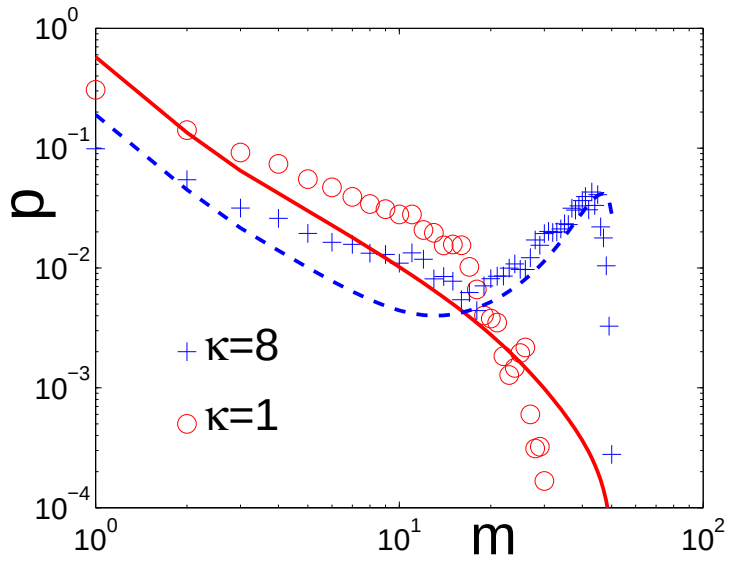

Figure 3.19: Onset of clustering triggered by κ. $p(m)$ as function of the cluster size m. Symbols show the average over 8 realizations for active particles at $\eta = 0.34$, and $\kappa = 1$ (circles) and $\kappa = 8$ (crosses). The lines correspond to the mean field theory for $\kappa = 1$ (solid) and $\kappa = 8$ (dashed). The second peak (for $\kappa = 8$) is the signature of particle clusterization.

in simulation performed under the same conditions, i.e., same initial condition, set of parameters, and boundary condition.

$p(m)$ is shown in Fig. 3.19 for different values of κ ($\kappa = 1$ ($circles$) and $\kappa = 8$ ($crosses$)). Simulations exhibit a transition which is triggered by κ when η is fixed. For low values of κ, $p(m)$ is monotonically decreasing, indicating no clusterization. For large values of κ, $p(m)$ exhibits a second peak which is the signature of particle clusterization. The second peak indicates that particles "prefer" to stay in large cluster instead of being part of small groups. We define the transition from no clustering to clustering as the point at which $p(m)$ is no longer monotonically decreasing. By using this definition, we can estimate the critical aspect ratio κ_c after which clustering becomes dominant. Notice that the transition to clustering, implies a transition to a swarming phase.

3.3.3 A first approach towards the understanding of clustering: the number of clusters and cluster entropy

As a first step to understand clustering theoretically, we study the evolution of the number of clusters in the system. We define $G(t)$ as the total number of clusters in the system. $G(t)$ takes the form:

$$G(t) = \sum_{i=1}^{N} n_i(t) \tag{3.3.3}$$

where N refers to the total number of particles in the system and $n_i(t)$ is the number of clusters of mass i at time t as defined above. $G(t)$ is not conserved during time, while the number of particles is constant, i.e., $\sum_{i=1}^{N} i n_i(t) = N$. Let us now define $f_i(t)$ as the probability of finding a cluster of size i at time t, which simply reads:

$$f_i(t) = \frac{n_i(t)}{G(t)} \tag{3.3.4}$$

Cluster entropy

In the following we look for a measure of "disorder" in clustering. Given a total number of clusters G, the total number of ways in which G may be formed into groups n_1, n_2, ... is given by W:

$$W = \frac{G!}{\prod_{j=1}^{N} n_j!} \tag{3.3.5}$$

If n_j is large, we could approximate the previous expression by use of the Stirling formula and obtain:

$$\ln(W) \approx -G \sum_{i=1}^{N} \frac{n_i}{G} \ln \frac{n_i}{G} \tag{3.3.6}$$

Since $n_i/G = f_i$ is the frequency of cluster of mass i, we can express:

$$\frac{\ln(W)}{G} = -\sum_{i=1}^{N} f_i \ln f_i \tag{3.3.7}$$

Borrowing the definition of *entropy of grouping* given by A. Okubo in [80], we call the right hand side of Eq. (3.3.8) the *cluster entropy* H_C (for $N \to \infty$):

$$H_C = -\sum_{i=1}^{\infty} f_i \ln f_i \tag{3.3.8}$$

H_C has the following properties which makes it a reasonable measure of disorder in clustering: i) if all particles gather in one cluster, corresponding to a state of maximum order, then $H_C = 0$, i.e., the disorder is 0. ii) if for each cluster size there is only one cluster, then $f_i = 1/G$, and for a given G, H_C has a maximum value $H_C = \ln(G)$. This state corresponds to the maximum clustering entropy, and clearly if $G \to \infty$, then $H_C \to \infty$. iii) any change towards the equalization of f_i increases H_C. It is worth noticing that when all particles form isolated clusters, then $H_C = 0$, as it is when all of them belong to one big cluster.

There are two natural constraints to the discrete frequency distribution f_i, a) $\sum_{i=1}^{\infty} f_i = 1$ and b) $\sum_{i=1}^{\infty} i f_i = N/G = q$. Notice that q is the mean number of particles per cluster.

The principle of maximum entropy states that the most probable distribution f_i^* corresponds to the maximum of H_C. To maximize the entropy under these constrains, the method of Lagrange multipliers can be used. The distribution f_i^* of maximum entropy is then given by:

$$f_i^* = \exp\left[-\left(1 + \lambda_0 + \lambda_1 i\right)\right] \tag{3.3.9}$$

where λ_0 and λ_1 are Lagrange multipliers [80]. Replacing Eq. (3.3.9) into conditions a) and b), and after some algebra we obtain:

$$f_i^* = \left(\frac{1}{q-1}\right)\left(\frac{q-1}{q}\right)^i \tag{3.3.10}$$

Replacing this expression into Eq. (3.3.8), we obtain:

$$H_C = -\sum_{i=1}^{\infty} \left(\frac{1}{q-1}\right)\left(\frac{q-1}{q}\right)^i \ln\left[\left(\frac{1}{q-1}\right)\left(\frac{q-1}{q}\right)^i\right] \tag{3.3.11}$$

Using that $\sum_{i=0}^{\infty} Q^i = 1/(1-Q)$ and $\sum_{i=0}^{\infty} i\, Q^i = Q/(1-Q)^2$ for $Q < 1$, we express Eq. (3.3.11) as:

$$H_C = \ln(q-1) + q\ln(\frac{q}{q-1}) \tag{3.3.12}$$

Given an estimation for G, we can approximate the mean number of particles per cluster by q and use Eq. (3.3.12) to estimate the cluster entropy H_C.

Evolution equation for the number of clusters

We need an equation for $G(t)$. We look for a simple phenomenological evolution equation of the form:

$$\dot{G} = R_S\,(G) - R_F\,(G) \tag{3.3.13}$$

where $R_S\,(G)$ describes the creation per unit time of new clusters due to splitting of big clusters, while $R_F\,(G)$ denotes the destruction per unit time of clusters caused by collision and fusion of clusters. We expect both, R_S and R_F, to be functions of G. In the following, we discuss the functional form of these term.

The creation term R_S:

The self-propelled rods we are analyzing do not have any cohesive force. Therefore, we can assume that the more particles a cluster has, the more unstable it becomes. Furthermore, clusters usually loose those particles that are located on the boundary of the clusters. Typically this is due to collisions or fluctuations that make these particles change the direction of their self-propelling force to some arbitrary direction which typically does not coincide with the average direction of motion of the group. Thus, we assume that the probability for a cluster of suffering a fission is proportional to the number of particle on the boundary. For a cluster with m particles, we approximate the number of particles on the boundary as $\sqrt{m}$. Since q represents the mean number of particles per cluster, we expect R_S to be proportional to $\sqrt{q}$.

At this point we need some characteristic time. Recalling the Buckingham π theorem [81], we conclude that this characteristic time has to be a function of either $L/\tilde{v}$ or $W/\tilde{v}$, or a combination of both. Since elongated particles form more stable clusters than short particles, we simply take the characteristic time τ a cluster lives to be $\tau^{-1} \sim \tilde{v}/L$.

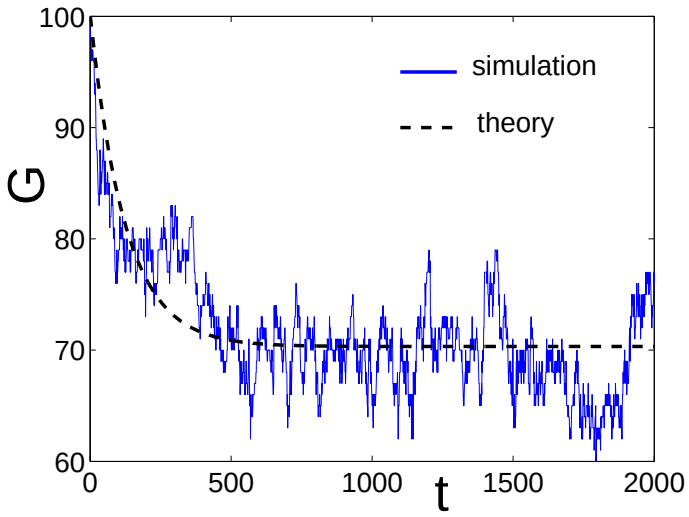

Figure 3.20: Average number of clusters G vs. time. Symbols corresponds to simulations performed with $N = 100$, $\kappa = 4$ and $\eta = 0.034$. The dot-dashed line is the approximation given by integration of Eq. (3.3.17), with $\gamma = 0.1186$ and $\beta = 6$.

Taking all this into account, we express R_S as:

$$R_S\left(G\right) = \frac{\tilde{v}}{\gamma L}\sqrt{\frac{N}{G}} \tag{3.3.14}$$

where γ is a free parameter of the model. Notice that Eq. (3.3.14) represents the mean number of clusters that are created per unit time, and therefore it is not a rate, i.e., in Eq. (3.3.13) we insert directly Eq. (3.3.14) and not Eq. (3.3.14) times G. Clearly, G_S has to be a decreasing function of G.

The destruction term R_F:

From the classical gas theory [79] we know that for dilute gases the collision rate among molecules can be approximated by:

$$\widetilde{\tau}^{-1} = \langle v \rangle \rho \sigma \tag{3.3.15}$$

where $\langle v \rangle$ refers to the mean speed of the gas, σ is the scattering cross section of the molecules, and ρ is the particle density.

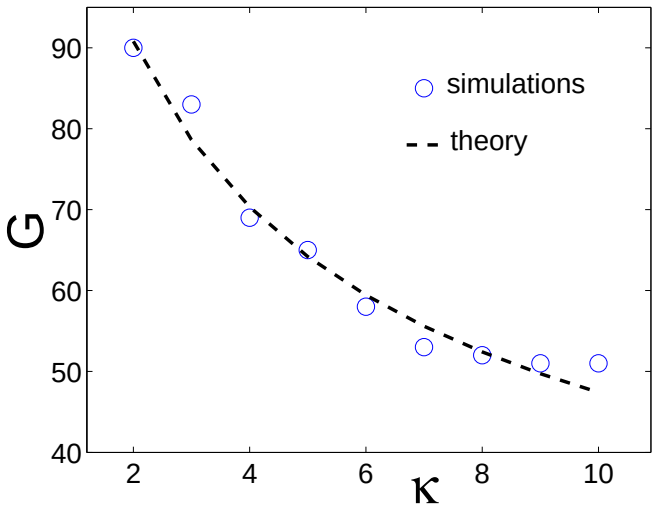

Figure 3.21: Average number of clusters G at the steady state vs. particle aspect ratio κ. Symbols corresponds to simulations performed with $N = 100$ and $\eta = 0.034$. The dot-dashed line is the approximation given by Eq. (3.3.18) with $\gamma = 0.1186$.

We make use of this expression to estimate the characteristic time between collisions of the clusters. We assume that clusters move roughly at the active speed $\tilde{v}$, and then replace $\langle v \rangle$ with $\tilde{v}$. In this case, ρ is simply $\rho = G/A$, where A is the area of the box where particles move. σ represents the scattering cross section of the clusters. For disks we know that the scattering cross section is proportional to the radius, which is proportional to the square root of the disk area. Therefore, σ has to be proportional to $\sqrt{q}$, and also to σ_0, the scattering cross section of individual particles, which we assume to be proportional to $L + W$ [3]. Thus, $\sigma = \sqrt{q}\,(L + W)$.

Then, the rate at which a cluster collides takes the form, $\tilde{v}\sqrt{N\,G}/A$. Since there are G clusters in the system, we approximate the mean number of clusters that disappear per unit time by:

$$R_F\,(G) = \frac{\tilde{v}\sqrt{N}}{A} G^{3/2}\,. \tag{3.3.16}$$

By inserting Eqs. (3.3.14) and (3.3.16) into Eq. (3.3.13), and using that $\kappa = L/W$ and $a = L.W$ to express $L = \sqrt{a\kappa}$ and $W = \sqrt{a/\kappa}$, we find the following explicit expression

[3] More details about the scattering cross section of individual particles is given in the next section.

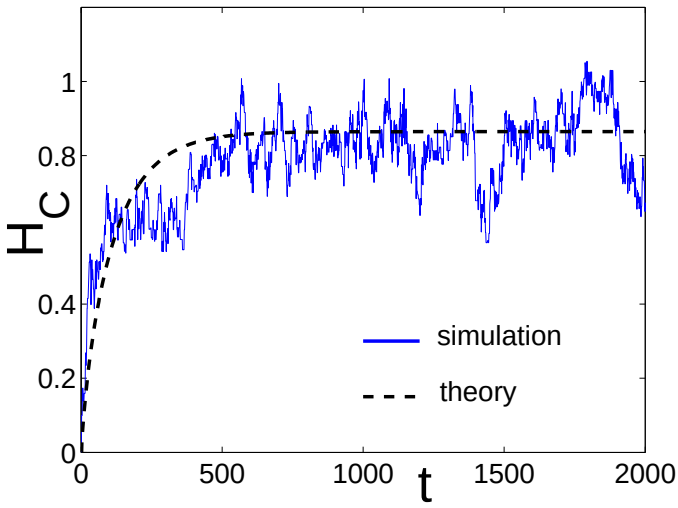

Figure 3.22: Average cluster entropy H_C vs. time. Symbols corresponds to simulations performed with $N = 100$, $\kappa = 4$ and $\eta = 0.034$. The dot-dashed line is the approximation given by inserting in Eq. (3.3.12) the numerical integration of Eq. (3.3.17) with $\gamma = 0.1186$ and $\beta = 6$.

for evolution equation for the number of clusters:

$$\dot{G} = \beta\tilde{v}\sqrt{N}\left[\frac{1}{\gamma\sqrt{a\kappa}}G^{-1/2} - \frac{\sqrt{a}}{A}\left(\kappa^{1/2} + \kappa^{-1/2}\right)G^{3/2}\right] . \tag{3.3.17}$$

where β is a constant that is introduced to adjust the time scale of the process. Thus, the steady state of G simply reads:

$$G = \sqrt{N}\left[\eta\gamma\right]^{-1/2}\left(1+\kappa\right)^{-1/2} , \tag{3.3.18}$$

where κ is defined as before, i.e., $\kappa = \rho a$.

Inserting Eq. (3.3.18) into Eq. (3.3.12) we obtain H_C as function of κ and η:

$$\begin{aligned} H_C(\kappa,\eta) &= \ln\left(\sqrt{N\eta\gamma\left(1+\kappa\right)} - 1\right) \\ &- \sqrt{N\eta\gamma\left(1+\kappa\right)}\ln\left(1 - \sqrt{N\eta\gamma\left(1+\kappa\right)}\right) \end{aligned} \tag{3.3.19}$$

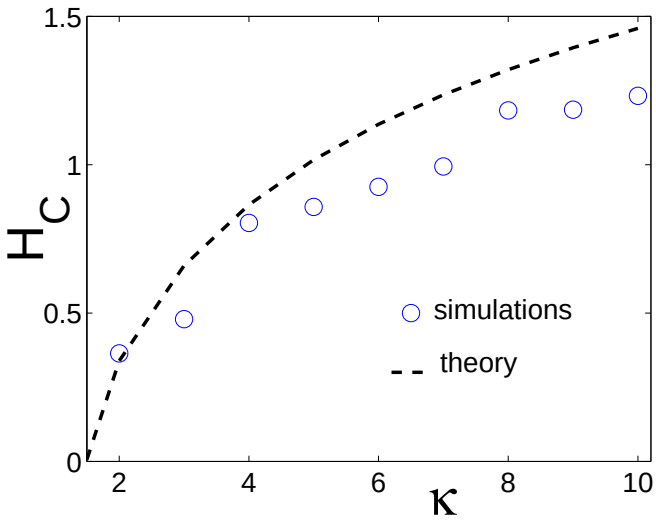

Figure 3.23: Average cluster entropy H_C at the steady state vs. particle aspect ratio κ at low density. Symbols corresponds to simulations performed with $N = 100$ and $\eta = 0.034$. The dot-dashed line is the approximation given by Eq. (3.3.19) with $\gamma = 0.1186$.

Comparing theory and simulations

Fig. 3.20 compares the time evolution of G predicted by Eq. (3.3.17) (dotted curve) and and $G(t)$ measured in an individual-based simulation performed with $N = 100$, $\kappa = 4$ and $\eta = 0.034$ (circles). For the numerical integration of Eq. (3.3.17) a value of $\gamma = 0.1186$ and $\beta = 6$ were used. γ is chosen to best fit the simulation data shown in Fig. 3.21, while β is used to adjust the time scale of Fig. 3.20. A fitting of the simulation data shown Fig. 3.21 by a function $C_1\,(1+\kappa)^{-C_2}$ reveals that C_2 has to be $1/2$. This implies that the dependency on G of the right hand of Eq. (3.3.17) is correct.

Fig. 3.22 shows the time evolution of the cluster entropy H_C corresponding to the simulation whose $G(t)$ is exhibited in Fig. 3.20. In simulations H_C is measured using the definition given by Eq. (3.3.8), i.e., $H_C(t) = -\sum_{i=1}^{N} n_i(t)/G(t) \ln\left(n_i(t)/G(t)\right)$ (blue solid line). Therefore, the values of H_C reported from simulation are calculated from the cluster size distribution. On the other hand, the black dashed line in Fig. 3.22 corresponds to Eq. (3.3.12), where q now is replaced by $q = N/G(t)$, $G(t)$ being the solution of Eq. (3.3.17). Thus, the theoretical approximation of H_C is performed only through the mean number of particles per cluster, which simply involves $G(t)$, and ignores the actual shape of cluster size distribution, which is assumed to obey Eq. (3.3.10).

Fig. 3.23 compares values of H_C for various values of κ measured in simulations, as mentioned above (circles), and calculated theoretically (dashed line). This time the theoretical approximation is performed by inserting in Eq. (3.3.12) the asymptotic values of G given by Eq. (3.3.18), with $\gamma = 0.1186$.

Eqs. (3.3.18) and (3.3.12) provide a phenomenological understanding of dynamics of the number of clusters and cluster entropy far below from the transition to clustering, but definitely they can not account for the transition itself and the clustering properties above it. The transition to clustering does not simply imply a decrease in the number of cluster, but also a dramatic change in the cluster size distribution. Particularly, the cluster size distribution becomes no longer monotonically decreasing above the transition point, as shown in Fig. 3.19. However, in the derivation of Eq. (3.3.12) we have assumed by Eq. (3.3.10) that the cluster size distribution is a monotonically decreasing function for all possible values of G. As a consequence, the cluster entropy H_C given by Eq. (3.3.19) is a monotonically increasing function of κ and η. But, as can be seen in Fig. 3.24, H_C is not a monotonically increasing function of κ (the same can be shown for η). Moreover, above the transition to clustering, reflected in Fig. 3.24 by the maximum exhibited by H_C[4], the cluster entropy becomes a monotonically decreasing function of κ.

To understand the transition to clustering and the clustering effects above the transition, we have to deal directly with the cluster size distribution. In next section we derive a theoretical description for the cluster size distribution.

3.3.4 A theoretical description for the cluster size distribution

The study of cluster size distributions in physical processes is not new. However, most of the effort has been focused to understand one particular non-equilibrium process: irreversible cluster coagulation of Brownian particles [82–89]. This kind of non-equilibrium kinetics is frequent in nature: coagulation of colloidal particles, coalescence of rain drops, smoke and dust, the formation of planetesimals from submicron dust grains, etc [82, 83]. Though this kinetics is remarkably important, it is not a general coagulation process. In particular, it is assumed that clusters cannot disintegrate, i.e., they cannot split into parts [82–85]. In consequence, clusters can only grow in time. A second important feature of these systems is that the number of particles can be considered infinite. Therefore,

[4]The transition to clustering is also manifested in the behavior of the cluster size distribution which exhibits a monotonically decreasing shape before the transition, while after it, the cluster size distribution becomes bimodal.

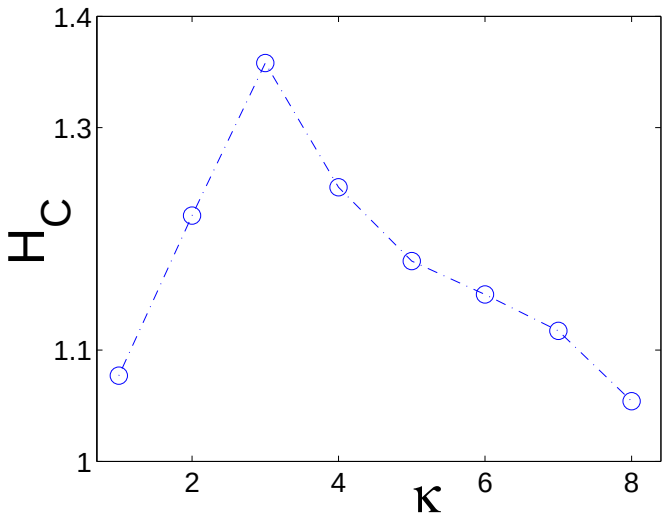

Figure 3.24: Cluster entropy H_C at the steady state vs. particle aspect ratio κ at high packing fraction. Simulations performed with $N = 50$ and $\eta = 0.34$. Notice that $H_C(\kappa)$ is not a monotonically increasing function exhibit κ and exhibit a maximum at $\kappa = 3$.

cluster sizes are not limited and particle conservation is not imposed. It becomes evident that we cannot make use of the classical coagulation theory to explain the cluster size dynamics of the self-propelled rods. While this is true, a brief introduction to the classical clustering theory might help to place in context the theoretical framework we develop in this section.

The celebrated cluster coagulation model introduced by Smoluchowski in 1916 [82, 83] assumes that each cluster of particles is surrounded by a sphere of influence. When their spheres of influence do not overlap, clusters execute independent Brownian motions. Whenever the sphere of influence of a pair of cluster touch, the clusters stick together and form a new cluster. To simplify the theoretical derivation of the model, it is assumed that: 1) clusters are randomly distributed in space and this feature persists throughout the coagulation process, 2) only collisions between pairs of clusters are significant, and 3) the number of new clusters of size $i+j$ formed per unit time and unit volume due to collisions of clusters of sizes i and j, is proportional to the product of the cluster concentrations $C_i = n_i/V$ and $C_j = n_j/V$, i.e., $K_{i,j}C_iC_j$, where n_i is the number of cluster of mass i as defined above, V is the volume of the coagulating system, and $K_{i,j}$ is the coagulation

kernel. The rate equation describing the evolution of $C_i(t)$ takes the form:

$$\begin{aligned} \dot{C}_i(t) &= \frac{1}{2}\sum_{j=1}^{i-1} K_{i-j,j} C_{i-j}(t) C_j(t) \\ &- \sum_{j=1}^{\infty} K_{i,j} C_i(t) C_j(t)\,,\ i = 1, ..., \infty, \end{aligned} \tag{3.3.20}$$

where the first term of the right hand side represents all binary collisions per unit time that lead to clusters of mass i, while the second term describes the number of clusters of mass i that grow in size, per unit time, due to collision with other clusters.

The natural continuous version of Eq. (3.3.20) leads directly to an evolution equation for the cluster size distribution $C(v,t)$, where v denotes physical cluster size. The evolution of $C(v,t)$ takes the form of an integro-differential equation:

$$\begin{aligned} \partial_t C(v,t) &= \frac{1}{2}\int_0^v K(u, v-u) C(u,t) C(v-u,t) du \\ &- C(v,t)\int_0^{\infty} K(u,v) C(u,t) du\,. \end{aligned} \tag{3.3.21}$$

When a solution of Eq. (3.3.21) exists, and whether it is unique are currently open problems. Existence and uniqueness of solution for all times have been proven for the kernels $K(u,v) \leq C(u+v)$, where C is a constant. This result has been recently extended to the kernels $K(u,v) \leq r(u)r(v)$, where $r(v) = O(v)$, as $v \to \infty$ [87, 88].

In the following we focus on the self-propelled rods system and derive a theoretical description for the cluster size distribution of this system.

Derivation of evolution equation for the cluster size distribution

We want to describe the evolution of the number n_j of clusters of a given size j through kinetic equations. The description has to account for fusion and fission of clusters, and conservation of the number of particles. For the fusion of clusters we adopt kinetic equations similar to the ones described above, while for cluster fission we define empirical terms derived from the typical behavior seen in simulations. The time-evolving cluster size distribution is given by the set of $\{n_j(t)\}_{j=1}^{\infty}$, where $n_j(t)$ is the number of clusters of mass j at time t.

This description neglects the geometry of clusters as well as spatial fluctuations. This allows us to consider a single rate constant for all possible collision processes between clusters of mass i and j, as well as a unique disintegration constant for any cluster of mass i. In addition we make four crucial assumptions:

i) The total number of particles in the system, $N = \sum_{j=1}^{N} j n_j\,(t)$, is conserved.

ii) Only binary cluster collisions are considered. Collisions between any two clusters are allowed whenever the sum of the cluster masses is less or equal to N.

iii) Clusters suffer spontaneous fission only by losing individual particles at the boundary one by one, *i. e.* a cluster can only decay by a process by which a j-cluster split into a single particle plus a $(j-1)$-cluster. This is motivated by observations in the above simulations.

iv) All clusters move at constant speed, $\widetilde{v} \approx F/\zeta_{\|}$, which implies that rods in a cluster have high orientational order and interact only very weakly with their neighbors.

Under all these assumptions the evolution of the n_j's is given by the following N equations:

$$\dot{n}_1 = 2B_2 n_2 + \sum_{k=3}^{N} B_k n_k - \sum_{k=1}^{N-1} A_{k,1} n_k n_1 \tag{3.3.22}$$

$$\dot{n}_j = B_{j+1} n_{j+1} - B_j n_j - \sum_{k=1}^{N-j} A_{k,j} n_k n_j + \frac{1}{2} \sum_{k=1}^{j-1} A_{k,j-k} n_k n_{j-k} \quad \text{for} \quad j = 2, ..., N-1 \tag{3.3.23}$$

$$\dot{n}_N = -B_N n_N + \frac{1}{2} \sum_{k=1}^{N-1} A_{k,N-k} n_k n_{N-k} \tag{3.3.24}$$

where the dot denotes time derivative, B_j represents the fission rate of a cluster of mass j, defined by $B_j = (\tilde{v}/R)\sqrt{j}$, and $A_{j,k}$ is the collision rate between clusters of mass j and k, defined by $A_{j,k} = (\tilde{v}\sigma_0/A)\left(\sqrt{j} + \sqrt{k}\right)$. σ_0 is the scattering cross section of a single rod. R is the only free parameter and indicates the characteristic length a rod at the boundary of a cluster moves before it is leaving the cluster in a typical fission event. We assume $R = \alpha L$ taken into account that longer rods will stay attached to cluster for a longer time. The dynamics of clusters of an intermediate size j is given by Eq. (3.3.23). Eqs. (3.3.22) and (3.3.24) differ from Eq. (3.3.23) because 1-particle clusters cannot decay and it can not be the product of a collision, while a N-particle cluster can not incorporate any extra

particle, i.e., it can not experience a collision. Since $\dot{N} = 0 = \sum_{j=1}^{N} j\dot{n}_j\,(t)$, conservation of particles is assured.

Let us provide more details about these equations, focusing particularly on Eq. (3.3.23). The number of clusters of mass j can grow due to the decay of clusters of mass $j+1$, first term in 3.3.23, or due to the collision of any two clusters whose masses add up j, last term in Eq. (3.3.23). A decrease of clusters of mass j may come from the spontaneous disintegration of j-clusters, second term in Eq. (3.3.23), as well as from the coalescence of clusters of mass j with any other cluster, third term in Eq. (3.3.23). So, gain and loss terms come from collision as well as disintegration processes.

The rate constants

The reasoning behind the rate constants B_k and $A_{k,j}$ is the following. Since we are assuming clusters are homogeneously distributed and moving at constant speed, we can derive $A_{k,j}$ by making use of the expression for collision rate of an ideal gas (see Eq. (3.3.15)). To adapt this expression to our problem, we assume $\langle v \rangle$ to be as before the active speed $\tilde{v}$. σ has to be replaced by the effective scattering cross section (*SCS*) between clusters of mass j and k. We approximate the *SCS* of a cluster of mass j in 2D by $\sqrt{j}\sigma_0$, where σ_0 is the *SCS* of a single particle (assuming that in clusters particles are aligned to each other). So, the effective *SCS* between clusters j and k becomes $\sigma = \sigma_0(\sqrt{j} + \sqrt{k})$ (explicitly using the fact that we are in 2D). ρ has to be substituted by n_j/A, where A is the system area. Finally $\omega_{j,k}$ represents the collision rate of a k-cluster against j-clusters. Thus, the total number of collisions per unit time between j- and k-clusters becomes $\omega_{j,k}n_k = \tilde{v}\sigma_0(\sqrt{j} + \sqrt{k})(n_j/A)n_k = A_{j,k}n_jn_k$, and from this expression we obtain $A_{j,k} = (\tilde{v}\sigma_0/A)\left(\sqrt{j} + \sqrt{k}\right)$.

For the rate of disintegration we assume a probability of loosing a particle proportional to the number of particles that conforms the edges of the cluster. For a i-cluster we approximate this number by $\sqrt{i}$. In addition we assume that there is a characteristic time which is associated to the time a particle lasts at the edge of the cluster. And as before, by the Buckingham π theorem [81], we know that this time has to be proportional to either $L/\tilde{v}$ or $W/\tilde{v}$, or a combination of both. Since elongated particles are more stable than short particles, we simply take this time to be $R/\tilde{v}$, where R is defined as $R \sim L = \sqrt{\alpha\kappa}$. All this together leads to a splitting rate for the i-cluster, $B_i = (\tilde{v}\sqrt{i}/(\alpha L)$.

We are interested in expressing Eqs. (3.3.22)-(3.3.24) as function of $\tilde{v}$, a, A and

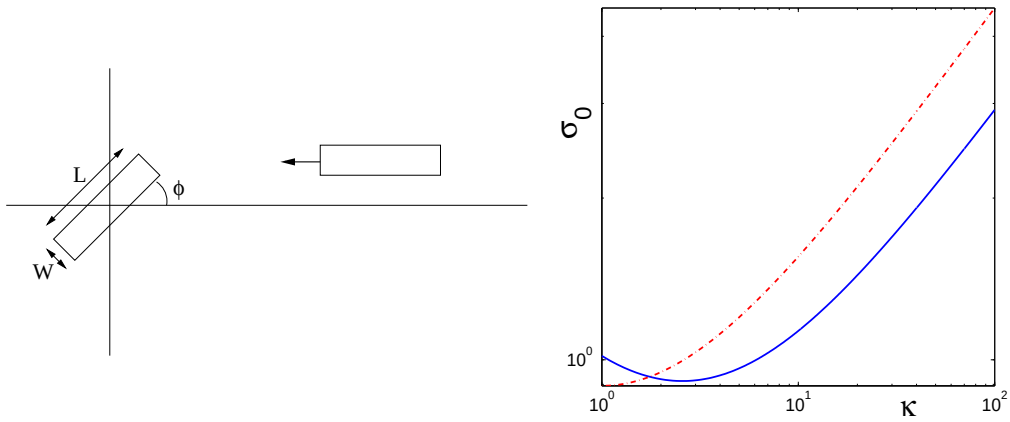

Figure 3.25: Left: The scheme illustrates the proposed experiment to measure the scattering cross section of individual particles (see text). The scattering cross section of the particles at the origin is a function of ϕ. Right: Effective scattering cross section σ_0 as function of the particle aspect ratio κ. The solid line corresponds to $\sigma = (2/\pi)\sqrt{a}\,(\sqrt{\kappa} + 1/\sqrt{\kappa}) + \sqrt{a/\kappa}$, while the dot-dashed line is the simplified approximation given by Eq. (3.3.25).

κ. There are two term we need to transform: L and σ_0. Recalling that $a = L\,W$ and $\kappa = L/W$, we express L as $L = \sqrt{a\,\kappa}$. For σ_0 we have first to remember the definition of *SCS*. Assume that we have one rod whose center of mass is fixed at the origin and that we shoot the rod with point-like particles from one place to the right of the origin and in such a way that the point-like particles move parallel to the x-axis (see left panel of Fig. 3.25). *SCS* is the effective "area" (in 2D, segment) that these particles can hit. The size of this segment depends on the orientation of the rod with respect to the x-axis, which is given by an angle that we call ϕ. As can be seen in the left panel of Fig. 3.25, the *SCS* for a given angle ϕ is $\sigma(\phi) = L\sin(\phi) + W\cos(\pi/2 - \phi)$. We want to know the effective *SCS* of a rod which can be oriented with equal probability in any direction. This quantity takes the form $\sigma = (2/\pi)\int_0^{\pi/2}\sigma(\phi)d\phi = (2/\pi)(L + W)$, where the integral runs from 0 to $\pi/2$ due to the symmetry of the problem and $2/\pi$ symbolizes that all directions are equally possible. Since in the system we do not have point-like particles but rods, the actual expression for σ reads $\sigma = (2/\pi)(L + W) + W$, assuming we shoot with rods whose long axis move parallel to the x-axis. However, we only need an estimation of a

single rod *SCS* to plug into the expression of $A_{j,k}$, and so we approximate σ_0 simply by:

$$\sigma_0 = \sqrt{a}\left(\sqrt{\kappa} + \frac{1}{\sqrt{\kappa}}\right), \tag{3.3.25}$$

where we have used that $L = \sqrt{a\,\kappa}$ and $W = \sqrt{a/\kappa}$. The right panel of 3.25 shows the scattering cross section of single rods as function of the aspect ration κ.

We have seen that Eqs. (3.3.22)-(3.3.24) are function of $\tilde{v}$, a, A and κ. Integrating them with the same parameters used in the simulation and initial condition $n_j\,(t=0) = N\delta_{1,j}$, we can compare the simulations and the explained rate equation approach (see Fig. 3.19). Next section is devoted to this issue.

Comparing theory and simulations

We want to compare the steady state of Eqs. (3.3.22)-(3.3.24) and the long time behavior of the simulations, which we assume to be also in their steady state. We make the comparison through the weighted cluster size distribution $p(m) = n_m^0 m/N$, where n_j^0 symbolizes $n_j(t)$ for $t \to \infty$. The best agreement between the theory and simulations for active particles is found for a choice of $\alpha = 1.0 \pm 0.05$ (see Fig. 3.19). Hence, we will use $R = L$ in the following.

To understand the relation between the parameters of the model and clustering effects, we rescale Eqs. (3.3.22)-(3.3.24) by introducing a new time variable: $\tau = t\tilde{v}/\sqrt{a\kappa}$. In the dimensionless model the equations read:

$$\begin{aligned}
\dot{n}_1 &= 2\sqrt{2}n_2 + \sum_{k=3}^{N}\sqrt{k}n_k - \sum_{k=1}^{N-1}\left(\sqrt{k}+1\right)n_k n_1 \\
\dot{n}_j &= \sqrt{j+1}n_{j+1} - \sqrt{j}n_j + P[\frac{1}{2}\sum_{k=1}^{j-1}\left(\sqrt{k}+\sqrt{j-k}\right)n_k n_{j-k} \\
&\quad - \sum_{k=1}^{N-j}\left(\sqrt{j}+\sqrt{k}\right)n_k n_j] \quad \text{for} \quad j = 2, ..., N-1 \\
\dot{n}_N &= -\sqrt{n}n_N + \frac{1}{2}\sum_{k=1}^{N-1}\left(\sqrt{k}+\sqrt{N-k}\right)n_k n_{N-k}
\end{aligned} \tag{3.3.26}$$

where P is the only dimensionless parameter and is defined as $P = (\kappa+1)a/A$. Notice that $\tilde{v} \neq 0$ is scaled and does not affect the qualitative dynamics of the system. In the

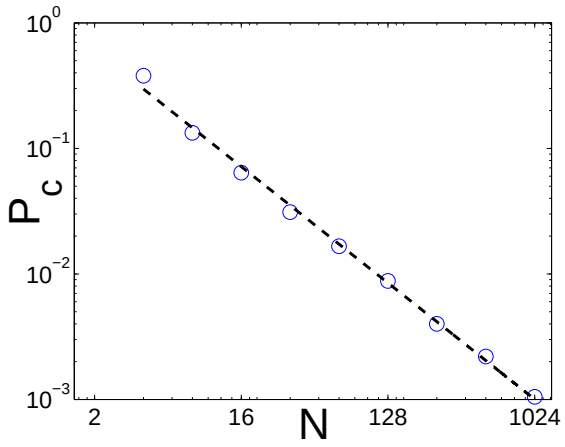

Figure 3.26: The dimensionless critical parameter P_c as function of the number of particles N. The slope of the dashed line is -1.026 ± 0.023.

dimensionless model the parameter P stands for the ratio between fusion and fission processes and therefore triggers the transition from a unimodal to a bimodal cluster size distribution (Fig. 3.19), as well as the crossover exhibited by M_T between a power-law and a log-tail (Fig. 3.28). Given the system area A, the rod area a, and the number of rods N, we can estimate κ_c by:

$$\kappa_c = P_c\,(N)\,\frac{A}{a} - 1 \tag{3.3.27}$$

where $P_c\,(N)$ is the critical value of P above which clustering set in. Since the transition occurs when the distribution is no longer monotonously decreasing, we can accurately determine the critical transition parameter P_c using a *bisection*-based method. Given an interval $[a, b]$ of the parameter P, assume that for $P = a$ the integration of Eq. (3.3.26) reveals an monotonically decreasing asymptotic distribution, while for $P = b$ the integration leads to bimodal distribution (specifically, a non-monotonically decreasing distribution). Now we set $P = (a + b)/2$ and perform the integration. If the resulting distribution is monotonically decreasing, we know that $P_c \in [(a + b)/2, b]$. Otherwise, $P_c \in [a, (a + b)/2]$. By repeating this process, we can reduce the interval containing P_c and determine with accuracy the value of P_c.

At this point it is worth noticing that κ_c also depends on N, i.e., the total number of particles in the system, and correspondingly, the number of ordinary differential equations appearing in Eq. (3.3.26). To have a complete understanding of the problem we need

to know the dependency of P_c with N. Fig. 3.26 shows P_c versus N, where P_c was obtained through the bisection-like method explained above. The slope of the dashed line is -1.026 ± 0.023. Assuming that P_c is strictly inversely proportional with N and making some easy algebra, we observe that κ_c is a function exclusively of the packing fraction regardless of the number of particles:

$$\kappa_c = \frac{C}{\eta} - 1 \tag{3.3.28}$$

where the estimated value of C was $C \sim 1.46$. Eq. (3.3.28) defines the κ-η phase diagram of the problem. Fig. 5.3 shows that the prediction given by Eq. (3.3.28) is in accordance with simulation results. For the range of parameters used in the individual-based simulations, we retrieve in the rate equation approach the unimodal shape of the weighted cluster size distribution for small values of κ and η, and the bimodal shape for large values of the two parameters. In Fig. 3.19 a comparison of the cluster size distribution obtained in simulations and from the rate equation approach is shown. For active particles, given a density of particles (equivalently, a packing fraction), Eq. (3.3.28) predicts the critical aspect ratio κ_c that triggers the transition to clustering. Eq. (3.3.28) can also be inverted to obtain for a given particle aspect ratio κ, the critical density/packing fraction η_c above which clustering set in. To account the fluctuations introduced in individual based simulations of Brownian-active particles, α, which for active particles takes the value $\alpha = 1$, has to be replaced by $0 \leq \alpha < 1$. The dashed line in Fig. 5.3 indicates that fluctuations shift the curve given by Eq. (3.3.28) upwards, i.e., κ_c becomes $\kappa_c = C/(\alpha\eta) - 1$.

As mentioned above, P_c defines the transition to clustering which is manifested by the emergence of a bimodal cluster size distribution, and also by a crossover in $M_T(\kappa)$ from a power-law to a log-tail. M_T is defined as the probability of observing the maximum cluster, i.e., a cluster of size N: $M_T = p(N, t \to \infty)$. This quantity, as shown in Fig. 3.28 for the dimensionless model, exhibits two regimes. To the left of P_c, M_T grows rapidly with P, and a power-law regime is observed. To the right of P_c, the growth of M_T dramatically slows down, and $M_T(P)$ exhibits a logarithmic regime. Though these two regimes are always present, for large values of η the power-law regime is observable in a very small range of κ, as shown in Fig. 3.29. It is instructive to compare Figs. 3.29 and 3.17. In Fig. 3.17 M, the mean maximum cluster size measured in simulations, experiences a fast growth for small values of κ and then it seems to saturate. On the other hand, in Figs. 3.29 we observe that M_T grows rapidly for small values κ and very slowly,

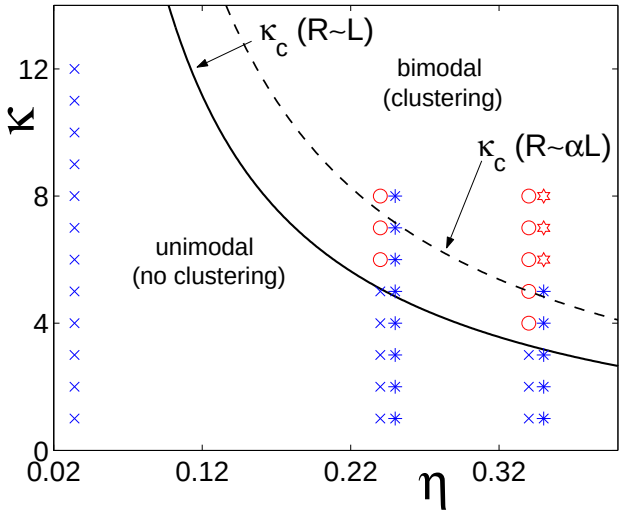

Figure 3.27: κ-η phase diagram. The solid line corresponds to the transition curve predicted by equation 3.3.28. The dashed line corresponds to the same kind of analysis but considering $R \sim \alpha L$, with $\alpha = 0.7$. The symbols indicate IBM simulations. ($crosses$) refer to unimodal, while ($circles$) to bimodal cluster size distribution of active particles. ($stars$) refer to unimodal, while ($hexagrams$) to bimodal of active-Brownian particles.

i.e., logarithmically, for large aspect ratios. These two regimes are also exposed by mean cluster size ϕ, as can be observed in Fig. 3.30. As shown in the inset of Fig. 3.28, the crossover between these two regimes coincides with maximum growth rate of M_T with P. This provides another interpretation for P_c, as the value of P at which M_T exhibits its maximum. Notice that slight deviations of P around this value are reflected as remarkable changes in the collective behavior of the rods.

Study of the cluster size distribution with system size

Eq. (3.3.28) suggests that κ_c depends only on η. On the other hand, η is the ratio between the area covered by particles and the system area. But, now the question is how the cluster size distribution scales with the system size. We understand by system size, number of particles, but keeping constant κ. This means that as we add more particles to the system, we also enlarge the size of the box in which particles move. From our analysis we can conclude that in principle the κ_c should be the same, but we cannot say anything else related to the distribution. The first problem we face is that by comparing distribution

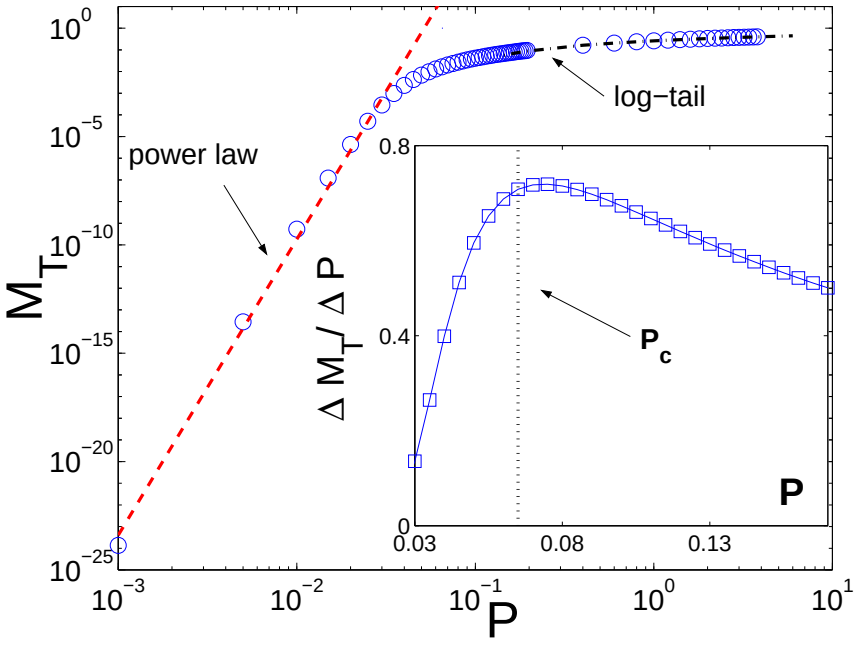

Figure 3.28: Crossover between the power-law and the log-tail regimes in the dimensionless model. The inset shows that P_c is located in the maximum growth rate of M_T with P.

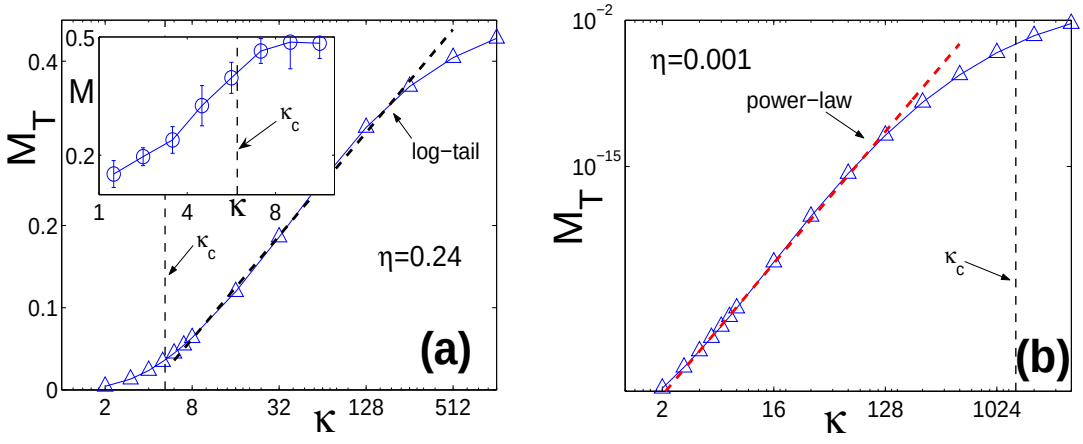

Figure 3.29: The two regimes of M_T as function of κ. (a) Semilog plot. The dashed line indicates the log-tail regime for $\kappa < \kappa_c$. The inset shows the mean maximum cluster size M vs κ for IBM simulations. (b) Log-log plot. The dashed line indicates the power-law regime for $\kappa > \kappa_c$.

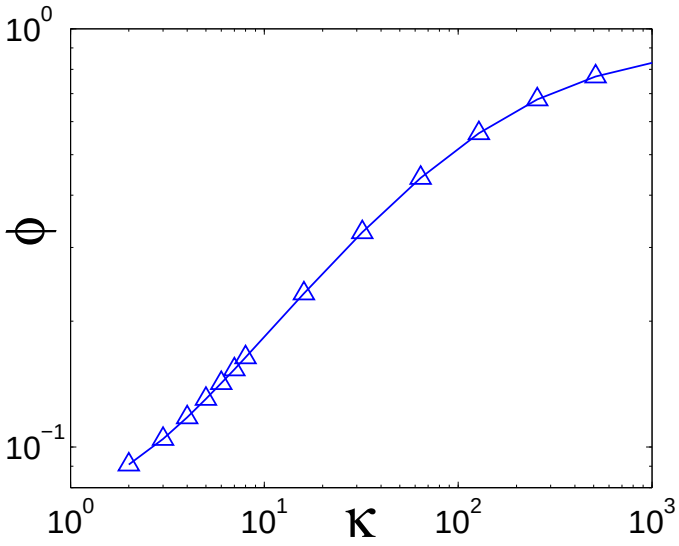

Figure 3.30: The mean cluster size ϕ for $\eta = 0.24$ and various values of the aspect ratio κ. Notice that ϕ also exhibits two regimes with η.

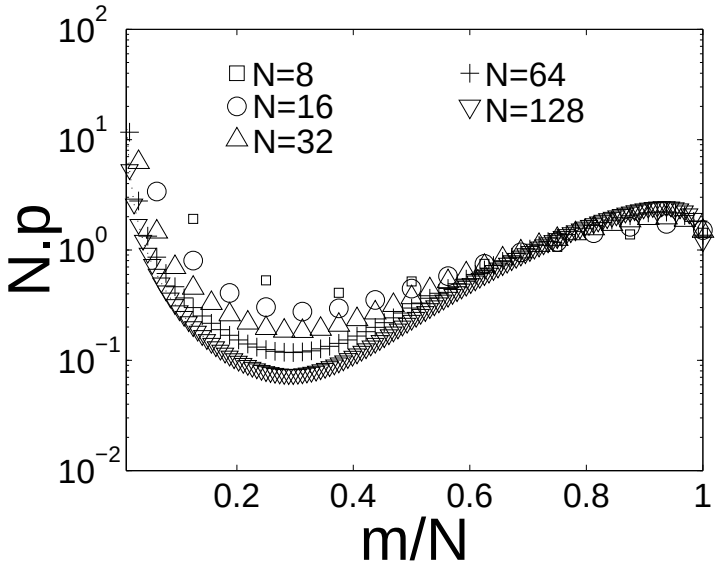

Figure 3.31: Scaling of the clustering effect as function of the system size.

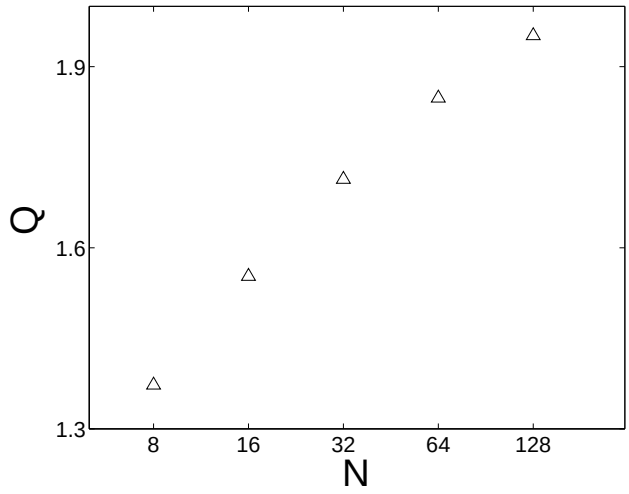

Figure 3.32: Fraction of particles living in clusters of mass bigger than half system size as function of the system size.

corresponding to different system sizes, the number of clusters in each system are different. We can overcome this difficulty by dividing the cluster index by N. If we do so, we fix this problem, but now we face another: The area under the curves are different. $\sum_{i=1}^{N} p_i \delta x = 1$ with $\delta x = 1$ for the case without "normalization" of the number of nodes. But now we get $\sum_{i=1}^{N} p_i \delta x/N = 1/N$. To solve this problem, we also renormalize the probability by multiply p_i by N. In Fig. 3.31 curves for $\eta = 0.24$, $\kappa = 12$ and various cluster sizes are shown.

Now we could ask whether the bimodal distribution is reinforced or weakened by the system size. If we observe directly the distribution we might get a wrong impression, because it seems that the clustering effects decrease with system size. However if we take a quantitative measure as Q, where we define Q as the ratio between the number of particles staying in clusters of mass $m > N/2$ and those staying in clusters of mass $m < N/2$, we realize that in larger system sizes clustering effect are stronger (see Fig. 3.32). To be more precise, from Fig. 3.32 we learn that the bigger the system size, the larger the fraction of particles living at large clusters.

In summary, this study suggests that the clustering effects discussed so far are also present in the thermodynamical limit.

3.4 Conclusions

Through individual-based simulations we have modeled a system of self-propelled particles in a noisy environment. Interactions between particles are based on the explicit consideration of particle shape, i.e., interactions depend on the overlapping area. The model exhibits a rich collective behavior that depends on the packing fraction η, noise amplitude, and particle aspect ratio κ.

We have found that elongated particles, i.e. with large aspect ratio κ, form densely packed clusters inside which particles are aligned and moving in the same direction. We have found multiple evidence of this process. At the level of the speed distribution, it has been noticed that large values of κ induce a shrinking of the width of the distribution around the active speed in such a way that the mode of the distribution shifts towards the active speed. The width of the angular velocity distribution, on the other hand, increases with κ, for lower values of the aspect ratio, and decreases at large values of it. This has been noticed by the shape of the average angular velocity and average square angular velocity, as function of κ, that exhibit a maximum at intermediate values of κ. The spatial arrangement of particles has been studied through the two-body correlation function that has revealed that particles locally arrange in a side-by-side and head-to-tail manner. A kind of spin-spin correlation function has been used to analyzed local orientation ordering. We have learned that polar local ordering is facilitated by κ. While isotropic particles do not exhibit local polar ordering, elongated particles succeed in forming densely packed cluster in which particles point in the same direction and consequently move coherently. Finally, through the study of the ferromagnetic and liquid crystal order parameter we have provided evidence that suggests that κ also induces global orientation ordering.

Interestingly, we have also found that these self-propelled rod-shaped particles, interacting only through short range repulsive interactions, exhibit non-equilibrium clustering for sufficient large values of η and κ. We have observed the active force F establishes a persistence in particle movement that makes active and active-Brownian particles qualitatively different to Brownian particles. The F induces particle clustering, while noise tend to destroy this effect. In the presence of reflecting boundary condition, particles cluster on the reflecting walls, while for periodic boundary conditions particles form polar-oriented clusters which swarm around.

The onset of clustering has been defined by a transition from an unimodal to bimodal cluster size distribution. This transition is reproduced by a mean-field description of the

cluster size distribution, which yielded a simple criterion, $\kappa = C/\eta - 1$, for the onset of clustering. This functional form with $C \approx 1.46$ provides a good fit to the results of the active particles simulations. The high density inside the cluster leads also to alignment of rods and coordinated motion of all particles in the cluster. It has been shown that the transition to clustering, as defined here, is practically independent of the system size, resp. the number of particles, and that clustering effects get stronger at large system sizes. We have provided evidence that suggests that all these findings hold in the thermodynamical limit. In addition, we have shown that the transition is also reflected in the crossover of the probability of the maximum cluster size, M_T, between a power-law and a logarithmic tail. The analysis of M_T has revealed that κ_c is located at the maximum growth rate of M_T with κ. Interestingly, the transition to clustering is also defined as the point, e.g., κ, at which cluster entropy H_C takes its maximum value. We have also shown that far below the transition, the clustering properties of the system obey the maximum entropy principle applied to H_C, which allowed us to describe the system in terms of the total number of clusters G.

It is instructive to compare our result for κ_c rewritten in the form $\kappa\eta + \eta \approx 1.46$ with the formula for the isotropic-nematic transition $\kappa\eta = 3\pi/2 \approx 4.7$ found in the two-dimensional version [90] of Onsager's mean-field theory for Brownian rods [71]. This shows that actively moving rods can achieve alignment at much lower densities than Brownian rods resp. particles in equilibrium systems. The clustering phenomenon is absent in simulations with isotropic self-propelled particles as well as with Brownian rods.

The model introduced in this chapter provides also an alternative explanation for collective behavior of rod-shaped objects. Previous swarming models have achieved swarming of particle, i.e., aggregation, clustering and local polarization of particles, by assuming attractive interaction plus some local alignment rule [40, 41, 46]. Here we have shown that volume exclusion interactions and the rod shape of particles suffice to produce swarm formation. The former observation offers a simple physical explanation for the formation of swarms and aggregates in many gliding rod-shaped bacteria, that often precedes the formation of biofilms and the appearance of more complex patterns. Our findings suggest that control of κ and η regulates collective behavior of bacteria. This is relevant for the following phenomena in myxobacteria: i) the different evolving colony shapes associated with different strains exhibiting different vegetative cell shapes (H. Reichenbach in [47]), ii) the diversity of the collective movement observed during fruiting body forma-

tion which is accompanied by changes of the cell shape as during sporulation (D. White in [47]), iii) the rapid growth and subsequent saturation of the 'swarm' expansion rate with initial density, iv) the dramatic increase in local cell density experienced by active moving bacteria during fruiting body morphogenesis in which geometry of cell arrangement allows maximum cell packing (D. Kaiser and L. Kroos in [47]), and v) the appearance of aggregates in areas of prior high cell density (D. White in [47]). However, real biological systems usually employ more complicated mechanisms like chemical signals and adhesion to achieve and enhance cell aggregation and swarming. The model studied here should be considered as a minimal model for collective phenomena of actively moving assemblies.

Finally, the current study can be thought as an example of short-range, contact based, interaction mechanism of self-propelled particles, in which arrangements of dipole forces give rise to a complex dynamics through the interplay of mechanical stress and reorientation of the dipoles [91, 92]. From this point of view, the applicability of these results ranges from gliding cells [93] to active films [94, 95].

Chapter 4

Collective motion in a simple model of polar particles with apolar interactions

Introduction

In Chapter 3 we have learned that self-propelled rods interacting by volume exclusion can exhibit collective effects like clustering and swarming for large enough values of particle density and particle aspect ratio. Remarkably, the interaction among these particles does not imply a local polar alignment of the particles. Fig. 4.1 sketches two typical collision events that lead to different local orientation of the particles. As illustrated by the figure, collisions among self-propelled rods can result in parallel as well as antiparallel alignment of the particles. This challenges the idea that coherent collective migration of self-propelled particle in absence of long-range signals and external forces is achieved only by polar alignment rules.

In this chapter a clear distinction is made between two basic alignment mechanisms: (1) the *ferromagnetic* (F) alignment by which particles tend to move parallel to each others, and (2) the *liquid crystal* (LC) alignment, by which particles tend to move parallel as well as antiparallel to each others (see Fig. 4.2). The F-alignment, introduced in the context of SPPs by Vicsek *et al.* [34] and studied by many others [40–43,96], may explain the collective motion observed in some biological examples with strong hydrodynamical interactions as fish schools [26], swimming bacteria [97], or chemotactic microorganisms [98,99]. On the other hand, the LC-alignment, as said above, is present when volume exclusion is the main interaction among agents, or when it is unlikely to consider U-turn

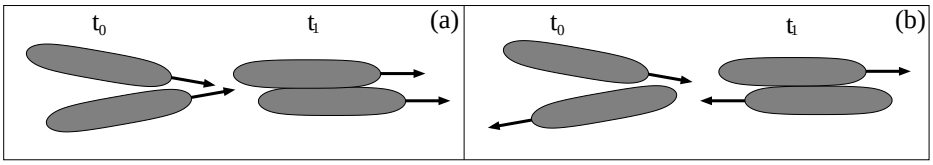

Figure 4.1: An example of LC alignment mechanism: collisions of anisotropic SPPs can lead to parallel (a) or antiparallel (b) alignment of the particles. The arrows indicate the active velocity of the particles. t_0 and t_1 refer to the configuration before and after the collision, respectively. See [100].

maneuvers. For instance, gliding bacteria, e.g., myxobacteria in the early stages of the life cycle [27, 28] as well as actin and tubulin filaments [29, 30] are good examples of SPPs with LC-alignment. Despite the importance of this kind of alignment, LC has received comparatively much less attention than F-alignment. Only recently Ramaswamy *et al.* proposed an hydrodynamical description of driven particles with LC-alignment [31]. In their study they assumed to be in the nematic phase and reported that their system exhibits giant fluctuations [31]. These findings were confirmed by Chaté *et al.* [48] through extensive simulations of a system of shaken particles with LC-alignment, and in experiments with driven granular media [50]. It was also shown that a discrete model of lattice-gas particles coupled to an angle field and exhibiting a liquid crystal angular dynamics is, in the nematic phase, intrinsically phase separated [49].

In this chapter, we introduce and analyze a simple model for self-propelled particles with persistent motion and a LC-alignment mechanism, by which particles align their direction of motion to the average local director. The model can be thought as an abstraction of the self-propelled rods model presented in Chapter 3, where the effects of volume exclusion interaction are now reduced to a local alignment rule. It has to be pointed out that particles are truly self-propelled, hence polar, and not like in [48–50], driven by shaking the system. Through extensive simulations we provide evidence that shows that at high density the system exhibits a continuous transition to orientational order. Interestingly, at high density ordering sets in before clustering. The homogeneous density scenario at which orientational order emerges at high density will allow us to propose in Chapter 5 an effective mean-field equation to describe the orientational dynamics. For the contrary, at low density the onset of orientation ordering and clustering starts at the same critical orientational noise. We show that orientational order at low density emerges from the interplay between orientational and clustering dynamics. Furthermore, we provide evidence

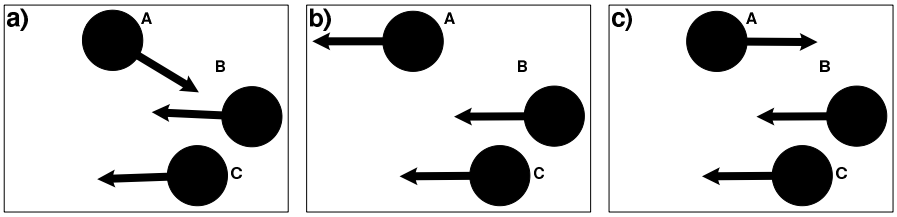

Figure 4.2: The scheme illustrates F- and LC-alignment mechanism. Suppose the initial configuration is given by (a). The F-alignment forces neighboring particles to move in the same direction as shown in (b). On the other hand, if LC-alignment is implemented, particles also align their velocity vector but in such a way that it is allowed for them to migrate in the same direction as well as in the opposite direction, as depicted in (c). Notice that F-alignment causes particle A to perform a long turn, almost a U-turn (see (a) to (b)), while LC-alignment implies a remarkable smaller turn (see (a) to (c)).

that suggests that the transition to ordering is in this case discontinuous. Simulation evidence indicates that the character of the transition to ordering is highly dependent on particle density, and being for higher densities mean-field type transition. In addition, we show that also diffusive particles at high density can exhibit a second order phase transition. However, orientational ordering in diffusive particles at low density is absent and no density inhomogeneities or clustering effects can be expected. These findings indicate that the phase transition occurs rather due to mixing of particles than exclusively to the directed active motion.

4.1 The individual-based model

We consider point-like particles moving at constant speed on a two dimensional space with periodic boundary conditions. The state of a particle at time t is given by its position $\mathbf{x}_i$ and its direction of motion θ_i. As in Vicsek's original model [34], a fast local relaxation of the direction of motion dynamics is assumed. The evolution of the i-th particle is described by the following updating rule:

$$\mathbf{x}_i^{t+\Delta t} = \mathbf{x}_i^t + v_0 \mathbf{v}\left(\theta_i^t\right) \Delta t \tag{4.1.1}$$

$$\theta_i^{t+\Delta t} = \arg\left(\sum_{|\mathbf{x}_i^t - \mathbf{x}_j^t| \leq \epsilon} \mathbf{f}\left(\mathbf{v}(\theta_j^t), \mathbf{v}(\theta_i^t)\right) \right) + \eta_i^t \tag{4.1.2}$$

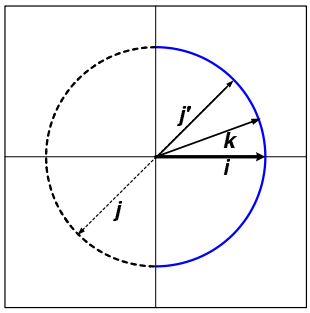

Figure 4.3: The scheme illustrates the mapping performed by the function $\mathbf{f}\left(\mathbf{v}(\theta_k^t), \mathbf{v}(\theta_i^t)\right)$. In the example, $\mathbf{f}$ projects j on the solid semicircle by making a 180-degree turn, i.e., j', while leaves unchanged k. See text.

where v_0 is the constant speed of the particles, $\mathbf{v}(\theta_i)$ is defined as $\mathbf{v}(\theta_i) = (\cos(\theta_i), \sin(\theta_i))$, Δt represents the temporal integration step, the sum in Eq. (4.1.2) runs also over i, $\arg(\mathbf{b})$ indicates the angle of the vector $\mathbf{b}$ in polar coordinates, η_i^t is a delta-correlated white noise with a strength η ($\eta_i^t \epsilon \left[-\frac{\eta}{2}, \frac{\eta}{2}\right]$), and $\mathbf{f}(\mathbf{a}, \mathbf{b})$ represents:

$$\mathbf{f}(\mathbf{a}, \mathbf{b}) = \begin{cases} \mathbf{a} & \text{if} \quad \mathbf{a}.\mathbf{b} \geq 0 \\ -\mathbf{a} & \text{if} \quad \mathbf{a}.\mathbf{b} < 0 \end{cases} \tag{4.1.3}$$

The reasoning behind the function $\mathbf{f}$ is as follows. We want particle i to align its direction of motion to the local average director. Instead of performing a normal velocity average as in [34], the ith particle calculates a weighted velocity average by mapping all its neighboring velocities (including its own) to a semicircle whose zenith is given by $\mathbf{v}(\theta_i^t)$. The procedure is illustrated in Fig. 4.3. Notice that due to this particular average, particles never turn more than 90 degrees to the left or to the right in one time step. Particles always perform the minimum turn to align their velocity direction to the local director, and so the movement is always smooth. In the limiting case of $v_0 = 0$, the model becomes an analog to the model studied in [101].

4.1.1 Parameters and boundary conditions

Simulations were carried out in a 2D box of area $L \times L$ with periodic boundary conditions and a random initial configuration. Given a system size L, and a radius of interaction ϵ, there are two parameters which determine the system behavior: particle density $\rho = N/L^2$, where N is the number of particles, and the directional noise strength η. Fig. 4.4

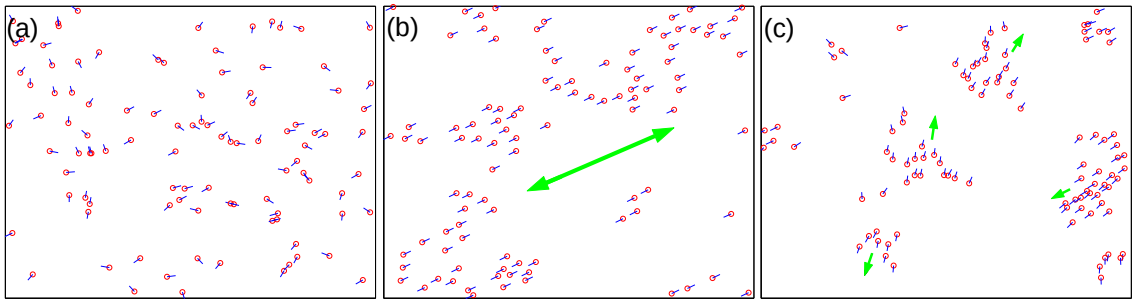

Figure 4.4: Snapshots of simulations. Number of particles, $N = 100$, system size $L = 30$, and radius of interaction $\epsilon = 1$. (a) random initial condition. After some time, for a noise strength $\eta = 0$, the system evolves towards the velocity orientational order state (b). The double arrow depicts the global director. For finite noise, (c) $\eta = 0.2$, particles form groups moving coherently in random direction. The arrows indicate the direction of motion of some clusters.

illustrates the dynamics of the system at low and high values of the noise strength η. The figure shows snapshots of simulations performed with $N = 100$ particles of interaction radius $\epsilon = 1$ in a box of linear size $L = 30$. When the noise intensity η is small enough, the system evolves towards a state with orientational order, see Fig. 4.4(b). On the other hand, for large values of η the system remains disordered, while at intermediate values of η a weak ordering is observed in which particles form groups that move in random direction as shown in Fig. 4.4(c).

All simulations have been performed with $\Delta t = 0.1$, $v_0 = 0.25$ and $\epsilon = 1$. Five densities have been studied: $\rho = 0.25$, 0.5, 1, 2 and 4. In each case, system sizes range from $N = 2^8$ to $N = 2^{14}$ particles. Typically simulations have been run for $\sim 10^6$ integration steps.

4.1.2 Order parameters

Orientational order

The modulus of the normalized total momentum distinguishes whether there is a favored direction in the system and takes the form:

$$S^F(t) = \left[\left(\frac{1}{N} \sum_{k=1}^{N} \cos(\theta_k^t) \right)^2 + \left(\frac{1}{N} \sum_{k=1}^{N} \sin(\theta_k^t) \right)^2 \right]^{1/2} . \tag{4.1.4}$$

Notice that using complex notation Eq. (4.1.4) can be expressed as $S^F(t) = \left|\frac{1}{N}\sum_{k=1}^{N} e^{i\theta_k^t}\right|$. We are interested in the temporal average of this quantity after the initial transient which simply reads:

$$S^F = \frac{1}{T - t_t}\sum_{i=t_t}^{T} S^F(i)\,, \tag{4.1.5}$$

where T refers to the simulation time and t_t to the transient time before the steady state is reached. $S^F = 1$ indicates that all particles point in the same direction. $S^F = 0$ might refer to a completely disordered situation, but also it might correspond to some peculiar ordered states as explained below.

The presence of a liquid-crystal alignment, as the one described by Eq. (4.1.2), makes possible the emergence of two favored direction in the system which are opposite to each other. If half of the particles move in one direction and the other half in the opposite direction, S^F vanishes. A different order parameter has to be used to distinguish this ordered state. We recall the order matrix Q of liquid crystals [72]. Specializing this for 2D and taking the largest eigenvalue, we obtain the following scalar orientational order parameter[1]:

$$S^{LC}(t) = \frac{1}{4} + \frac{3}{2}\sqrt{\frac{1}{4} - \frac{1}{N^2}\left\{\sum_{i,j}^{N} v_{xi}^2 v_{yj}^2 - v_{xi}v_{yi}v_{xj}v_{yj}\right\}} \tag{4.1.6}$$

where v_{xi} and v_{yi} are defined as $v_{xi} = \cos(\theta_i^t)$ and $v_{yi} = \sin(\theta_i^t)$. As before, we are interested in the temporal average:

$$S^{LC} = \frac{1}{T - t_t}\sum_{i=t_t}^{T} S^{LC}(i)\,. \tag{4.1.7}$$

S^{LC} takes the value 1 when all particles are perfectly moving along the same director, and $1/4$ in the disorder phase, where particles move with equal probability in any direction. It is worth noticing that $S^F = 1$ implies $S^{LC} = 1$, conversely $S^{LC} = 1$ does not necessary imply $S^F = 1$. The nematic phase is defined by $S^{LC} = 1$ while simultaneously $S^F = 0$. Notice that S^{LC} can be normalized to go from 0 to 1:

$$S_n^{LC} = \frac{4\left(S^{LC} - 1/4\right)}{3}\,. \tag{4.1.8}$$

[1]For the detailed derivation see Appendix B.

Using complex notation S_n^{LC} can be expressed as $S_n^{LC} = \left| \frac{1}{N} \sum_{k=1}^{N} e^{i2\theta_k} \right|$, where we have assumed θ_k to represent a stationary distribution of angles.

Interestingly, for equilibrium two-dimensional systems with continuum symmetry, i.e., for $v_0 = 0$, as stated by the Mermin-Wagner theorem [33], and confirmed by simulations, long-range orientational order cannot emerge. When $v_0 > 0$ the situation is different, the system becomes non-equilibrium, and orientational order can emerge. Vicsek *et al.* propose that the kinetic transition exhibited by these non-equilibrium systems is of second-order [34, 102]. It has been suggested that the transition for $v_0 \to \infty$ could be described by a network model which, for additive noise, also predicts a second-order transition [103]. In contrast, Chaté *et al.* provided evidence that shows that in the thermodynamical limit the transition may be discontinuous [40, 41], and that there is a critical system size above which a crossover from an apparent second to first order character of the transition can be observed.

Clustering

On the other hand, clustering is characterized through the weighted cluster size distribution $p(m)$. $p(m)$ is the probability of finding a randomly chosen particle belonging to a cluster of m particles and can be expressed as $p(m) = m \langle n_m \rangle / N$ where $\langle n_m \rangle$ represents the temporal-average number of cluster of mass m. We consider that two particles are $connected$ and belonging to the same cluster when their centers of mass are separated by a distance smaller or equal to the diameter of the interacting neighborhood.

4.2 Orientational order and clustering at high and low densities

Simulations at high and low density exhibit remarkable differences which are manifested in the character of transition from orientational disorder to order, including a different response of S^F and S^{LC} to changes in the noise intensity η, and the onset of clustering effects. In this section, a systematic comparison between these two scenarios, i.e., high and low density, is presented.

Fig. 4.5(a) shows the behavior of the orientational order parameters S^F and S^{LC} vs. the noise amplitude η for a high density density scenario corresponding to $\rho = 4$. Simulations were performed with $N = 2^{12}$ particles. A transition from a disordered (isotropic) to

an orientational ordered ("nematic") state is indicated. Notice that in contrast to classical liquid-crystal, for low values of η, S^F does not vanish. It will be explained below that this behavior is observed even for larger system sizes.

The vertical dot-dashed line in Fig. 4.5(a) indicates the onset of density instabilities. To the right of that line particle distribution is roughly homogeneous in space for all times. Fig. 4.5(b) illustrates this situation by showing a typical particle configuration slightly to the right from the vertical line. The simulation snapshot corresponds to the $2.5\,10^5$ integration step after the beginning of the numerical experiment whose value η is indicated in Fig. 4.5(a). To the left of the vertical line density instabilities becomes evident. Figs. 4.5(c) and (d) show typical patterns at the onset of the density instability, (c), and slightly to the left from it, (d). Both snapshots correspond to the $2.5\,10^5$ integration step. The corresponding values of η are shown in Fig. 4.5(a). Notice that the polar order parameter S^F does not take off simultaneously with S_n^{LC} but surprisingly after it, at the same point where the density instabilities become noticeable. Below it will be shown that this phenomenon is not a finite size effect. Moreover, it will be shown that S^F increases with system size making the effect even more pronounced. The gathered evidence suggests that density instabilities are mainly due to the coupling between local polar order and local density (i.e., formation of polar clusters) rather than to the interplay between local apolar order and local density as known to occur in liquid crystals [72] and driven apolar particles [31, 49, 50].

As said above, at low density the scenario at which orientation order emerges is significantly different. Fig. 4.6(a) shows, in first place, that for $\rho = 0.25$ and $N = 2^{14}$ particles, the transition to orientational order characterized by S_n^{LC} is much smoother than at high density. Secondly, it is observed that S_n^{LC} and S^F, in contrast to the high density case, take off simultaneously. Moreover, both order parameters adopt roughly the same values near the the onset of orientational ordering. This suggests that it is the emergence of polar order what set in at very first place. As said above, an increase S^F results always in an increase of S_n^{LC} (recall the opposite is not true). Notice, however, that as η is decreased to low values, apolar order becomes dominant. As mentioned above, the onset of density instabilities at high density seems to be caused by the coupling between local polar order and local density. Findings at low density supports this hypothesis since the onset of orientational ordering, resp. onset of polar order, is accompanied by the onset of clustering. Fig. 4.6(b) shows that before orientational order set in, the spatial distribution of particle is roughly homogeneous. The snapshot corresponds to the $2.5\,10^5$ integration step and

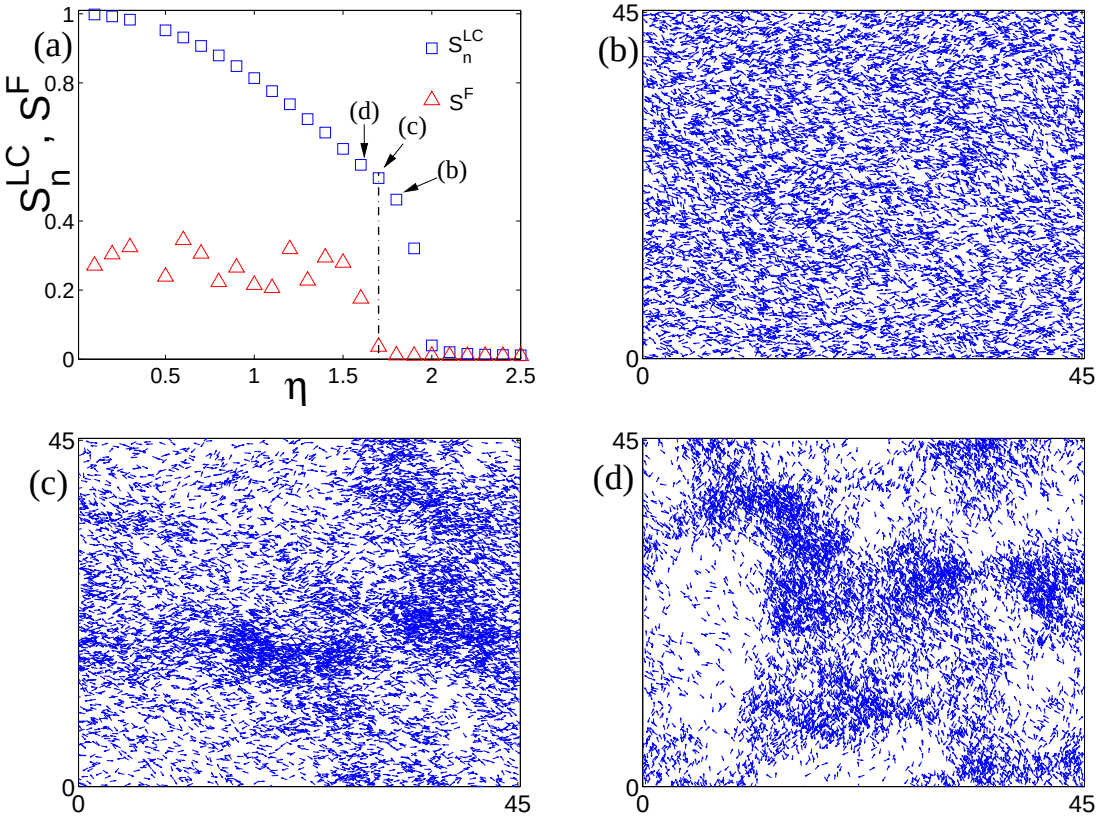

Figure 4.5: Orientational dynamics and clustering at high density. Number of particles $N = 2^{12}$ and density $\rho = 4$. (a) orientation order parameter S vs. noise amplitude η. Symbols are average over 10 realizations. (b)-(c) snapshots of the simulations for the values of η indicated in (a) at the steady state, time step $2.5\ 10^5$. Particles are represented just by arrows which indicate the direction of motion of the particle.

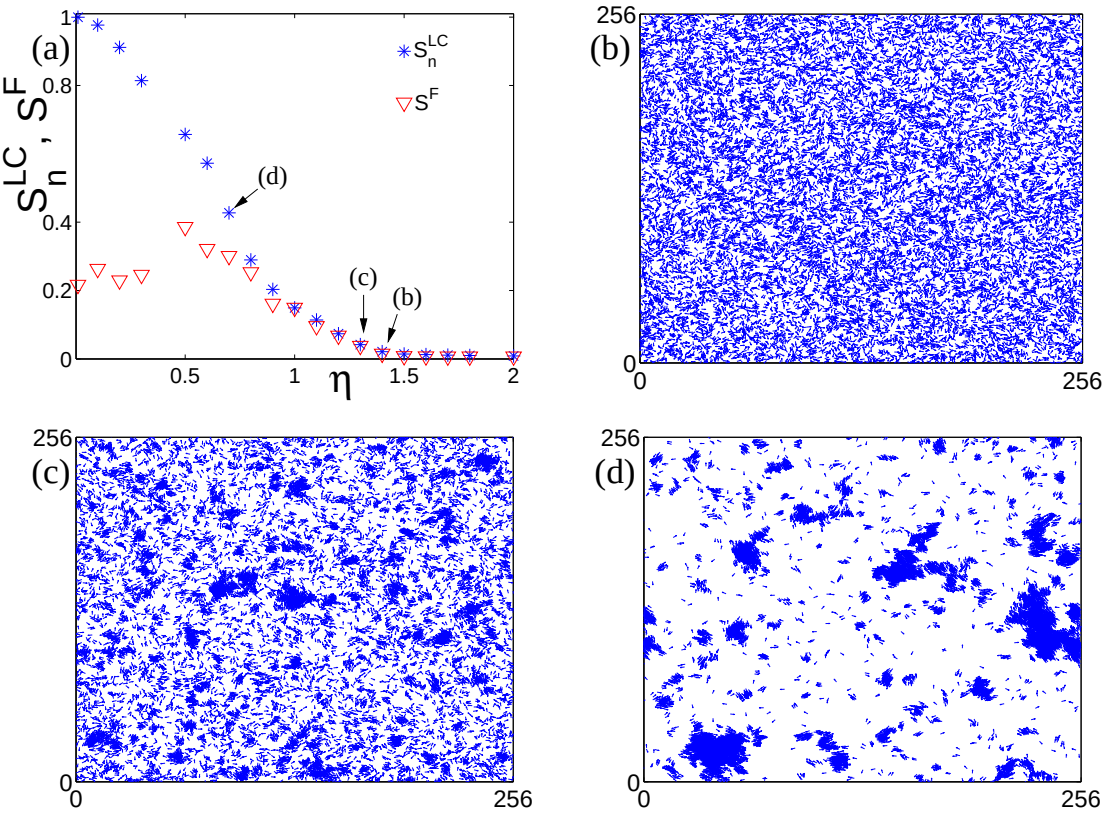

Figure 4.6: Orientational dynamics and clustering at low density. Number of particles $N = 2^{12}$ and density $\rho = 0.25$. (a) orientational order parameter S vs. directional noise amplitude η. Symbols are average over 10 realizations. (b)-(c) snapshots of the simulations for the values of η indicated in (a) at the steady state, time step $2.5\ 10^5$.

the value of η is indicated in Fig. 4.6(a) (equivalently for Fig. 4.6(c) and (d)). Just when orientational order emerges, as shown in Fig. 4.6(c), clustering effects become evident. As the noise is decreased, and S^F becomes larger, clustering effects are more pronounced, Fig. 4.6(d). We stress that these patterns correspond to typical particle configurations in the "steady state" of the systems. Clusters do not keep on growing as in a phase separation process. As it will be shown below, clusters are formed and disintegrated in a dynamical way. The rate of growth and disintegration of the clusters is highly dependent on the value of η. Given a value of η the cluster size distribution reaches after a transient a steady distribution. At low density, the orientational dynamics is highly coupled to the clustering dynamics.

4.2.1 System size study

We are interested in knowing whether the above mentioned phenomena persist in the thermodynamical limit or are just a finite size effect. We start out by questioning whether there is genuine long-range order. The Mermin-Wagner theorem states that two-dimensional systems with continuum symmetry cannot exhibit true long-range order [33]. Furthermore, Koterlitz and Thouless showed how in the planar XY-model the order parameter, i.e., the magnetization, decays with the system size [104, 105]. As verified later on in simulations [106], the order parameter ϕ of the model scales with the system size N as $\langle\phi\rangle \sim N^{-\psi(T)}$, where T refers to the temperature in the system and ϕ a function of the temperature. This implies that for all finite temperature T, in the thermodynamical limit, i.e., $N \to \infty$ the order parameter ϕ vanishes. The same kind of scaling was observed in equilibrium simulations of two-dimensional long, thin, hard spherocylinders [107] and in a non-equilibrium two-dimensional system of driven apolar particles interacting by a LC-alignment [48]. If our system does not exhibit a genuine long-range order, then we expect it to present quasi-long-range order as in a Kosterlitz-Thouless transition. We test whether the parameter scales S^{LC} as $S^{LC} \sim N^{-\psi(\eta)}$. Fig. 4.7 shows $S^{LC}(\eta, N)$ as function of the system size N for various values of the noise intensity η. Simulations were performed at high density, $\rho = 2$. According to the Kosterlitz-Thouless scaling, for a given η, S^{LC} obeys a particular decreasing power-law of base N whose exponent depends on η. The different curves in Fig. 4.7(a) correspond to different values of η. Figs. 4.7(a) and (b) are in log-log scale. Since straight lines are not observed, particularly evident for large values of η, we conclude $S^{LC}(\eta, N)$ does not scale as predicted by the Kosterlitz-Thouless, and consequently we discard quasi-long-range order at high density. Simulations at low density, as it will discuss below, are much more noisy and it was not possible to draw any conclusion regarding the scaling of $S^{LC}(\eta, N)$.

In the following we explore the behavior of S_n^{LC} and S^F, and their interplay, with the system size N. Fig. 4.8(a) shows S_n^{LC} and S^F measured in simulations performed with $N = 1024$ and $N = 16384$ particles at a density $\rho = 0.25$. For both system sizes the curves for S_n^{LC} and S^F take off simultaneously and grow together up to roughly the same value of η, regardless of the system size. As expected, the value S_n^{LC} increases for smaller system sizes. While S^F follows the curve of S_n^{LC}, the same behavior in S^F is observed. The numerical evidence supports the hypothesis that at low density the onset of orientational order is due to the onset of polar order.

The situation at high density is remarkably different. Fig. 4.8(b) shows S_n^{LC} and

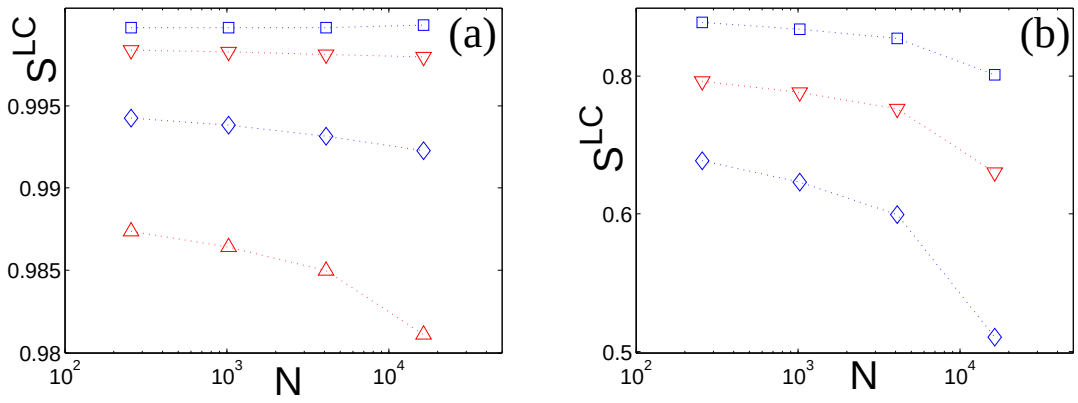

Figure 4.7: S^{LC} order parameter vs. system size N for various values of the noise intensity η. Particle density $\rho = 2$. (a) $\eta = 0.001$ (squares), 0.01 (upside-down triangles), 0.1 (diamonds) and 0.3 (triangles). (b) $\eta = 1.0$ (squares), 1.3 (upside-down triangles) and 1.6 (diamonds). (a) and (b) are in log-log scale. Notice that $S^{LC}(\eta, N)$ does not scale as $S^{LC}(\eta, N) \sim N^{\zeta(\eta)}$ as expected in a Kosterlitz-Thouless transition.

S^F measured in simulations performed with $N = 1024$, $N = 4096$ and $N = 16384$ particles at a density $\rho = 2.0$. As expected, the value S_n^{LC} increases for smaller system sizes. Surprisingly, S^F exhibits the opposite behavior. S^F increases with system size. The transition from a disordered to an apparent nematic state suggested by S_n^{LC} comes accompanied by a strong polar order whose presence becomes more pronounced at larger system sizes. This finding rules out the possibility of a pure classical nematic state in favor of a more complex transition involving an interplay between S_n^{LC} and S^F. Remarkably, S^F takes off at a lower value of η than S_n^{LC} for all system sizes. Contrary to what was observed at low density, at high density orientational order emerge due to the onset of apolar order. Let us notice that the later onset of the noisy polar order coincides with the onset of density instabilities (see Fig. 4.5).

4.2.2 Classification of the transitions

Assuming that there are true long-range order at high and low densities, here we look for evidence to determine the character of the phase transition. At this point it has to be said that Gregoire *et al.* [40, 41] show that systems of self-propelled polar particles

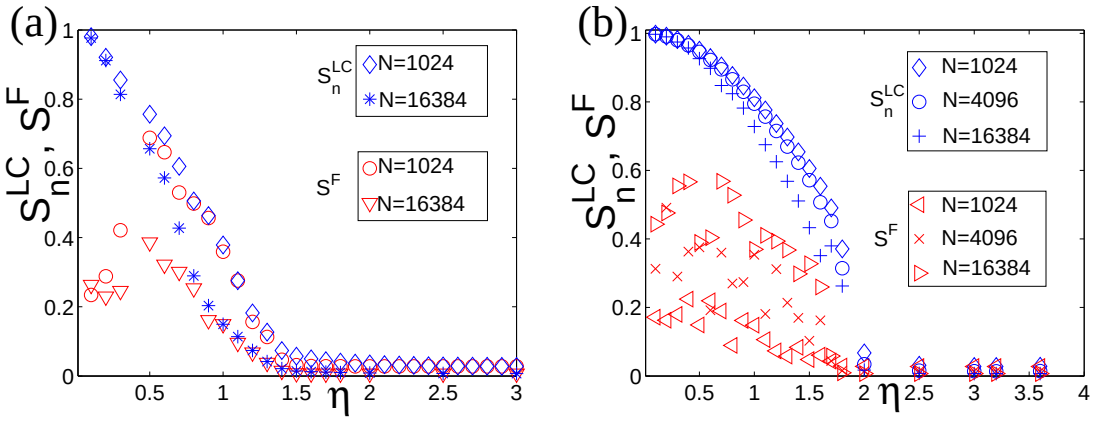

Figure 4.8: S_n^{LC} and S^F vs. η for various system sizes. (a) $\rho = 0.25$ and (b) $\rho = 2.0$. Notice that at low density S^F seems to decrease with the system size N, while at high density the opposite is observed.

interacting by a F-alignment exhibit a first-order phase transition[2]. We wonder whether the order parameter S_n^{LC} in self-propelled polar particles interacting this time through an apolar LC-alignment exhibits such an evidence of first-order phase transition. The Binder cumulant G is good measure to distinguish between first and second order phase transitions. The cumulant G is defined as $G = 1 - \langle S_n^{LC4} \rangle / \left(3 \langle S_n^{LC2} \rangle^2 \right)$ and measures the fluctuations of the order parameter. G falling to negative values near the critical noise intensity η_c is a sign of a discontinuous transition. Fig. 4.9 shows the Binder cumulant G as function of the noise intensity η for various densities. As it can be seen in the figure, for all the explored densities and all values of η, G remains positive. However, G presents a minimum which becomes more pronounced at lower densities. It could be argued that the minimum exhibited by G, particularly at low densities, could become negative for much larger system sizes. To solve this problem we look at other estimates of the character of the phase transition, particularly at the fluctuations of the order parameter.

Fluctuations of S_n^{LC} and S^F at low and high densities are remarkably different. Fig. 4.10 shows the time evolution of S_n^{LC} and S^F at low density (a), and high density (b). Notice that in Figs. 4.10(a) and (b), the temporal average of the order parameter is roughly the same, $S^{LC} \sim 0.6$. This implies that Fig. 4.10(a) shows the outcome of simulations performed at a much lower noise, $\eta = 0.5$, than simulations shown in Fig. 4.10(b) and

[2]Nagy *et al.* [102] has recently called into question the first-order character of the transition reported in [40, 41].

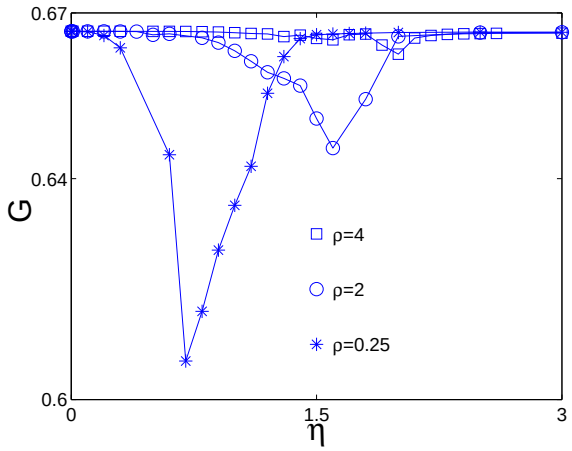

Figure 4.9: Binder cumulant G as function of the noise intensity η for various densities ρ. The curves $\rho = 0.25$ and 0.2 correspond to simulations with $N = 16384$ particles, while the curve $\rho = 4.0$ was performed with $N = 8192$ particles. Notice that G is positive for all values of η and all densities.

corresponding to $\eta = 1.5$. Though the implemented noise in (a) is much weaker than in (b), the order parameter fluctuations in (a) are much larger than in (b). Furthermore, simulations in (a) correspond to a much larger system size, $N = 2^{14}$, than simulations in (b), $N = 2^{12}$

First and second order phase transitions can also be distinguished by studying the distribution of the order parameter. Typically, in a second order phase transition, the time series of the order parameter shows that order parameter fluctuates around it mean value as observed in Fig. 4.10(b). The mode of the distribution is close to the mean value, and the distribution is single peaked. In a first order phase, the time series exhibits abrupt jumps from high to low values of the order parameter. Consequently, the mode of the distribution is no longer close to its mean, and the distribution is bimodal. Fig. 4.11 shows the distribution of the order parameter S_n^{LC} at high and low densities. $p\left(S_n^{LC}\right)$ measures the occurrence frequency of S_n^{LC} in the time evolution of a simulation. The different curves in the figure correspond to different values of η. Fig. 4.11(a) shows $p\left(S_n^{LC}\right)$ at high density and as expected from Fig. 4.10(b), the distribution is single peaked for all values of η. All the evidence at high density, Binder cumulant, time series of the order parameter, and its distribution $p\left(S_n^{LC}\right)$ points towards a second-order phase transition[3].

[3]The previous assertion is based on the available data, i.e., system sizes explored. A crossover to a

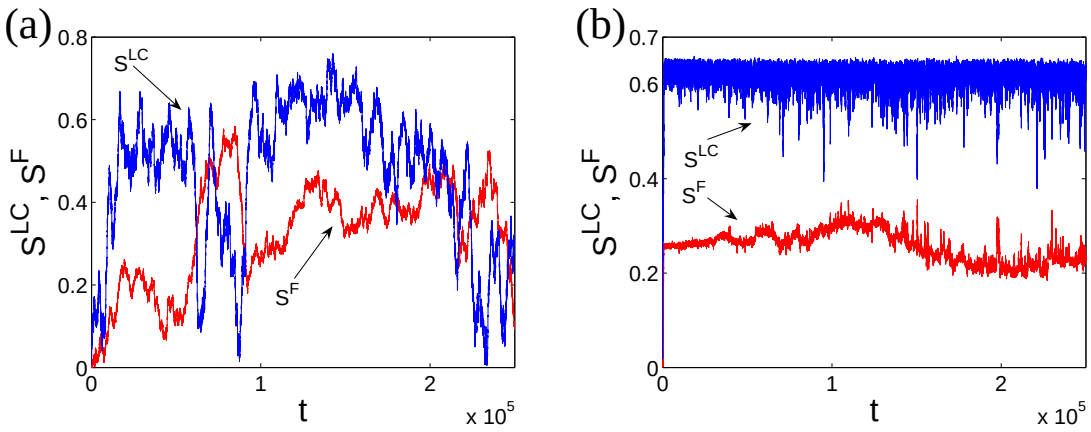

Figure 4.10: Time evolution of the order parameters at high and low density. (a) corresponds to the low density case with $\rho = 0.25$ and noise intensity $\eta = 0.5$, while (b) illustrates the high density case with $\rho = 0.4$ and $\eta = 1.5$. Notice that in both, (a) and (b), the temporal average of the LC-order parameter is $S^{LC} \sim 0.6$. However, fluctuations at low density are huge compared to fluctuations at high density.

At low density, the situation is by far much more ambiguous. Fig. 4.11(b) shows that $p\left(S_n^{LC}\right)$ is sharp at large values of η and becomes broader for low values of the noise intensity. The inset shows $p\left(S_n^{LC}\right)$ for three values of η, $\eta = 0.5$, 0.6, and 0.7. Though the distributions are very noisy, the bimodal character of the distributions are strongly suggested. Finally, we presume that at low density, the pronounced minimum of G can take negative values for large enough system sizes. We speculate that at low density the transition is of different character than at high density, and presumably first-order.

4.2.3 Comparison of the transitions at low and high density

We have gathered numerical evidence that strongly suggests that the transition is remarkably different at high and low densities. There is an obvious physical difference between these two extreme scenarios. At high density, meaning above the percolation threshold, the local orientation information travels through a percolated systems. Presumably, at these high densities, the constant motion of particles leading to a constant changing neighborhood is responsible to the emergence of long-range order. This mixed scenario together with the numerical evidence of a continuous transition at high density suggest that the observed transition could be of mean-field type. On the other hand, at low density,

first-order transition for larger system sizes, as observed for polar interactions in [41], cannot be excluded.

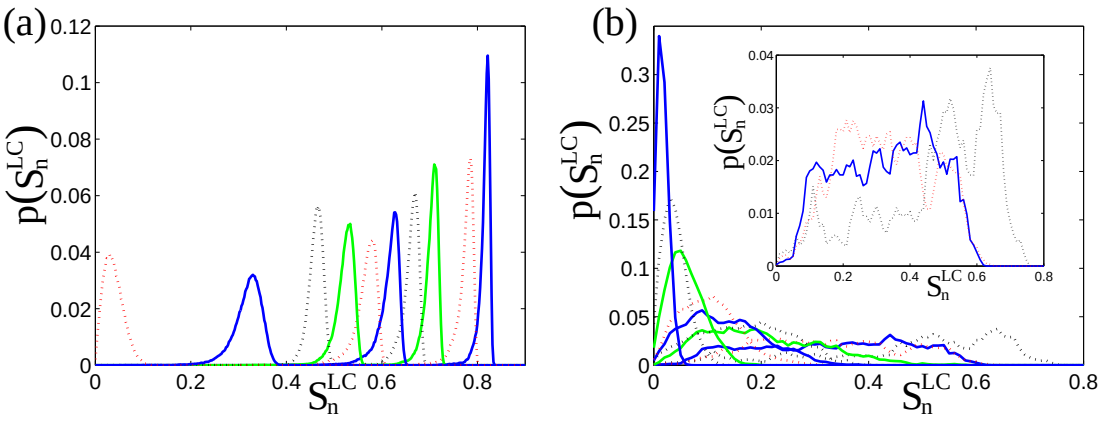

Figure 4.11: Distribution of the order parameter S_n^{LC} at high and low densities. $p\left(S_n^{LC}\right)$ measures the occurrence frequency of S_n^{LC} in the time evolution of a simulation. (a) $p\left(S_n^{LC}\right)$ at high density, $\rho = 4.0$ and $N = 2^{12}$. The different curves correspond from right to left to $\eta = 1.0$, 1.1, 1.2, 1.3, 1.4, 1.5, 1.6, 1.7, 1.8, 1.9 and 2.0. (b) $p\left(S_n^{LC}\right)$ at low density, $\rho = 0.25$ and $N = 2^{14}$. The different curves correspond from left to right to $\eta = 0.5$, 0.6, 0.7, 0.8, 0.9, 1.0, 1.1, 1.2, 1.3, 1.4 and 1.5. The inset of figure (b) shows an amplification of the curves $\eta = 0.5$, 0.6, and 0.7.

far below the percolation threshold, the information does no longer travel along a percolated systems and it requires, to be transferred, the physical movement of the particles. Consequently, the transition at low density has to be highly dependent of the clustering properties of the system, and its nature depends upon them.

These thoughts are illustrated by the following two figures. In Fig. 4.12 the order parameters S_n^{LC} and S^F as function of η are compared at three densities, $\rho = 0.25$, 2.0 and 4.0. The figure suggests through a simple fitting $S_n^{LC} \sim (\eta_c - \eta)^\beta$ that as we move from low to high densities the character of the transition changes, becoming of mean-field type at very high densities. We warn that the fitting argument has to be taken just as an illustration. The interplay between orientational order and clustering effects is summarized by the η-ρ phase diagram sketch shown in Fig. 4.13. The lines separating disorder from orientational order (solid-circle line), and clustering from no clustering (open-circle line) were estimated using a system size of $N = 2^{14}$ particles. To accurately determine the separatrices, a system size analysis has to be performed. Fig. 4.13 represents a rough estimate of the actual η-ρ phase diagram and has to be considered just as a sketch. However, Fig. 4.13 suffices to illustrate that at high density, orientational order emerges before (= at higher values of η) the onset of density instabilities, while at low density both, orientational order and clustering, set in at the same value of the noise intensity. Notice that

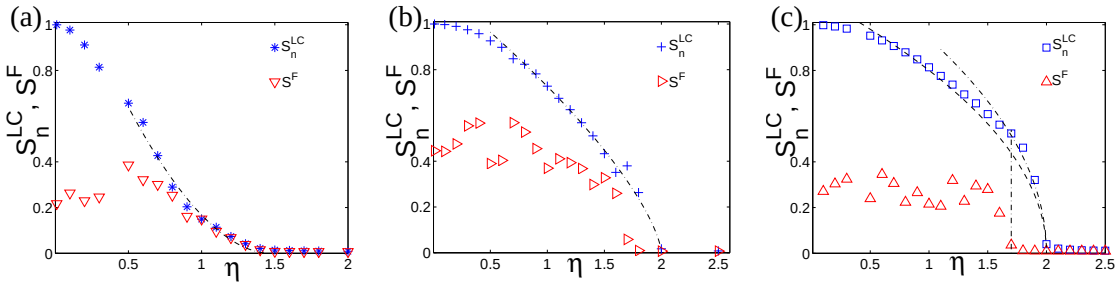

Figure 4.12: Comparison of the order parameters S_n^{LC} and S^F vs. η at different densities: $\rho = 0.25$ (a), 2.0 (b) and 4.0 (c). (a) and (b) were performed with $N = 2^{14}$ particles, while (c) with $N = 2^{12}$. The dash-dotted curves are fittings S_n^{LC} using $S_n^{LC} \sim (\eta_c - \eta)^\beta$. In (a) $\beta = 1.8$ and $\eta_c = 1.45$, in (b) $\beta = 0.7$ and $\eta_c = 2.0$, and in (c) $\beta = 0.5$ and $\eta_c = 2.0$. In (c) the dashed curve corresponds to a fitting of the first 16 data points to the left of η_c, while the dash-dotted to the first 5 points. In both cases $\beta = 0.5$. The vertical line indicates the onset of density instabilities.

it can be speculated that $\eta_c(\rho)$ saturates with ρ.

In the following sections we provide arguments and evidence that support all these hypotheses.

4.3 Understanding clustering

This section is mainly devoted to the understanding of clustering effects at low density. We start out by studying an apparently unrelated problem, particle diffusion in the ordered state. The problem will prove to be helpful not only to understand clustering at low density but also orientational order at low values of the noise intensity.

4.3.1 Diffusion in the order state

Assume that initially all particles are located at the origin and move in direction $+\widehat{\mathbf{x}}$ with speed v_0. Assume, in addition, that they box inside which the move is infinite. Since initially each particle can see all the others, the problem can be described initially by a mean-field. According to Eq. (4.1.2), particles calculate the same common direction of motion. The additive noise η_i^t acts just as a perturbation around the global common direction of motion. This average vector can be thought as an external field that guides the particles. The problem becomes, as described in chapter 2, a directed random walk. In consequence, the time evolution of the particle density $\rho(\mathbf{x}, t)$ obeys the following

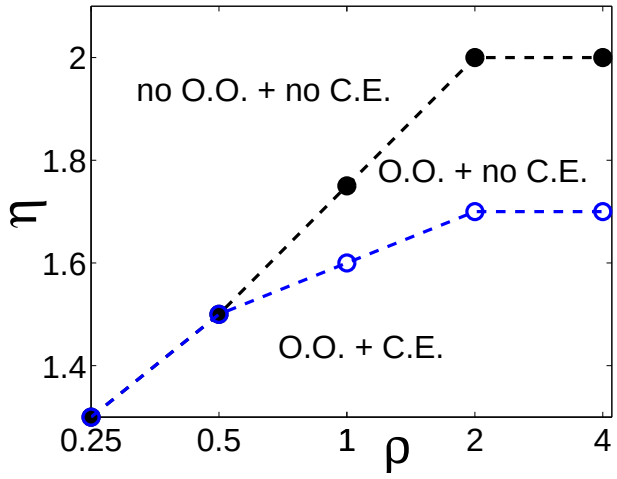

Figure 4.13: Sketch of the system phase diagram η-ρ. Number of particles $N = 2^{14}$. The solid-circle line corresponds to $\eta_c(\rho)$ and separates orientational order (O.O.) from no orientational order (no O.O.) regions. The open-circle line is the separatrix between clustering effects (C.E.) and no C.E. regions.

equation:

$$\partial_t \rho(\mathbf{x},t) = -v_0 V(\eta)\partial_x \rho(\mathbf{x},t) + D_{\mathbf{x}}(\eta)\bigtriangledown^2 \rho(\mathbf{x},t) \tag{4.3.1}$$

where $D_{\mathbf{x}}(\eta)$ is given by:

$$D_{\mathbf{x}}(\eta) = (1-c)v_0^2 \Delta t\,, \tag{4.3.2}$$

with $c = \langle\cos(\theta)\rangle^2 = [2/\eta\sin(\eta/2)]^2$, as described in Chapter 2 and in [108]. Notice that Δt in Eq.(4.3.2) plays the role of the inverse of the turning rate, i.e., α^{-1} in Eq. (2.3.4). $V(\eta)$ is the mean projection of the instantaneous velocity of the particles on the $+\widehat{\mathbf{x}}$ semi-axis. Let $P(\eta_i^t = \phi)$ be the probability for the ith-particle of getting a random angular noise ϕ. Assuming that the noise, as implemented in the simulation, is obtained from a step function distribution of width η, $V(\eta)$, which by definition is $V(\eta) = \int_0^{2\pi} d\theta P(\theta)\cos(\theta)$, takes the form:

$$V(\eta) = \frac{2\sin(\eta/2)}{\eta}\,. \tag{4.3.3}$$

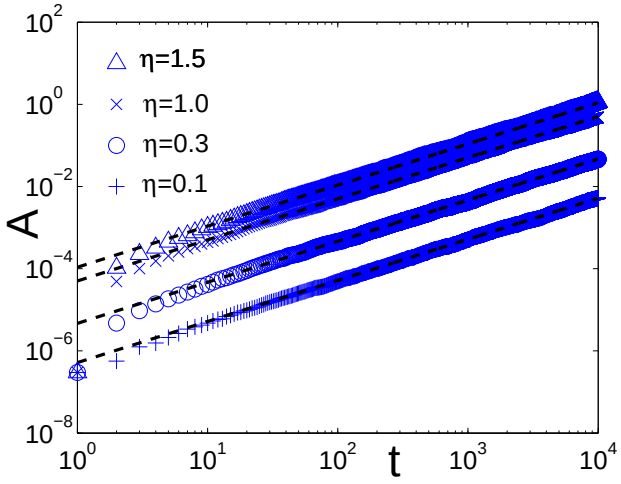

Figure 4.14: Spreading A of the swarm around it center of mass vs. time for different values of the noise intensity η. Symbols correspond to measurements of $\langle \mathbf{x}^2 \rangle$ in simulations with $N = 1000$ particles, which initially were located at the origin and all pointing in direction $+\widehat{\mathbf{x}}$. The dashed lines correspond to the approximation $A = D_{\mathbf{x}}(\eta)t$.

Notice that in the limit of $\eta \to 0$, $V(\eta) \to 1$ and $D_{\mathbf{x}}(\eta) \to 0$, i.e., there is only a deterministic transport of particles without any diffusion, while in the limit of $\eta \to 2\pi$, $V(\eta) \to 0$ and $D_{\mathbf{x}}(\eta) \to v_0^2 \Delta t$, i.e., there is only diffusion (which takes its maximum value) and no convective flux. The description given by Eq. (4.3.1) is valid while the cloud of particles remains being a percolating giant cluster. For longer times, this picture fails and particles loose their coherent motion. The interaction among particles is such that keep particles moving in the same direction as long as they can see each other, but cannot prevent them from slowly moving apart due to the stochastic kicks on the direction of motion.

Fig. 4.14 shows the time evolution of the spreading A of the swarm around it center of mass in simulations with $N = 1000$ particles at various noise intensities η. As said above, particles have been initially located at the origin and oriented in direction $+\widehat{\mathbf{x}}$. The spreading around the center of mass is simply defined as $A = \langle \mathbf{x}(t)^2 \rangle - \langle \mathbf{x}(t) \rangle^2$. The dashed lines in Fig. 4.14 correspond to the approximation $A = D_{\mathbf{x}}(\eta)t$, where $D_{\mathbf{x}}(\eta)$ is given by Eq. (4.3.2). To obtain A analytically, both, $\langle \mathbf{x}(t) \rangle$ and $\langle \mathbf{x}(t)^2 \rangle$ are calculated from Eq. (4.3.1). For $\langle \mathbf{x}(t) \rangle$, both sides of Eq. (4.3.1) are multiplied by $\mathbf{x}$ and integrated over the space to get a simple expression for $\partial_t \left(\langle \mathbf{x}(t) \rangle \right)$ from which finally $\langle \mathbf{x}(t) \rangle$ is obtained. And similarly for $\langle \mathbf{x}(t)^2 \rangle$, but this time both sides of Eq. (4.3.1) are multiplied by $\mathbf{x}^2$. As

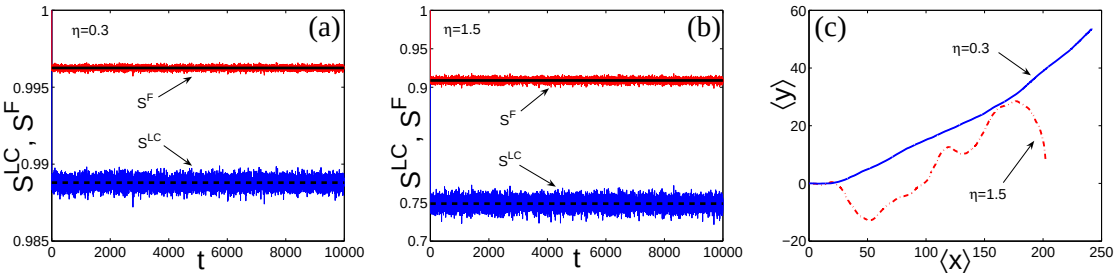

Figure 4.15: (a) and (b): S^{LC} and S^F vs. time for a simulation performed with $N = 1000$ particles initially located at the origin and all pointing in direction $+\hat{\mathbf{x}}$. The noise intensity corresponds to $\eta = 0.3$ in (a) and $\eta = 1.5$ in (b). The solid black line refers to the prediction for S^F given by Eq. (4.3.7), while the dashed line is the approximation for S^{LC} given by Eq. (4.3.10). (c) shows the trajectory of the center of mass of the particle ensemble corresponding to the numerical experiment with $\eta = 0.3$ (solid line) and $\eta = 1.5$ (dot-dashed line).

shown in Fig. 4.14, the agreement between simulations and Eq. (4.3.1) is fairly good.

Now, we turn our attention to the orientational order parameters exhibited by this cloud of moving particles. At first glance, it might seem that since the bunch of particles moves coherently, then S^F and S^{LC} have to be $S^F = S^{LC} = 1$. Figs. 4.15(a) and (b) show S^F and S^{LC} as function of time in simulation with $N = 1000$ particles at two values of η, $\eta = 0.3$ (a) and $\eta = 1.5$ (b). The figures prove that S^F and S^{LC} inside the coherently moving swarm are still function of η. The explanation is as follows. Since each particle can see all the others, all of them calculate the same average direction α_0. This is strictly true for $\eta < \pi$. Then, the angular dynamics of the ith-particle takes the form:

$$\theta_i^{t+1} = \alpha_0 + \eta_i^t \,. \tag{4.3.4}$$

This means that the probability of finding a randomly chosen particle pointing in direction θ is

$$P(\theta) = \frac{1}{\eta} g(\theta, \alpha_0, \eta) \,, \tag{4.3.5}$$

where $g(\theta, \alpha_0, \eta)$ is defined to be 1 when $\alpha_0 - \eta/2 \leq \theta \leq \alpha_0 + \eta/2$, and 0 otherwise, i.e., $g(\theta, \alpha_0, \eta) = H(\alpha_0 + \eta/2 - \theta).H(\eta/2 - \alpha_0 + \theta)$, where $H(x)$ is a Heaviside function.

S^F in terms of $P(\theta)$ takes the form

$$S^F = \left[\left(\int_0^{2\pi} d\theta P(\theta) \cos(\theta) \right)^2 + \left(\int_0^{2\pi} d\theta P(\theta) \sin(\theta) \right)^2 \right]^{1/2} . \tag{4.3.6}$$

Inserting Eq. (4.3.5) into Eq. (4.3.6), we obtain:

$$S^F = \frac{2}{\eta} \sin(\eta/2) . \tag{4.3.7}$$

Similarly, S^{LC} in terms of $P(\theta)$ is defined as

$$\begin{aligned} S^{LC} &= \frac{1}{4} + \frac{3}{2} \left[\frac{1}{4} + \int \int_0^{2\pi} d\theta d\theta' P(\theta) P(\theta) \right. && (4.3.8) \\ &\quad \left. \left(\cos^2(\theta) \sin^2(\theta') - \cos(\theta) \sin(\theta) \cos(\theta') \sin(\theta') \right) \right]^{1/2} . && (4.3.9) \end{aligned}$$

Inserting Eq. (4.3.5) into Eq. (4.3.8), we find the following expression for S^{LC}:

$$S^{LC} = \frac{1}{4} + \frac{3}{2} \sqrt{1/4 + \left(4 \cos^2(\eta/2) \sin^2(\eta/2) - \eta^2 \right) / \left(4\eta^2 \right)} . \tag{4.3.10}$$

Fig. 4.16 compares Eqs. (4.3.7) and (4.3.10) and simulations performed with $N = 1000$ particles. The solid and dashed curve correspond to Eq. (4.3.7) and Eq. (4.3.10), respectively. The symbols correspond to temporal averages of simulated time series of S^F and S^{LC} as shown in Figs. 4.15(a) and (b). The agreement is remarkably good for the 10^4 integration steps that the simulations span. It is worth to notice that during such period the center of mass of the swarm travels a distance d much larger than the interaction radius ϵ, i.e., $d \gg \epsilon$ (see Fig. 4.15(c)), while the swarm spreading around its center of mass is comparatively very small. Despite the fact the swarm moves in a very coherent way, as we increase η, the value of the order parameters drop (see Figs. 4.15(a) and (b)), and the center of mass performs a more tortuous meandering trajectory as shown in Figs. 4.15(c). Interestingly, the fluctuations of the center of mass around the $\widehat{\mathrm{y}}$ axis are much larger than the swarm spreading around its center. This is due to large fluctuations of the average total momentum vector that are not reflected in the fluctuations of its modulus, i.e., S^F. The total momentum vector fluctuates in direction and modulus, but S^F fluctuations are only related to fluctuations of its modulus. The same applies to orientation tensor Q and to its associated scalar liquid crystal order parameter S^{LC}.

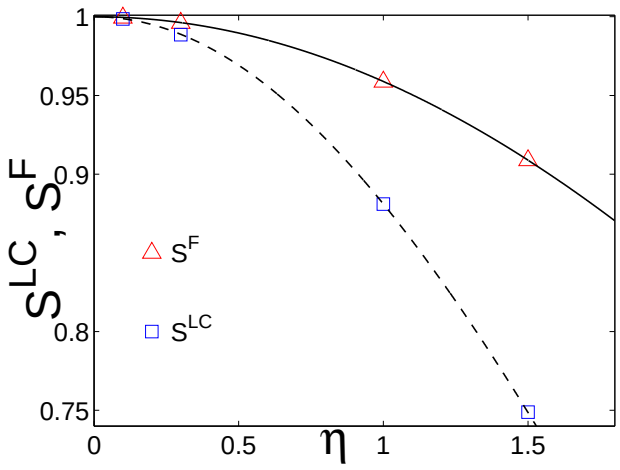

Figure 4.16: S^F and S^{LC} as function of η as predicted by Eq. (4.3.7) (solid curve) and (4.3.10) (dashed curve), respectively. Symbols correspond to S^F (triangles) and S^{LC} (squares) measured in simulations performed with $N = 1000$ particles initially located at the origin and all pointing in direction $+\widehat{\mathbf{x}}$.

It was said above that this simple description of the swarm is valid until the spreading around the center of mass is such that the density of the moving cluster falls below percolation. However, the presence of a finite correlation length shifts the threshold to higher densities. In consequence, the actual *coherence* density is a function of η. Now, imagine that the swarm does not evolve in an infinite space, but in a box with periodic boundary conditions. Assume in addition that the size L^2 of the box is such that N/L^2 is much larger than the *coherence* density. Can this system be described in term of such simple equations as Eq. (4.3.7) and (4.3.10) for all times? And if the initial condition of the system is completely random, does the system reach the same steady state? For a random initial condition, we cannot expect an steady state with a unique direction of motion. We assume that two opposite direction of motion emerge, α_0 and $\alpha_0 + \pi$, and that the angular dynamics of the i-th particle is simply given by:

$$\theta_i^{t+1} = \begin{cases} \alpha_0 + \eta_i^t & \text{with probability} \quad p_+ \\ (\alpha_0 + \pi) + \eta_i^t & \text{with probability} \quad p_- \end{cases} \tag{4.3.11}$$

In consequence, $P(\theta) = (p_+/\eta)g(\theta, \alpha_0, \eta) + (p_-/\eta)g(\theta, \alpha_0 + \pi, \eta)$. Replacing this expression into Eqs. (4.3.6) and (4.3.8), we find that $S^F = (2/\eta)\sin(\eta/2)(p_+ - p_-)$, while S^{LC} remains to be given by Eq. (4.3.10). These ideas are tested in Fig. 4.17. The simulations

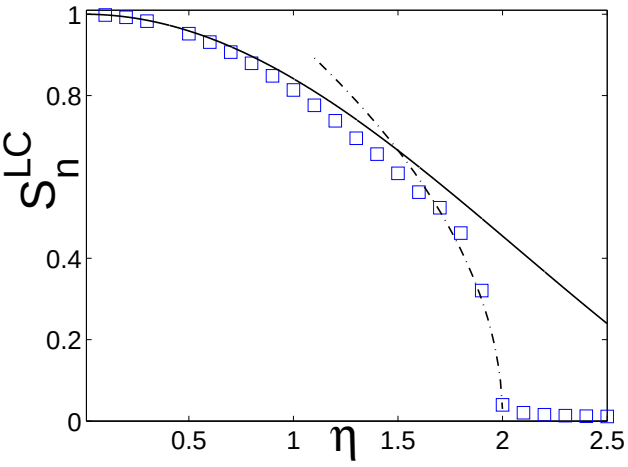

Figure 4.17: S_n^{LC} vs. η. Symbols correspond to simulations with $N = 2^{12}$ particles at density $\rho = 4$ in a box with periodic boundary conditions and random initial conditions. The dot-dashed curve is a fitting of the first 8 data points to the left of $\eta_c = 2$ through $S^{LC} \sim (\eta_c - \eta)^{\beta}$, where $\beta = 0.46 \pm 0.03$. The solid curve corresponds to Eq. (4.3.10).

were performed with $N = 2^{12}$ particles at density $\rho = 4$ in a box with periodic boundary conditions. The initial condition was random and the simulations ran for 10^6 time steps. The solid curve corresponds to the approximation given by Eq. (4.3.10), where no fitting parameter is used. The dot-dashed curve is a fitting of the first 8 data points to the left of $\eta_c = 2$ assuming $S^{LC} \sim (\eta_c - \eta)^{\beta}$, where $\beta = 0.46 \pm 0.03$. The figure shows that Eq. (4.3.10) provides a good approximation of S^{LC} for small values of η, but fails to describe orientational order at large values of the noise intensity. Particularly the transition from disorder to order is not captured by Eq. (4.3.10). Chapter 5 will be devoted to understand this particular problem.

4.3.2 Cluster size distribution at low density

Fig. 4.6 suggests that at low density the onset of orientational order coincides with the onset of clustering. We define the onset of clustering as the point at which the cluster size distribution is no longer monotonically decreasing. Fig. 4.18 shows the cluster size distribution $p(m)$ for various values of the noise intensity η at low density. The simulations were performed with $N = 2^{14}$ particles at density $\rho = 0.25$. The figure indicates that a transition from a monotonically decreasing distribution for large values of η to a

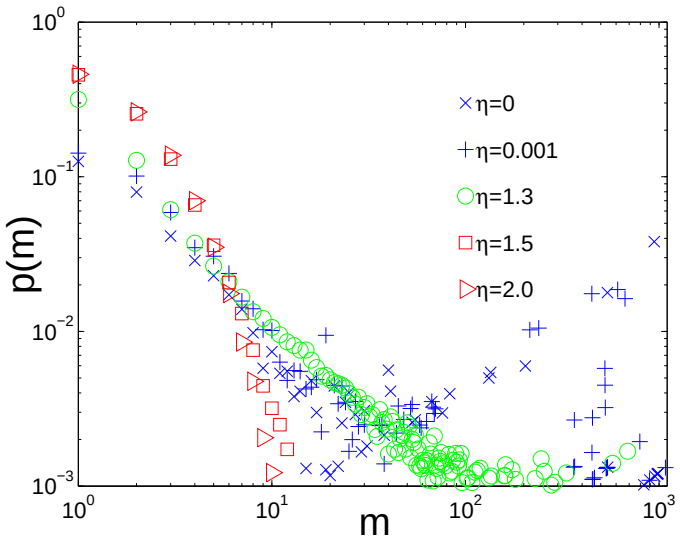

Figure 4.18: Clustering at different values of the noise intensity η at low density. Simulation performed with $N = 2^{14}$ particles at density $\rho = 0.25$. Notice the transition from a monotonically decreasing distribution for large values of η to a bimodal distribution for small enough values of noise intensity. A comparison with Fig. 4.6(a) reveals that onset of clustering coincides with the onset of orientational order.

bimodal distribution for small enough values of noise intensity takes place. Interestingly, at the transition the cluster size distribution becomes scale-free. A comparison with Fig. 4.6(a) reveals that effectively clustering and orientational order emerge together. In this subsection we look for an explanation for the observed clustering phenomena.

Through the study of the coherence of an initially perfectly oriented swarm, we have learned that clusters have a finite life time before they break into parts. Now we incorporate the fact that a moving cluster when meets particles whose relative direction of motion is such that $|\Delta\theta| < \pi/2$, collects them, provided the noise intensity η is low enough. If the topology of the system is a finite torus, these two effects, spreading of particles due to fluctuation in the direction of motion and collection of particles due to random "collisions" of clusters, reach an equilibrium and the cluster size distribution (CSD) becomes a steady distribution. As in Chapter 3 and [100], the evolution of the CSD is described as

follows:

$$\begin{aligned}
\dot{n}_1 &= 2B_2 n_2 + \sum_{k=3}^{N} B_k n_k - \sum_{k=1}^{N-1} A_{k,1} n_k n_1 \\
\dot{n}_j &= B_{j+1} n_{j+1} - B_j n_j - \sum_{k=1}^{N-j} A_{k,j} n_k n_j \\
&\quad + \frac{1}{2} \sum_{k=1}^{j-1} A_{k,j-k} n_k n_{j-k} \quad \text{for} \quad j = 2, ..., N-1 \\
\dot{n}_N &= -B_N n_N + \frac{1}{2} \sum_{k=1}^{N-1} A_{k,N-k} n_k n_{N-k}
\end{aligned} \tag{4.3.12}$$

where the dot denotes time derivative, B_j represents the rate for a cluster of mass j of loosing a particle, and is defined as

$$B_j = \frac{D_{\mathbf{x}}(\eta)}{d^2} \sqrt{j}\,, \tag{4.3.13}$$

and $A_{j,k}$ is the collision rate between clusters of mass j and k, defined by

$$A_{j,k} = \frac{v_0 2\epsilon}{A} \left(\sqrt{j} + \sqrt{k} \right) . \tag{4.3.14}$$

In Eq. (4.3.13), d denotes the typical distance that separates particles on the boundary from their nearest neighbors. In this way, $d^2/D_{\mathbf{x}}(\eta)$ is the characteristic time a particle on the boundary needs to detach from the cluster. The splitting rate B_j is proportional to the inverse of that characteristic time multiplied by the number of particles on the boundary, which we approximate by $\sqrt{j}$. On the other hand, the collision rate $A_{j,k}$ is a concept shared from kinetic gas theory [79] which tells us that the collision rate between two disk-like particles A and B is proportional to the relative velocity of the particles and the sum of their diameters. We assume the diameter of a cluster of mass j can be approximated by $2\epsilon\sqrt{j}$.

Rescaling Eq. (4.3.12) by introducing a new time variable $\tau = tD_{\mathbf{x}}(\eta)/d^2$, we retrieve the dimensionless set of equations given by Eqs. (3.3.26) in Chapter 3, where this time the dimensionless parameter P is defined as $P = (2v_0\epsilon d^2) / (AD_{\mathbf{x}}(\eta))$. Recall that the critical dimensionless parameter P_c is a function of the number of particles in the system,

resp. the number of ordinary differential equation in Eq. (4.3.12). Fig. 3.26 indicates that $P_c(N) \sim N^{\beta_0}$ where $\beta_0 = -1.026 \pm 0.023$. For simplicity, we take $P_c(N) = C\, N^{-1}$ and obtain that there is critical spatial diffusion $D_{\mathbf{x}}(\eta_c)$ defined by $D_{\mathbf{x}}(\eta_c) = (2v_0\epsilon d^2\rho)/C$. From this expression, we predict that the critical orientational noise η_c which triggers clustering (and orientation) is given by the transcendental equation:

$$\eta_c = \frac{2\sin(\eta_c/2)}{\sqrt{1-\frac{2\rho\epsilon d^2}{v_0 C\Delta t}}}\,. \tag{4.3.15}$$

Provided d is known, then η_c can be estimated through Eq. (4.3.15). An estimate of d would imply a systematic numerical study of either the cluster size distribution or η_c. Though, this can be regarded as a drawback of Eq. (4.3.15), this expression allows us to understand the the behavior of η_c with respect to ρ and v_0 at low density.

4.4 Comparison with diffusive particles

We have gathered evidence that indicates that at high density this non-equilibrium system exhibits a continuous kinetic phase transition from disorder to order. We have mentioned that an equilibrium two dimensional system with continuum symmetry cannot exhibit long-range orientational order [33]. Here, we wonder what causes long-range orientational order in this self-propelled particle system. Fig. 4.12 suggests that as we move from low to high densities the character of the transition changes and approaches a mean-field transition at very high densities. Typically a mean-field description, resp. a mean-field transition, implies a good mixing of particles. Contrary to the classical static XY-model, self-propelled particles move and mix up in such a way that each particle has a constantly changing neighborhood. Does this mixing induce a mean-field transition or is the self-propulsion responsible for the transition? In Chapter 5 we will introduce a simple mean-field approach to understand the emergence of orientational order from a disorder state. We will show that in such theoretical framework the replacement of the self-propulsion of the particles by an uncoordinated spatial diffusion leads to the same type of transition. This finding strongly suggests that at high density the mixing of particles makes possible the mean-field transition. In this section we test these ideas through simulations.

Imagine a system of two-dimensional Brownian particles with an internal state variable θ_i^t which might represent the orientation of their long axis. The motion of the particles is completely decoupled from θ_i^t. However, the dynamics of the internal state variable

θ_i^t does depend on the particle position. Brownian particles interact through the internal state variable as active particles do through their direction of motion (see Eq. (4.1.2)). For Brownian particles θ_i^t does not affect particle movement. The evolution of the ith-Brownian particle is given by:

$$\mathbf{x}_i^{t+\Delta t} = \mathbf{x}_i^t + v_0 \left(\cos(\gamma_i^t), \sin(\gamma_i^t)\right) \Delta t \tag{4.4.1}$$

$$\theta_i^{t+\Delta t} = \arg\left(\sum_{|\mathbf{x}_i^t - \mathbf{x}_j^t| \leq \epsilon} \mathbf{f}\left(\mathbf{v}(\theta_j^t), \mathbf{v}(\theta_i^t)\right) \right) + \eta_i^t \tag{4.4.2}$$

where γ_i^t is an uncorrelated random angle obtained from a step distribution of width 2π, i.e., $\gamma_i^t \in [0, 2\pi]$. Notice that the equations of motion of active and diffusive particles only differ in the center of mass update rule (see Eqs. (4.1.1) and (4.4.1)), while the orientation dynamics remains the same (see Eqs. (4.1.2) and (4.4.2)).

Fig. 4.19 compares the apolar order parameter S_n^{LC} as function of η in simulations of active and Brownian particles. The simulations were performed with $N = 2^{14}$ particles at two densities, $\rho = 0.25$ and 2.0. The figure shows that at high density the behavior $S_n^{LC}(\eta)$ in active and Brownian particles is strikingly similar. This finding suggests that Brownian particles also exhibit a transition to orientational order. The result also supports the above mentioned mean-field transition hypothesis for high density.

At low densities, on the other hand, active and Brownian particles differ dramatically. Fig. 4.19 shows that Brownian particles at low density exhibit weak orientational order compared to active particles. This is not surprising since we have learned that at low density orientational order in active particles emerges as result of clustering. In Brownian particles, the uncoupled spatial and angular dynamics do not allow a transition to clustering. In consequence, Brownian particles at low density cannot exhibit orientational ordering for any (non-zero) finite value of η.

Fig. 4.20 shows both order parameters, S_n^{LC} and S^F, in Brownian particles at low and high density. As expected, since Brownian particles and their interactions are apolar, polar order does not emerge. Consequently, the emergence of orientational order observed in Brownian particle at high density corresponds to a genuine nematic order. Recall that the transition to orientational order reported in active particle at high density comes accompanied for low values of η by a non-vanishing polar order (see Fig. 4.8).

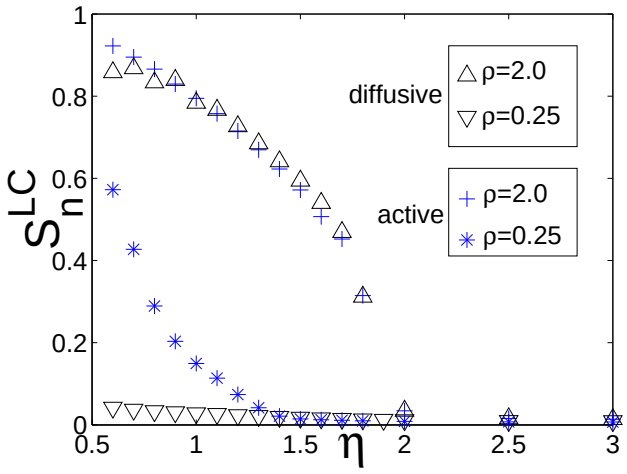

Figure 4.19: Comparison of S_n^{LC} vs. η in simulations of active and diffusive particles. The dynamics of active particles is given by Eqs.(4.1.1) and (4.1.2), while Brownian particles obey Eqs. (4.4.1) and (4.4.2). Simulations with $N = 2^{14}$ particles.

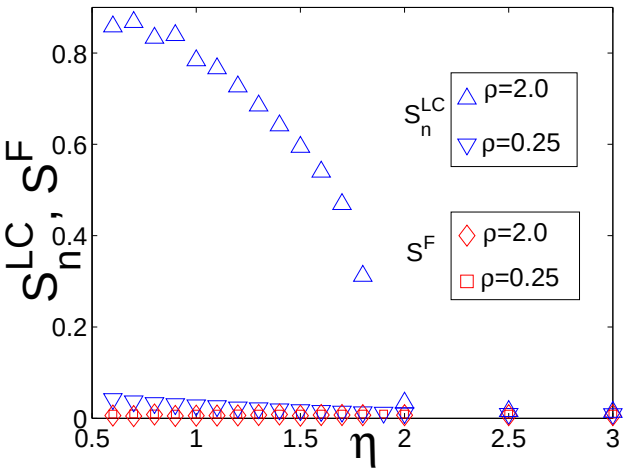

Figure 4.20: S_n^{LC} and S^F vs. η for diffusive particles. Notice that diffusive particles do not exhibit any polar order at all.

4.5 Conclusions

We have modeled and simulated a two-dimensional system of (polar) self-propelled particles interacting through a liquid crystal (apolar) alignment mechanism. Through the individual-based simulations, we have gathered multiple evidence that indicates that the system exhibits for low enough orientational noise a kinetic phase transition to orientational order whose character strongly depends on particle density. At high densities, i.e., when the orientation information travels through a percolated system, the liquid crystal order parameter presents a continuous phase transition. Additional polar order emerges simultaneously with density instabilities in a second transition. On the other hand, at low densities, i.e., when the transfer of orientational information requires the physical motion of the particles, the transition to orientational order is initiated by the onset of clustering, where individual clusters have strict polar order.

In addition, it has been shown that the dynamics of a coherently moving swarm can be described as a system of random walkers guided by an external field. From this approach, a rate equation description of clustering has been derived that is qualitatively in line with simulations at low density.

Finally, it has been tested whether the long-range orientational order observed in self-propelled particles also appears for interacting Brownian particles with an internal state variable. The outcome of the simulations has revealed that Brownian particles at high density also can exhibit long-range order. This finding together with comparison between self-propelled and Brownian particles has revealed that at high density the strong mixing of particles, due to particle motion, produces the transition.

In summary, the self-propulsion of particles leads to local polar effects that particularly influence particle transport and clustering effects, which in turn affect the character of the phase transition to orientational order. These results might shed some light to elucidate the complex interplay between local orientational order and local density in large-scale pattern of interacting self-propelled entities as gliding bacteria [27,28] and crawling cells [93].

Chapter 5

Continuum theory for self-propelled particles

Introduction

In the previous Chapters we have seen that self-propelled particles (SPPs) with local interactions can organize into large-scale patterns. Flocks of birds [26], swarms of bacteria [27, 35, 109, 110], sperm cells [111], mixtures of microtubules and motors [112], are biological examples for such a behavior. Beyond the complexity of each particular system, we observe that there are some few common features which cause the emergence of long-range order in these systems: the active motion of the particles and a velocity alignment mechanism. In this Chapter we wonder in which way the local velocity alignment mechanism affects the emerging macroscopic pattern.

The Vicsek-model [34] is considered the simplest model of SPPs which exhibits collective motion. In this model, point-like particles moving with a velocity vector of constant magnitude interact by aligning their velocity direction to the local average velocity. One can think of this model as a model of moving spins, in which the velocity of the particles is given by the spin-vector. Going further in this analogy with spin systems, we denote this alignment mechanism, as in Chapter 4, ferromagnetic (F-alignment). The temperature associated with spin-systems enters in the Vicsek-model as noise in the alignment mechanism. It was shown that two-dimensional SPPs with F-alignment and additive noise exhibit a second-order phase transition[1] which leads for low enough noise to long-range

[1] Chaté et al. have questioned the second-order phase transition even when additive noise is imple-

orientational order [34, 102]. For different choices of system parameters and different choices of the noise term (non-additive noise term), simulations show, however, first order phase transitions to orientational order [40, 41]. Interestingly, in equilibrium systems of non-moving spins with continuum symmetry this transition cannot occur [33,104,105].

F-alignment is one possible alignment mechanism, but clearly not the only one. If a system of self-propelled rods interacts simply by volume exclusion as described in Chapter 3, resp. [100], particles may end up moving in the same direction as well as in opposite directions. A biological realization of such a system are myxobacteria, which in the early stages of their life-cycle organize their motion by simply pushing each other [27]. A similar effect without active motion occurs in liquid-crystals at high density where particles get locally aligned [72]. In analogy to these systems we name this mechanism hence liquid-crystal alignment (LC-alignment). In a system of SPPs with LC-alignment particles align their velocity to the local average director. In simulations of a model of SPPs with LC-alignment it was found that at high density these moving "liquid-crystal" spins exhibit a second-order phase transition leading to long-range orientational order for low noise[2]. Notice that the orientational order observed in SPPs with LC-alignment refers to the emergence of a global director in the system, while for F-alignment orientational order refers to the appearance of a global direction of motion.

Toner and Tu were the first to look for a macroscopic description of SPPs with F-alignment. Their approach was a phenomenological hydrodynamical description based on symmetry arguments for which they derived general macroscopic equations for a large class of individual-based models of SPPs with F-alignment [36, 42, 113]. In this approach many of the parameters in the model are difficult to derive from the microscopic dynamics. Recently Grégoire et al. proposed an alternative approach based on the Boltzmann equation [114] and could explain in a systematic way the functional form proposed by Toner and Tu [42] by use of an ad-hoc collision term.

The case of LC-alignment has been much less explored. Recently, Ramaswamy et al. proposed a phenomenological hydrodynamical description for driven, but non-persistent, particles with LC-alignment [31]. The approach is comparable to the Toner and Tu description for F-alignment. One of the striking results of this approach is the giant number

mented [41], claiming that in the thermodynamical limit the system exhibits a first-order transition. However, very recently Vicsek et al. have insisted about the continuous character of the transition for additive noise [102] providing evidence not present in their pioneering work [34]. The actual nature of the transition for additive noise is currently under debate.

[2]The numerical evidence supporting this assertion has been given in the previous chapter.

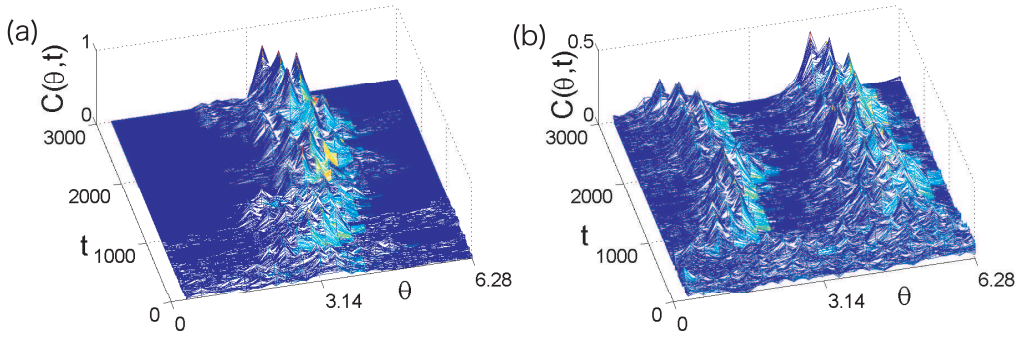

Figure 5.1: Temporal evolution of the velocity direction distribution (angular distribution) in simulations with very fast angular relaxation. (a) corresponds to F-alignment, while (b) to LC-alignment. Number of particles $N = 100$, radius of interaction $\epsilon = 2$, linear system size $L = 42.4$, and noise amplitude $\eta = 0.25$.

fluctuations of particles in the ordered state, which has been confirmed in simulations by Chaté et al. [48] and in granular media experiments by Narayan et al. [50]. More recent simulations have suggested that these fluctuations are linked with intrinsic phase separation of SPPs into regions of high and low density [49].

Here, we derive mean-field type description for SPPs with F- and LC- alignment. Numerical evidence provided by individual-based simulations indicates that SPPs with both F and LC-alignment (and additive noise) can exhibit a continuous kinetic phase transition in two dimensions. The derived mean-field equations allow us to study ferromagnetic as well as liquid-crystal interactions among particles. Through this approach the phase transition to orientational order observed in individual-based simulations at high density for F and LC-alignment is correctly captured. Furthermore, we show that the critical noise amplitude η_c is such that $\eta_C^{LC} < \eta_C^F$ in the mean-field description as well as in the individual-based simulations in both investigated cases.

5.1 Individual-based model

5.1.1 Equations of motion

We consider point-like particles moving at constant speed in a two dimensional space and assume an over-damped situation such that the state of particle i at time t is given by its

position $\mathbf{x}_i$ and its direction of motion θ_i. The evolution of these quantities follow:

$$\dot{\mathbf{x}}_i = v_0 \mathbf{v}(\theta_i) \tag{5.1.1}$$

$$\dot{\theta}_i = -\gamma \frac{\partial U}{\partial \theta_i}(\mathbf{x_i}, \theta_i) + \tilde{\eta}_i(t) \tag{5.1.2}$$

where γ is a relaxation constant, and U the interaction potential between particles, and hence $\frac{\partial U}{\partial \theta_i}(\mathbf{x_i}, \theta_i)$ defines the velocity alignment mechanism. Moreover, v_0 represents the active velocity of the particles, $\mathbf{v}(\theta_i)$ is defined as $\mathbf{v}(\theta_i) = (\cos(\theta_i), \sin(\theta_i))$, and $\tilde{\eta}_i(t)$ is an additive white noise applied to the direction of motion. The evolution Eqs. (5.1.1) and (5.1.2) are expressed in terms of first derivatives. In this way, v_0 in Eq. (5.1.1) can be considered as an active force divided by a translational friction coefficient, and γ in Eq. (5.1.2) as the inverse of a rotational friction coefficient.

In analogy to spin systems, the ferromagnetic velocity alignment mechanism is given by a potential defined as:

$$U_F(\mathbf{x_i}, \theta_i) = -\sum_{|\mathbf{x}_i - \mathbf{x}_j| \leq \epsilon} \cos(\theta_i - \theta_j) \tag{5.1.3}$$

where ϵ is the radius of interaction of the particles. For the liquid-crystal alignment mechanism, we choose the potential introduced by Lebwohl and Lasher to study liquid crystal interactions on a lattice [101] which reads:

$$U_{LC}(\mathbf{x_i}, \theta_i) = -\sum_{|\mathbf{x}_i - \mathbf{x}_j| \leq \epsilon} \cos^2(\theta_i - \theta_j) \tag{5.1.4}$$

One can add a coupling strength coefficient to the expression (5.1.3) and (5.1.4). We assume that the coupling strength is absorbed in γ in Eq. (5.1.2). Notice that the potential given by Eq. (5.1.3) exhibits one minimum, while Eq. (5.1.4) has two minima, which correspond to particles pointing in the same direction and particles pointing in opposite directions.

In the limiting case of very fast angular relaxation we expect Eqs. (5.1.1) and (5.1.2) to be approximated by the updating rules:

$$\mathbf{x}_i^{t+\Delta t} = \mathbf{x}_i^t + v_0 \mathbf{v}\left(\theta_i^t\right) \Delta t \tag{5.1.5}$$

$$\theta_i^{t+\Delta t} = \arg\left(\sum_{\left|\mathbf{x}_i^t - \mathbf{x}_j^t\right| \leq \epsilon} \mathbf{f}(\mathbf{v}(\theta_j^t), \mathbf{v}(\theta_i^t)) \right) + \eta_i^t \tag{5.1.6}$$

where $\arg(\mathbf{b})$ indicates the angle of a vector $\mathbf{b}$ in polar coordinates, and η_i^t is a delta-correlated white noise of strength η ($\eta_i^t \epsilon \left[-\frac{\eta}{2}, \frac{\eta}{2}\right]$). Given two vectors $\mathbf{a}$ and $\mathbf{b}$, $\mathbf{f}(\mathbf{a}, \mathbf{b})$ is defined as follows. For F-alignment, $\mathbf{f}(\mathbf{a}, \mathbf{b}) = \mathbf{a}$ and Eqs. (5.1.5) and (5.1.6) becomes Vicsek model [34]. For LC-alignment, $\mathbf{f}$ takes the form:

$$\mathbf{f}(\mathbf{a}, \mathbf{b}) = \begin{cases} \mathbf{a} & \text{if} \quad \mathbf{a}.\mathbf{b} \geq 0 \\ -\mathbf{a} & \text{if} \quad \mathbf{a}.\mathbf{b} < 0 \end{cases} . \tag{5.1.7}$$

Recall Eqs. (5.1.5), (5.1.6), and (5.1.7) have been introduced and analyzed in the previous Chapter.

5.1.2 Order parameters

If particles interact through the F-alignment mechanism, and assuming low noise amplitude, they get locally aligned, and locally point in a similar direction. The question is whether such local alignment may lead to a global orientational order in which a macroscopic fraction of the particles in the system points in a similar direction. The order parameter that quantifies this phenomenon is the modulus of the normalized total momentum (analogous to the magnetization in the XY-model [104, 105]) that we express as:

$$S^F = \left| \frac{1}{N} \sum_{i=0}^{N} \mathbf{v}\left(\theta_i^t\right) \right| \tag{5.1.8}$$

where N stands for the total number of particles in the system. S^F takes the value 1 when all particle move in the same direction. On the other hand, S^F is equal to 0 in the disordered case in which particles point in any direction with equal probability. This can be also observed through the velocity direction distribution, that in two dimensions becomes an angular distribution $C(\theta)$. For high values of the noise, $C(\theta)$ is flat. When the noise is decreased below a critical noise η_c, an instability arises in the system (characterized by a single peak) indicating the onset of orientational order as shown in Fig. 5.1(a). The order parameter S^F expressed in terms of $C(\theta)$ takes the form:

$$S^F = \left[\left(\int_0^{2\pi} d\theta C(\theta) \cos(\theta) \right)^2 + \left(\int_0^{2\pi} d\theta C(\theta) \sin(\theta) \right)^2 \right]^{1/2} \tag{5.1.9}$$

On the other hand, if for example, half of the particles move in one direction, and the other half in the opposite direction, S^F is also 0. Clearly, S^F cannot distinguish such a state and the completely disordered state. However, LC-alignment may induce such a kind of local arrangement of particle velocities, and lead to a global orientational order state in which there are two opposite main directions of motion in the system. To study such orientation ordering, one uses the order matrix Q of liquid crystals [72]. For two dimensions one takes the largest eigenvalue S^{LC} of Q and obtain the following scalar orientational order parameter:

$$S^{LC} = \frac{1}{4} + \frac{3}{2}\sqrt{\frac{1}{4} - \frac{1}{N^2}\left\{\sum_{i,j}^{N} v_{xi}^2 v_{yj}^2 - v_{xi}v_{yi}v_{xj}v_{yj}\right\}} \tag{5.1.10}$$

where v_{xi} and v_{yi} are defined as $v_{xi} = \cos(\theta_i)$ and $v_{yi} = \sin(\theta_i)$. The orientational order parameter S^{LC} takes the value 1 when all particles are aligned along the same director, and the value $\frac{1}{4}$ in the disordered phase where particles move with equal probability in any direction. Again this can be observed through the velocity direction distribution $C(\theta)$. In this case, for low values of the noise amplitude, as shown in Fig. 5.1(b), an instability arises in the system with the characteristic of having two peaks separated by 2π. In terms of $C(\theta)$, S^{LC} reads:

$$S^{LC} = \frac{1}{4} + \frac{3}{2}\left[\frac{1}{4} - \left(\int_0^{2\pi} d\theta C(\theta)\cos^2(\theta)\right)\left(\int_0^{2\pi} d\theta C(\theta)\sin^2(\theta)\right) + \left(\int_0^{2\pi} d\theta C(\theta)\cos(\theta)\sin(\theta)\right)^2\right]^{1/2} \tag{5.1.11}$$

Recall Eqs. (5.1.8), (5.1.9), (5.1.10) and (5.1.11) have already been introduced and analyzed in the previous Chapter. Here, we have included them for making the reading of this Chapter easier and selfcontained.

5.2 Mean-field approach

5.2.1 Derivation of the mean-field approach

A system of SPPs may alternatively be described through a density field $\psi(\mathbf{x}, \mathbf{v}(\theta), t) = \psi(\mathbf{x}, \theta, t)$ in such a way that the particle density at a point $\mathbf{x}$ is given by

$$\rho\left(\mathbf{x}, t\right) = \int_0^{2\pi} \psi\left(\mathbf{x}, \theta, t\right) d\theta \tag{5.2.1}$$

while the velocity direction distribution (or angular distribution) can be expressed as:

$$C\left(\theta, t\right) = \int_\Omega \psi\left(\mathbf{x}, \theta, t\right) d\mathbf{x} \tag{5.2.2}$$

We recall that in the individual-based model the kinetic energy is conserved, while the momentum is not. For F-alignment, the system tends to increase the total momentum, while for LC-alignment the tendency is to decrease it. The continuum approach has to reflect that particles can re-orient their velocity direction but always move at constant speed. On the other hand, the number of particles has to be conserved. Under these assumptions the following evolution equation for $\psi(\mathbf{x}, \theta, t)$ is obtained:

$$\partial_t \psi = D_\theta \partial_{\theta\theta} \psi - \partial_\theta \left[F_\theta \psi\right] - \bigtriangledown \left[\mathbf{F}_x \psi\right] \tag{5.2.3}$$

where $F_\theta \psi$ and $\mathbf{F}_x \psi$ are deterministic fluxes which are associated to the local alignment mechanism and active migration, respectively, and D_θ refers to the diffusion in the direction of motion.

Let us derive the specific expressions for D_θ, F_θ and $\mathbf{F}_x$. D_θ depends on the square of the noise amplitude. For example, if in the individual-based simulations $\eta_i(t)$ is implemented by taking at each time step a random variable from a step distribution of width η, D_θ is given $D_\theta = \eta^2 \Delta t/24$, where Δt is the temporal time step. F_θ contains the interaction of a particle located at $\mathbf{x}$ and pointing in direction θ with all neighboring particles which are at a distance less than ϵ from $\mathbf{x}$, and so takes the form:

$$F_\theta = -\gamma \int_{R(\mathbf{x})} d\mathbf{x}' \int_0^{2\pi} d\theta' \frac{\partial U(\mathbf{x}, \theta, \mathbf{x}', \theta')}{\partial \theta} \psi(x', \theta', t) \tag{5.2.4}$$

where $U(\mathbf{x}, \theta, \mathbf{x}', \theta')$ represents the pair potential between a particle located at $\mathbf{x}$ and pointing in direction θ, and another at $\mathbf{x}'$ and pointing in direction θ'. $R(\mathbf{x})$ denotes the interaction neighborhood around $\mathbf{x}$. If $\mathbf{x}'$ is inside $R(\mathbf{x})$, then $U(\mathbf{x}, \theta, \mathbf{x}', \theta') = U(\theta, \theta')$. Finally, F_θ can be thought as the "torque" felt by a particle located at $\mathbf{x}$ and pointing in direction θ. Notice that we have implicitly assumed that the two-particle density can be approximated in terms of the one-particle probability, i.e., $\psi(\mathbf{x}, \theta; \mathbf{x}', \theta', t) \simeq \psi(\mathbf{x}, \theta, t)\psi(\mathbf{x}', \theta', t)$, as in the mean-field approximation for coupled oscillators [115] or generic equations for angular order [116].

The expression for $\mathbf{F}_x$ is straightforward and is directly related to the velocity of particle at $\mathbf{x}$ and pointing in direction θ,

$$\mathbf{F}_x = v_0 \mathbf{v}(\theta) \tag{5.2.5}$$

5.2.2 Angular distribution

Integrating both sides of Eq. (5.2.3) over the space Ω we obtain an evolution equation for $C(\theta, t)$ which still depends on $\psi(\mathbf{x}, \theta, t)$. In the following we assume a homogeneous spatial distribution of particles $\psi(\mathbf{x}, \theta, t) = C(\theta, t)\rho_0/N$, where ρ_0 is defined as $\rho_0 = N/L^2$, being L the linear size of the system. With these assumptions the equation for the temporal evolution of $C(\theta, t)$ reads:

$$\frac{\partial C(\theta,t)}{\partial t} = D_\theta \frac{\partial^2 C(\theta,t)}{\partial \theta^2} + \gamma \frac{\pi \epsilon^2}{L^2} \partial_\theta \left[\left\{ \int_0^{2\pi} d\theta' \frac{\partial U(\theta,\theta')}{\partial \theta} C(\theta',t) \right\} C(\theta,t) \right] \tag{5.2.6}$$

5.2.3 Linear stability analysis for F-alignment

For both F- and LC-alignment the homogeneous angular distribution is a steady state of Eq. (5.2.6). We determine the onset of the ordered state by studying the linear stability of the disordered state. First let us look at the F-alignment. By dividing both sides of Eq. (5.2.6) by $\gamma \pi \epsilon^2 / L^2$, and redefining time as $\tau = (\gamma \pi \epsilon^2 / L^2) t$, and $D'_\theta = D_\theta / [\gamma \pi \epsilon^2 / L^2]$ one obtains:

$$\frac{\partial C(\theta,t)}{\partial \tau} = D'_\theta \partial_{\theta\theta} C(\theta,t) + \partial_\theta \left[\left\{ \int d\theta' \sin(\theta - \theta') C(\theta',t) \right\} C(\theta,t) \right] \tag{5.2.7}$$

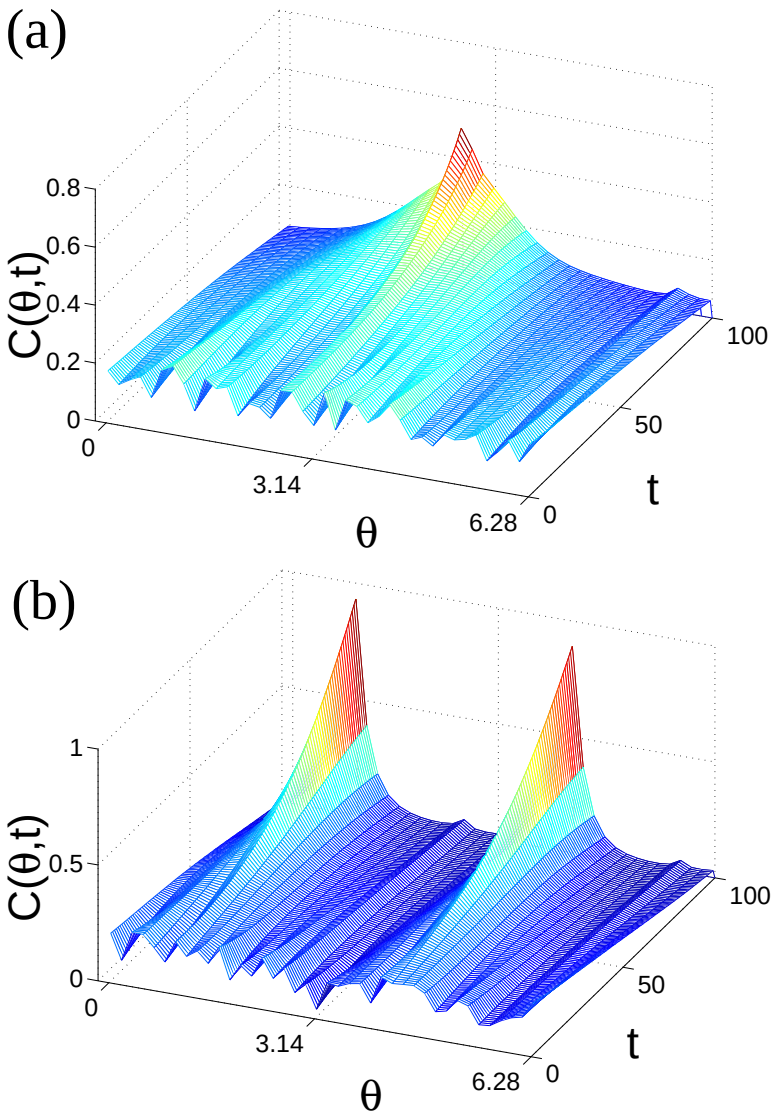

Figure 5.2: Temporal evolution of $C(\theta, t)$. (a) F-alignment, numerical integration of Eq. (5.2.7) with $D_\theta = 0.28$. (b) LC-alignment, numerical integration of Eq. (5.2.11) with $D_\theta = 0.014$. For both (a) and (b), $C^* = 0.3183$, $\Delta t = 0.001$ and $\Delta\theta = 0.16$. The initial condition is a random perturbation around C^*. Notice that for F-alignment a single peak emerges, while for LC-alignment the distribution develops two peaks.

Now, consider a weak perturbation of the homogeneous pattern:

$$C(\theta,t) = C^* + C_0 e^{in\theta} e^{\lambda\tau} \tag{5.2.8}$$

Notice that $e^{in\theta}$ are eigenfunctions of the operators emerging from the linearization of Eq. (5.2.7) about the homogeneous steady state. By substituting into Eq. (5.2.7) and keeping terms linear in C_0 we obtain the following expression for the eigenvalues:

$$Re(\lambda) = -D'_\theta n^2 + \pi C^* \delta_{n,1} \tag{5.2.9}$$

This means that the only mode which can become unstable is $n = 1$. The condition for the instability of the homogeneous state takes the form:

$$\rho_0 > \frac{2D_\theta}{\gamma\pi\epsilon^2} \tag{5.2.10}$$

where $\rho_0 = N/L^2$. For a given noise amplitude, expressed by D_θ, there is a critical particle density above which the homogeneous solution is no longer stable. Fig. 5.1(a) shows that in individual-based simulations indeed a single peak emerges in the system for low density. Fig. 5.2(a) confirms that such qualitative behavior is recovered by numerical integration of Eq.(5.2.7).

5.2.4 Linear stability analysis for LC-alignment

Applying analogous procedure for LC-alignment yields:

$$\begin{aligned} \frac{\partial C(\theta,t)}{\partial\tau} &= D'_\theta \partial_{\theta\theta} C(\theta,t) \\ &+ \partial_\theta \left[\left\{ \int d\theta' 2\cos(\theta-\theta')\sin(\theta-\theta') C(\theta',t) \right\} C(\theta,t) \right] \end{aligned} \tag{5.2.11}$$

Again the weakly perturbed homogeneous ansatz given by Eq. (5.2.8) is considered. As before $e^{in\theta}$ are eigenfunctions of the linearized operators. Substituting Eq. (5.2.8) into Eq. (5.2.11) and keeping terms linear in C_0 the following expression for the eigenvalues is obtained:

$$Re(\lambda) = -D'_\theta n^2 + 2\pi C^* \delta_{n,2} \tag{5.2.12}$$

As for the F-alignment, there is only one mode which could become unstable, but this time it is $n = 2$. This mode is the only one that exhibits two peaks separated by π, which corresponds to two population of particles migrating in opposite direction. In this case, the instability condition of the homogeneous states takes simply the form:

$$\rho_0 > \frac{4D_\theta}{\gamma\pi\epsilon^2} \tag{5.2.13}$$

Again, this inequality defines a critical density for a given noise amplitude above which the homogeneous solution is no longer stable. Fig. 5.1(b) shows the emergence of these two peaks for LC-alignment in individual-based simulations. Numerical integration of Eq. (5.2.11), see Fig. 5.2(b), confirms that this behavior is recovered qualitatively by the mean-field description.

Eqs. (5.2.10) and (5.2.13) indicate that the instability of the homogeneous state is given by ρ_0, D_θ, and ϵ, the range of interaction. The critical density is inversely proportional to ϵ^2, hence when ϵ goes to infinity the critical density goes to 0. The interpretation of this is straightforward, $\epsilon \longrightarrow \infty$ indicates that particles have infinity "visibility", i.e., each particle can sense all other particles in the system. In this way, the collective behavior has to emerge independent of particle density. The other limiting case is represented by $\epsilon \longrightarrow 0$. In this case particles do not interact and in consequence no organized motion is possible.

From these findings a phase diagram is derived that shows where the system exhibits velocity orientational order (see Fig. 5.3).

5.2.5 Spatially inhomogeneous steady states

Through the linear stability analysis it has been found for which conditions the homogeneous distribution (disordered state) becomes unstable. To study the nonlinear behavior of these instabilities in more detail, Eq. (5.2.6) can be integrated numerically. Details about the numerical methods are given in the Appendix C. Fig. 5.2 has shown already the temporal evolution of $C(\theta, t)$. The initial condition is a homogeneous state with small random perturbations: $C(\theta_n, t = 0) = C^* + \eta(n)$, where θ_n denotes the discrete angular variable, C^* is the constant unperturbed homogeneous state, which we have set to be in the unstable regime according to Eqs. (5.2.10) and (5.2.13) for the F- and LC-alignment case, respectively, and $\eta(n)$ is a white noise. In Fig. 5.4 the angular distribution for F- and LC-alignment is shown at different times. $C(\theta, t)$ tends asymptotically to a non-trivial

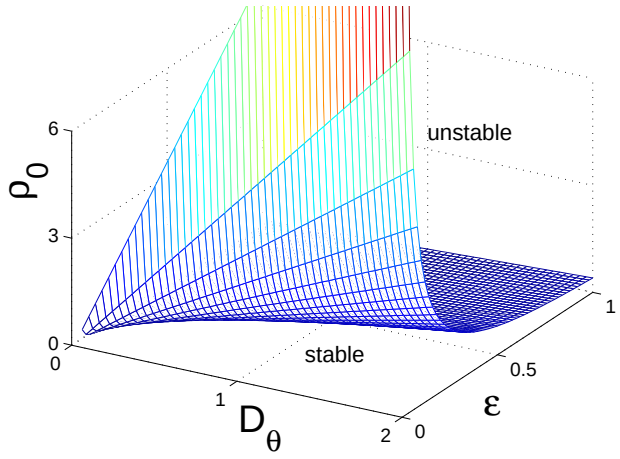

Figure 5.3: Phase diagram derived from the continuum approach. The unstable region corresponds to the velocity orientational order, while stable means no orientational order can be observed.

steady state, see Fig. 5.4. The width of the peaks in the steady state is the result of the competition between influence of rotational diffusion, indicated by D_θ, and the alignment force associated with the interactions.

5.2.6 Scaling of the order parameter close to the transition

For a given density, there is a critical D_{θ_c}. Close to D_{θ_c} we expect to observe that only one mode dominates $C(\theta, t)$. As said before, $n = 1$ is dominant for F-alignment and $n = 2$ governs LC-alignment. The steady state distribution $C_{st}(\theta)$ then takes the form:

$$C_{st}(\theta) \simeq C^* + B_1\sqrt{D_{\theta_c} - D_\theta}\cos(\theta - \theta_0) \tag{5.2.14}$$

for F-alignment, while for LC-alignment the expression reads:

$$C_{st}(\theta) \simeq C^* + B_2\sqrt{D_{\theta_c} - D_\theta}\cos(2(\theta - \theta_0)) \tag{5.2.15}$$

where B_1, B_2 are constants and θ_0 is an arbitrary phase which depends on the initial condition. In both cases the maximum amplitude of $C_{st}(\theta)$ close to the D_{θ_c} grows as $\sqrt{D_{\theta_c} - D_\theta}$. Inserting Eq. (5.2.14) into Eq. (5.1.9) and using, as indicated above, $D_\theta = \eta^2\Delta t/24$, we obtain the scaling of the order parameter S^F:

$$S^F \simeq \tilde{B}_1\sqrt{\eta_c - \eta} \tag{5.2.16}$$

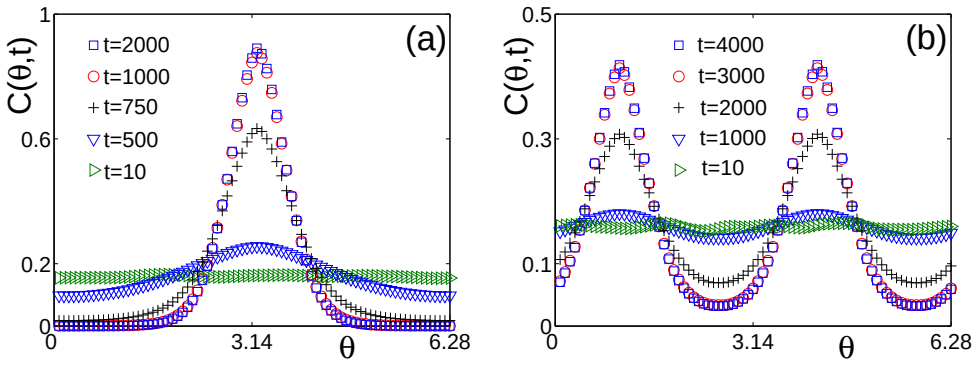

Figure 5.4: Convergence towards the non-trivial stable steady state. (a) F-alignment, numerical integration of Eq. (5.2.7) with $D_\theta = 0.3472$. (b) LC-alignment, numerical integration of Eq. (5.2.11) with $D_\theta = 0.2813$. For both (a) and (b), $C^* = 0.3183$, $\Delta t = 0.001$ and $\Delta\theta = 0.0785$. The initial condition is a random perturbation around C^*. Different curves correspond to different times. Notice that for large values of t curves start to overlap on top of each other.

where $\tilde{B}$ is a constant. To obtain the scaling of the order parameter S^{LC}, we insert (5.2.15) into Eq. (5.1.11):

$$S^{LC} \simeq \frac{1}{4} + \tilde{B}_2\sqrt{\eta_c - \eta} \tag{5.2.17}$$

where again $\tilde{B}_2$ is a constant. $\tilde{B}_1$ and $\tilde{B}_2$ are constants proportional to η_c.

5.2.7 Comparison with individual-based simulations

Individual-based simulations have been performed in the limit case of very fast angular relaxation [34, 102]. In contrast, our mean-field description assumes that there is a finite angular relaxation. Can we expect the mean-field approach to describe scaling of the orientational dynamics in this kind of simulations? We redefine γ as function of the particle velocity v_0 and the particle density ρ. The effective resulting mean-field equation reads:

$$\frac{\partial C}{\partial t}(\theta,t) = D_\theta \frac{\partial^2 C(\theta,t)}{\partial\theta^2} + \gamma(v_0,\rho)\frac{\partial}{\partial_\theta}\left[\left\{\int_0^{2\pi} d\theta' \frac{\partial U(\theta,\theta')}{\partial\theta} C(\theta',t)\right\} C(\theta,t)\right] \tag{5.2.18}$$

where $\gamma(v_0,\rho)$ is an effective interaction strength which absorbs the spatial dynamics.

The scaling obtained from individual-based simulations may now be compared with the one predicted by the mean-field approach. We recall that $D_\theta \sim \eta^2$, where η is the orientational noise amplitude used in individual-based simulations. From this we find that $D_{\theta_c} - D_\theta$ has to be $D_{\theta_c} - D_\theta = K(\eta_c - \eta) + O((\eta_c - \eta)^2)$, where K is a constant. We focus on the LC-alignment and replace this expression into Eq. (5.2.15). We obtain that $C_{st}(\theta) \simeq C^* + B_1\sqrt{\eta_c - \eta}\cos(2(\theta - \theta_0))$, and we know from Eq. (5.2.17) that $S^{LC} \simeq \frac{1}{4} + B_2\sqrt{\eta_c - \eta}$, where B_1 and B_2 are constants.

Fig. 5.5(a) shows a comparison between the scaling predicted by the mean-field approach for S^{LC} (dashed curve) and the one obtained from individual-based simulations for $\rho = 4$ in the limit of very fast angular relaxation (symbols). We find good agreement between the mean-field prediction and the simulations for the scaling of S near η_c that suggests that individual-based simulations with LC-alignment at high densities exhibit a mean-field type transition. Notice that simulations start to deviate exactly at the point where density fluctuations become important (denoted by the dot-dashed vertical line in (5.5)(a)). Let us recall that the mean-field approach implies the assumption of homogeneous density. Evidence also points towards a mean-field transition if we look at the scaling of the maximum amplitude of the angle distribution as function of the angular noise intensity η (see Fig. (5.5)(b)). The order parameter scaling exponent for F-alignment (Vicsek-model) has been found to be 0.45 ± 0.07 [34, 102], which is also in line with the predictions of the presented mean-field theory.

Finally, Fig. 5.6 shows that in individual-based simulations with the same parameters and different (namely LC- and F-) alignment mechanism, in the limit of very fast angular relaxation $\eta_C^{LC} < \eta_C^F$ as predicted by the mean-field theory. Note, however, that the simulations yield $2\eta_C^{LC} \approx \eta_C^F$, while the mean-field description predicts $\sqrt{2}\eta_C^{LC} = \eta_C^F$.

5.3 Concluding remarks

We have derived a mean-field theory for self-propelled particles which accounts for F- and LC-alignment. This approach predicts a continuous phase transition with the order parameter scaling with an exponent one half in both cases. In addition, it yields that the critical noise amplitude below which orientational order emerges is smaller for LC-alignment than for F-alignment, i.e., $\eta_C^{LC} < \eta_C^F$.

These findings were confirmed by individual-based simulations with F- and LC-alignment. In the limit of infinitely fast angular relaxation used in simulations here

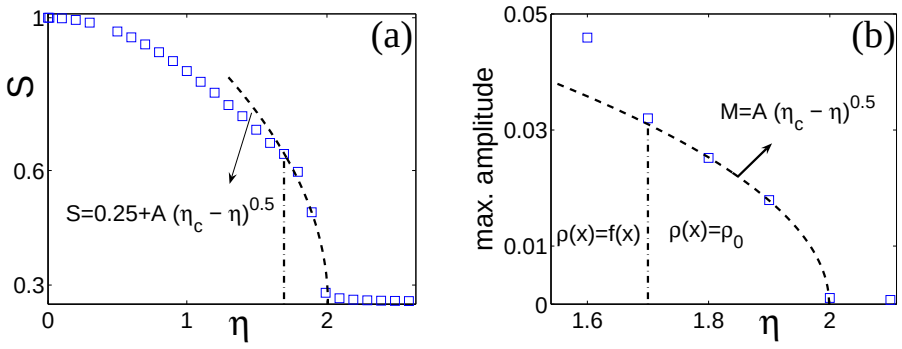

Figure 5.5: (a) Scaling of the scalar order parameter S^{LC} with the noise amplitude η. (b) Scaling of the maxima in $C_{st}(\theta)$ with η. Symbols correspond to simulations with LC-alignment in the limit of very fast angular relaxation. $\rho = 4$ and $N = 2^{12}$. The dashed-curve corresponds to the scaling predicted by the mean-field approach (see Eq. (5.2.17)). The vertical dot-dashed line indicates the onset of clustering effects in the simulations. To the right of that line particle density $\rho(x)$ can be considered constant. To the left of the line, $\rho(x)$ becomes a function of x. For F-alignment in limit of very fast angular relaxation, the scaling of S^F is close to the one predicted by Eq. (5.2.16), compare also [34, 102].

the mean-field theory provides a good qualitative description of the simulations. If simulations were performed by integrating Eqs. (5.1.1) and (5.1.2) with a finite angular relaxation, *i. e.* a finite γ, a direct correspondence between parameters used in simulations and parameters in the mean-field theory can be made and quantitative comparisons become possible. The presented mean-field theory is not an exact coarse-grained description of Eqs. (5.1.1) and (5.1.2). For instance, we have neglected the potential impact of particle-particle correlations. Furthermore, we have assumed spatial homogeneous density to study the emergence of orientational order. Thus, the presented approach does not apply to situations where self-propelled particles show clustering at the onset of orientational order [100]. In summary, a better understanding of the problem should imply the study of the interplay between local orientational order and density fluctuations. We leave that for future research.

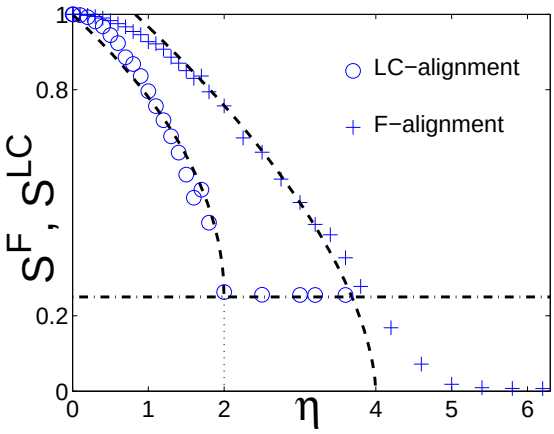

Figure 5.6: Comparing simulations of particles with F-alignment (crosses) and LC-alignment (circles) in the limiting case of very fast angular relaxation. In both cases $N = 2^{14}$ and $\rho = 2.0$. Notice that the order parameter for F-alignment is S^F while for LC-alignment is S^{LC} (See text). The dashed horizontal line indicates the minimum value that S^{LC} could take. The dashed curves correspond to the best fit assuming an exponent 0.5, i.e., η_c was the fitting parameter.

Chapter 6

Summary

Throughout this Thesis many aspects of the physics of self-propelled particles systems ranging from individual to collective motion have been addressed. Chapter 2 has been devoted to the study of the individual motion of self-propelled particles. Specifically, general aspects of two-dimensional active motion, with fluctuations in the speed and the direction of motion, have been studied. We have considered the case in which fluctuations in the speed are not correlated to fluctuations in the direction of motion, and assumed that both processes, fluctuation in the speed and direction of motion, can be described by independent characteristic time-scales. Under these assumptions, a complex transient occurs that can exhibit a series of alternating regimes of motion, for two different angular dynamics which correspond to persistent and directed random walks. Expressions for the mean square displacement and diffusion coefficient have been derived. They have been found to differ from the classical results by additive corrections. The characteristic time-scales of the stochastic motion are exposed in the velocity autocorrelation, which is a sum of exponential forms. It has been shown that uncorrelated fluctuations in the direction of motion and speed might play an important role in the migration of motile microorganisms.

In chapter 3 we have looked for a simple physical mechanism that can induce collective motion in self-propelled particles. Individual-based simulations of self-propelled elongated rods interacting only by volume exclusion exhibit interesting collective motion, i.e., formation of coherently moving groups. Provided the particles are elongated enough, they form densely packed clusters inside which particles are aligned and moving in the same direction. This effect is reflected in the particle speed distribution, particle rotation, and local and global orientational order parameter of the particles. These self-propelled rod-shaped particles that interact only through short-range repulsive interactions, exhibit

a non-equilibrium transition to clustering for sufficient large values of the density and particle aspect ratio. We have defined the onset of clustering by a transition of the cluster size distribution from unimodal to bimodal shape. The transition to clustering observed in individual-based simulations is reproduced by a mean-field description of the cluster size distribution, which yielded a simple criterion for the critical particle aspect ratio κ_c, which predicts κ_c to be inversely proportional to the density. The high density inside the cluster leads to alignment of rods and coordinated motion of all particles in the cluster. Interestingly, the transition to clustering coincides with the point at which the cluster entropy H_C takes its maximum value. Far below the transition, the clustering properties of the system obey the maximum entropy principle applied to H_C, which allowed us to describe the system in terms of the total number of clusters. A comparison with liquid crystal theory reveals that actively moving rods can achieve alignment at much lower densities than Brownian rods resp. particles in equilibrium systems. All these findings are relevant to understand the collective motion of some gliding bacteria as myxobacteria.

The interaction by volume exclusion among self-propelled rods leads to parallel as well as anti-parallel alignment of the rods. The resulting alignment mechanisms is apolar, though particles are, due to their self-propulsion, polar. Chapter 4 has been devoted to the study of a simplified version of the self-propelled rods model. It has been modeled and simulated a two-dimensional system of polar self-propelled particles interacting through an apolar alignment mechanism. It has been shown that the system exhibits for low enough orientational noise a kinetic phase transition to orientational order whose character strongly depends on particle density. At high densities, i.e., above the percolation threshold, the liquid crystal order parameter displays a continuous phase transition. The orientational order state, however, does not correspond to a perfect nematic phase, since the transition involves a non-vanishing polar order. On the other hand, at low densities, i.e., when the transfer of orientational information requires the physical motion of the particles, evidence of a discontinuous phase transition has been found. Contrary to the high density scenario, the transition to orientational order is initiated by an increase of polar order and the onset of clustering. Through the study of interacting Brownian particles, it has been shown that the emergence of long-range orientational order in the self-propelled particle system at high density arises from the mixing of particles rather than the coupling between active motion and particle orientation.

In Chapter 4 it has been shown that collective effects can be achieved by either a polar or an apolar alignment mechanism. Chapter 5 has been devoted to develop a common

theoretical framework to describe the macroscopic dynamics of self-propelled particles under both possible alignment mechanisms. At high density the orientation dynamics is captured by a simple mean-field approach which predicts for low enough noise a single peaked angular distribution for polar alignment, and a bimodal distribution for apolar alignment. The approach also predicts a continuous phase transition in which the order parameter scales with an apparent exponent $1/2$ for both alignment mechanisms. In addition, the critical noise amplitude below which orientational order emerges is smaller for apolar alignment than for polar alignment, in line with individual-based simulations.

In summary, the self-propulsion of particles leads to local polar effects that particularly influence particle transport and clustering effects, which in turn affect the global collective behavior of the system. The results that have been developed throughout this Thesis might shed some light to elucidate the complex interplay between local orientational order and local density in large-scale pattern of self-propelled entities as gliding bacteria [27, 28, 47, 75] and crawling cells [5, 56, 93, 98], among many others.

Appendix A

Calculation of the overlapping area in self-propelled rods simulations

The self-propelled rods simulations require a good and fast estimation of the overlapping area between two rods. This appendix explains how the overlapping area was calculated in simulations.

Suppose two rods intersect as shown in the left panel of Fig. A.1. The first step in order to calculate the intersection area between these two rods is to transform the coordinate system in such a way that the origin of the new system coincides with the center of mass of one of the particle. The coordinate transformation involves also a rotation so that the long-axis of the particle coincides with the new system axis $\widetilde{\mathrm{y}}'$. Notice that now we have to refer to the other rectangle in terms of the relative variables. The procedure is illustrated in the right panel of Fig.A.1.

In the new coordinate system the overlapping area can be easily calculated with the following integral that uses four step functions:

$$\begin{aligned} a(\mathbf{x},\theta,\mathbf{x}',\theta') \;=\; & \int_{-W/2}^{W/2}\int_{-L/2}^{L/2} \Theta\left(\widetilde{b}+l.\sin(\alpha)-b.\cos(\alpha)+\frac{b}{2}\right) \\ & \Theta\left(\frac{b}{2}-\left(\widetilde{b}+l.\sin(\alpha)-b.\cos(\alpha)\right)\right)\Theta\left(\widetilde{a}+l.\cos(\alpha)+b.\sin(\alpha)+\frac{L}{2}\right) \\ & \Theta\left(\frac{L}{2}-(\widetilde{a}+l.\cos(\alpha)+b.\sin(\alpha))\right)\,dl.db \end{aligned} \tag{A.0.1}$$

where $\widetilde{a} = (\cos(\theta),\sin(\theta)).(\mathbf{x}'-\mathbf{x})$, $\widetilde{b} = (-\sin(\theta),\cos(\theta)).(\mathbf{x}'-\mathbf{x})$and $\alpha = \theta-\theta'$. This expression might look complicated, but it can be easily implemented in a computer.

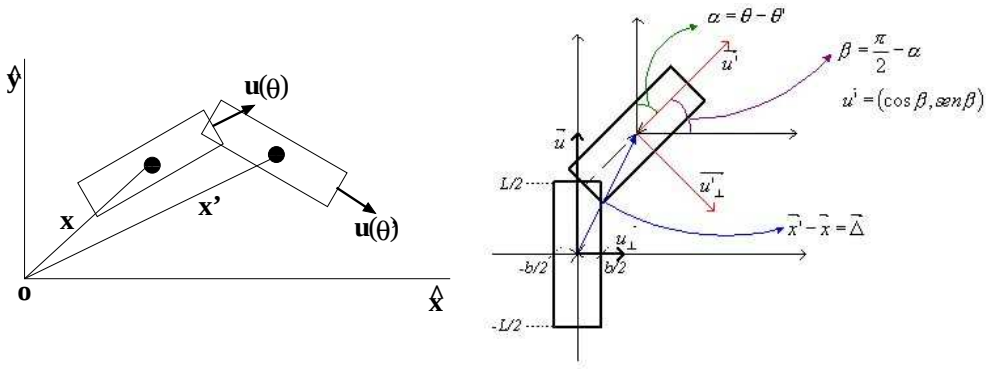

Figure A.1: The left panel sketches the intersection between two rods as seen from a fixed coordinate system. The right panel illustrates the coordinate transformation that is performed to calculate the overlapping area.

Subdividing the area occupied by the rectangle located at $\mathbf{x}'$ and pointing in direction θ' in tiny squares and counting those that obey the condition:

$$-\tfrac{b}{2} \leq x'_{int} \leq \tfrac{b}{2} \text{ and } -\tfrac{L}{2} \leq y'_{int} \leq \tfrac{L}{2},$$

where x'_{int}, y'_{int} refer the interior points of the rectangle located at $\mathbf{x}'$ in the new coordinate system, a good approximation of the overlapping area is obtained.

Though this procedure works very well, it is extremely slow. To speed up the overlapping calculation, the following can be done. After the coordinate system transformation, it is possible to calculate the overlapping area by asking which sides of the rectangle located at $\mathbf{x}'$ intersect the particle located at $\mathbf{x}$. There are four linear equation per side of the rectangle located in $\mathbf{x}'$. Each linear equation can intersect 0, 1 or 2 sides of the rectangle at the origin. If we think that there are four linear equation, the total number of intersection that we may have is 1, 2, 3 or 4. All this represents more than 64 possibilities. In addition the area of overlap may be a triangle, a rectangle or an irregular polygon. Despite of this fact, we can use the symmetries of the problem and to classify all the possible situations in a few cases. In Fig. A.2 some of these cases are shown. Though this procedure is a tedious and hard task, the resulting algorithm is a very fast, gives the exact overlapping area, and reduces the calculation of the overlapping area to a series of "if"s.

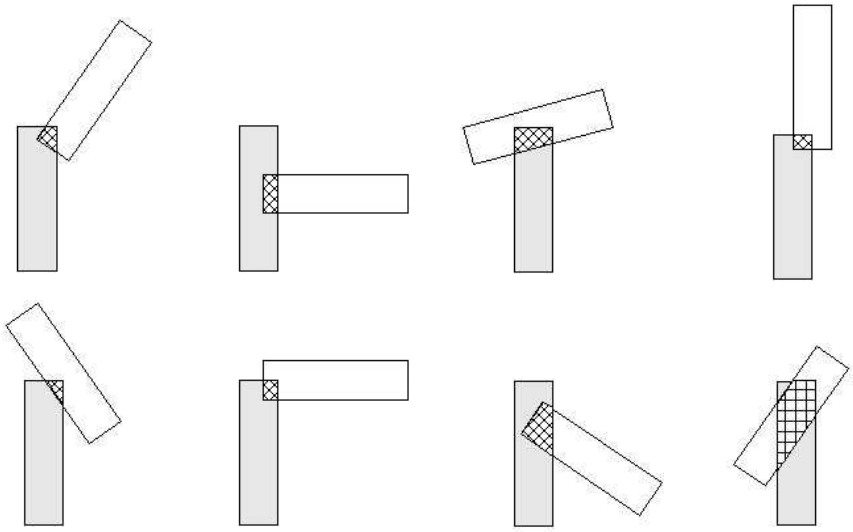

Figure A.2: The figures sketch some of the possible overlapping scenarios. Notice that a side of the particle located at $\mathbf{x}'$ can exhibit 0, 1 or 2 intersection with the perimeter of the particles at the origin. The overlapping area can be a triangle, a rectangle or and irregular polygon.

Appendix B

Liquid crystal tensor

The apolar order in liquid crystal theory is measured through a tensor defined as [72]:

$$Q_{\alpha,\beta} = \frac{1}{N}\sum_{i=1}^{N}\left(\frac{3}{2}u_{i,\alpha}u_{i,\beta} - \frac{1}{2}\delta_{\alpha,\beta}\right),\ \alpha,\beta = x,y,z \tag{B.0.1}$$

where $\mathbf{u}_i$ represents the orientation of the long axis of particle i, N is the number of particles, and $\delta_{\alpha,\beta}$ is the Kronecker delta function. Notice $Q_{\alpha,\beta}$ is symmetric and traceless. Diagonalization of $Q_{\alpha,\beta}$ gives three eigenvalues λ_+, λ_0 and λ_- such that $\lambda_+ > \lambda \geq \lambda_-$ which sum to zero. The scalar order parameter corresponds to the maximum eigenvalue of $Q_{\alpha,\beta}$, i.e., λ_+. The director is the eigenvector associated to that eigenvalue.

$Q_{\alpha,\beta}$ specialized for two-dimensional system takes the form:

$$\mathbf{Q} = \begin{pmatrix} 3/(2N)\sum\cos^2(\theta_i) - 1/2 & 3/(2N)\sum\cos(\theta_i)\sin(\theta_i) & 0 \\ 3/(2N)\sum\cos(\theta_i)\sin(\theta_i) & 3/(2N)\sum\sin^2(\theta_i) & 0 \\ 0 & 0 & -1/2 \end{pmatrix} \tag{B.0.2}$$

The eigenvalues are obtained by solving $det\left[\mathbf{Q} - \lambda\mathbf{I}\right] = 0$, where $\mathbf{I}$ is the identity matrix. The characteristic polynomial reads:

$$det\left[\mathbf{Q} - \lambda\mathbf{I}\right] = -(1/2+\lambda)\left[(a-(1/2+\lambda))(b-(1/2+\lambda)) - c^2\right] \tag{B.0.3}$$

where $a = 3/(2N)\sum_{i=1}^{N}\cos^2(\theta_i)$, $b = 3/(2N)\sum_{i=1}^{N}\sin^2(\theta_i)$ and $c^2 = \sum_{i,j=1}^{N}\cos(\theta_i)\sin(\theta_i)\cos(\theta_j)\sin(\theta_j)$. It can be easily verified that the roots are: $\lambda_- =$

$-1/2$, $\lambda_0 = \left[3/2 - \sqrt{9/4 - 4q}\right]/2 - 1/2$ and $\lambda_+ = \left[3/2 + \sqrt{9/4 - 4q}\right]/2 - 1/2$, where $q = a.b - c^2$. In consequence, λ_+ takes the form:

$$\lambda_+ = \frac{1}{4} + \frac{3}{2}\left[\frac{1}{4} - \frac{1}{N^2}\sum_{i,j=1}^{N}\left(\cos^2(\theta_i)\sin^2(\theta_j) - \cos(\theta_i)\sin(\theta_i)\cos(\theta_j)\sin(\theta_j)\right)\right]^{1/2}.$$

It can be easily verified that in the ordered case, e.g., when $\theta_i = 0$ for all i, $a = 3/2$, $b = c = 0$, and so $\lambda_+ = 1$. In the disordered case, i.e., when all orientations are equally probable, $a = b = 3/4$, $c = 0$, and so $\lambda_+ = 1/4$.

Appendix C

Numerical integration scheme for integro-PDE

The numerical integration of the integro-partial differential equation (5.2.6) requires to perform the numerical integration of Eq. (5.2.4) to then proceed to the integration of the diffusive and advective terms in Eq. (5.2.6).

At each time step $F_\Omega(\theta, t)$ is calculated through a simple Newton-Cotes method. Then the integration of Eq. (5.2.6) is performed through an operator splitting method. The diffusion is implemented by an explicit forward method. The integration of the active turning (Eq. (5.2.4)) contained in the advective term requires special attention. Since F_Ω depends explicitly on θ and t neither a Lax nor an Upwind method gives a satisfactory result. We overcame this difficulty by implementing the following variant of the Upwind method:

$$\begin{aligned} C(\theta_k, t_j + 1) = (1 - |\widetilde{F}_\Omega(\theta_k, t_j)|)C(\theta_k, t_j) + \\ \Theta(\widetilde{F}_\Omega(\theta_k - 1, t_j))|\widetilde{F}_\Omega(\theta_k - 1, t_j)|C(\theta_k - 1, t_j) + \\ \Theta(-\widetilde{F}_\Omega(\theta_k + 1, t_j))|\widetilde{F}_\Omega(\theta_k + 1, t_j)|C(\theta_k + 1, t_j) \end{aligned} \tag{C.0.1}$$

where θ_k and t_j represent the discrete indices of the angular and temporal variables respectively, $\Theta(x)$ denotes a Heaviside function, and $\widetilde{F}_\Omega(\theta_k, t_j)$ is defined as $\widetilde{F}_\Omega(\theta_k, t_j) = (\Delta t/\Delta\theta)F_\Omega(\theta_k, t_j)$ where $\Delta\theta$ and Δt are the discretization of the space and time respectively.

Bibliography

[1] U. Thiele, K. John, and M. Bär, Phys. Rev. Lett. **93**, 027802 (2004).

[2] Y. Sumino, N. Magome, T. Hamada, and K. Yoshikawa, Phys. Rev. Lett. **94**, 068301 (2005).

[3] L. Pismen, Phys. Rev. E **74**, 041605 (2006).

[4] Y. Sumino *et al.*, Phys. Rev. E **72**, 041603 (2005).

[5] A. Czirók, K. Schlett, E. Madarász, and T. Vicsek, Phys. Rev. Lett. **81**, 3038 (1998).

[6] L. Cameron, J. Robbins, M. Footer, and J. Theriot, Mol. Biol. Cell **15**, 2312 (2004).

[7] D. Selmeczi *et al.*, Biophys. J. **89**, 912 (2005).

[8] N. Kumar, M. Zaman, H. Kim, and D. Lauffenburger, Biophys. J. **91**, L32 (2006).

[9] X.-L. Wu and A. Libchaber, Phys. Rev. Lett. **84**, 3017 (2000).

[10] F. Schweitzer, W. Ebeling, and B. Tilch, Phys. Rev. Lett. **80**, 5044 (1998).

[11] F. Schweitzer, W. Ebeling, and B. Tilch, Phys. Rev. E **64**, 021110 (2001).

[12] F. Schweitzer, *Brownian Agents and Active Particles* (Springer, Berlin, 2003).

[13] G. Sibona, Phys. Rev. E **76**, 011919 (2007).

[14] B. Lindner, New J. Physics **9**, 136 (2007).

[15] G. Uhlenbeck and L. Ornstein, Phys. Rev. **36**, 823 (1930).

[16] O. Benichou *et al.*, Phys. Rev. E **74**, 020102(R) (2006).

[17] N. Komin, U. Erdmann, and L. Schimansky-Geier, Fluct. Noise Lett. **4**, L151 (2004).

[18] U. Erdmann *et al.*, arXiv:q-bio **0404018v2**, (2004).

[19] G. Viswanathan *et al.*, Nature (London) **381**, 413 (1996).

[20] R. Dickinson and R. Tranquillo, AIChE J. **39**, 1995 (1993).

[21] M. Krieger, J. Billeter, and L. Keller, Nature (London) **406**, 992 (2000).

[22] E.Fiorelli *et al.*, Proc. IEEE **AUV04**, 1 (2004).

[23] A. Jadbabaie, J. Lin, and A. Morse, IEEE Trans. on Automatic Control **48**, 988 (2003).

[24] D. Helbing, Rev. Mod. Phys. **73**, 1067 (2001).

[25] D. Helbing, I.Farkas, and T.Vicsek, Nature (London) **407**, 487 (2000).

[26] J. Parrish and W. Hamner, *Three Dimensional Animals Groups* (Cambridge University Press, Cambridge, 1997).

[27] L. Jelsbak and L. Sogaard-Andersen, Proc. Natl. Acad. Sci. USA **99**, 2032 (2002).

[28] R. Welch and D. Kaiser, Proc. Natl. Acad. Sci. USA **98**, 14907 (2001).

[29] Y. Harada, A. Noguchi, A. Kishino, and T. Yanagida, Nature (London) **326**, 805 (1987).

[30] Y. Toyoshima *et al.*, Nature (London) **328**, 536 (1987).

[31] S. Ramaswamy, R. Simha, and J. Toner, Europhys. Lett. **62**, 196 (2003).

[32] K. Kruse *et al.*, Eur. Phys. J. E **16**, 5 (2005).

[33] N. Mermin and H. Wagner, Phys. Rev. Lett. **17**, 1133 (1966).

[34] T. Vicsek *et al.*, Phys. Rev. Lett. **75**, 1226 (1995).

[35] A. Czirok, E. Ben-Jacob, I. Cohen, and T. Vicsek, Phys. Rev. E **54**, 1791 (1995).

[36] J. Toner and Y. Tu, Phys. Rev. E **58**, 4828 (1998).

[37] E. Bonabeau, G. Theraulaz, V. Fourcassie, and J. Deneubourg, Phys. Rev. E **57**, 4568 (1998).

[38] E. Ben-Jacob, I. Cohen, and D. Gutnick, Annual Review of Microbiology **52**, 779 (1998).

[39] J. Buhl *et al.*, Science **312**, 1402 (2006).

[40] G. Gregoire, H. Chate, and Y. Tu, Physica D **181**, 147 (2003).

[41] G. Gregoire and H. Chate, Phys. Rev. Lett. **92**, 025702 (2004).

[42] J. Toner and Y. Tu, Phys. Rev. Lett. **75**, 4326 (1995).

[43] N. S. K. Sugawara, T. Mizuguchi, Y. Hayakawa, and M. Sano, Phys. Rev. Lett. **76**, 3870 (1996).

[44] H. Bussemaker, A. Deutsch, and E. Geigant, Phys. Rev. Lett. **78**, 5018 (1997).

[45] H. Levine, W.-J. Rappel, and I. Cohen, Phys. Rev. E **63**, 017101 (2001).

[46] E. Ben-Jacob, I. Cohen, and H. Levine, Adv. Phys. **49**, 395 (2000).

[47] M. Dworkin and D. Kaiser, *Myxobacteria II* (American Society for Microbiology, Washington DC, 1993).

[48] H. Chate, F. Ginelli, and R. Montagne, Phys. Rev. Lett. **96**, 180602 (2006).

[49] S. Mishra and S. Ramaswamy, Phys. Rev. Lett. **97**, 090602 (2006).

[50] V. Narayan, S. Ramaswamy, and N. Menon, Science **317**, 105 (2007).

[51] D. Bray, *Cell movements: from molecules to motility*, 2nd ed. (Garland Publishing, New York, 2001).

[52] W. Ebeling and I. Sokolov, *Statistical thermodynamics and stochastic theory of non-equilibrium systems* (World Scientific, Singapore, 2005).

[53] H. Othmer, S. Dunbar, and W. Alt, J. Math. Biol. **26**, 263 (1988).

[54] A. Mikhailov and D. Mainkoehn, in *Stochastic Dynamics*, edited by L. Schimansky-Geier and T. Poeschel (Springer, Berlin, 1997), Vol. LNP 484, p. 169.

[55] M. Schienbein, K. Franke, and H. Gruler, Phys. Rev. E **49**, 5462 (1994).

[56] I. Schneider and J. Haugh, J. Cell Biol. **171**, 883 (2006).

[57] S. Huang, X. Zou, and Z. Jin, Phys. Rev. E **65**, 52105 (2002).

[58] C. Tojo and P. Argyrakis, Phys. Rev. E **54**, 58 (1996).

[59] C. Bracher, Physica A **331**, 448 (2004).

[60] H. Risken, *The Fokker-Planck equation* (Springer, Berlin, 1989).

[61] G. Viswanathan *et al.*, Phys. Rev. E **72**, 011111 (2005).

[62] J.-F. Joanny, F. Jülicher, and J. Prost, Phys. Rev. Lett. **90**, 168102 (2003).

[63] A. Ponti *et al.*, Science **305**, 1782 (2004).

[64] O. Igoshin, R. Welch, D. Kaiser, and G. Oster, Proc. Natl. Acad. Sci. USA **101**, 4256 (2004).

[65] M. Alber, M. Kiskowski, and Y. Jiang, Phys. Rev. Lett. **93**, 068102 (2004).

[66] D. Dusenbery, Journal of Bacteriology **180**, 5978 (1998).

[67] D. Dusenbery, Proc. Natl. Acad. Sci. USA **94**, 10949 (1997).

[68] J. Mitchell, Microb. Ecol. **22**, 227 (1991).

[69] J. Mitchell, Am. Nat. **160**, 727 (2002).

[70] R. Kemkemer *et al.*, Eur. Phys. J. E **3**, 101 (2000).

[71] L. Onsager, Ann. N. Y. Acad. Sci. **51**, 627 (1949).

[72] M. Doi and S. Edwards, *The Theory of Polymer Dynamic* (Clarendon Press, Oxford, 1986).

[73] U. Börner, A. Deutsch, H. Reichenbach, and M. Bär, Phys. Rev. Lett. **89**, 078101 (2002).

[74] H. Reichenbach, *Myxobacteriales: Schwarmentfaltung und Bildung von Protocysten* (Institut fuer den wissenschaftlichen Film, Goettingen, 1966).

[75] H. Reichenbach, Ber. Dtsch. Bot. Ges. **78**, 102 (1965).

[76] A. Levine, T. Liverpool, and F. MacKintosh, Phys. Rev. E **69**, 021503 (2004).

[77] A. Levine, T. Liverpool, and F. MacKintosh, Phys. Rev. Lett. **93**, 038102 (2004).

[78] N. Kampen, *Stochastic Processes in Physics and Chemistry* (North Holland, Amsterdam, 1981).

[79] F. Reif, *Fundamentals of Statistical and Thermal Physics*, international edition ed. (McGraw-Hill, Singapore, 1985).

[80] A. Okubo, Adv. Biophys. **22**, 1 (1986).

[81] E. Buckingham, Phys. Rev. **4**, 345 (1914).

[82] S. Chandrasekhar, Rev. Mod. Phys. **15**, 1 (1943).

[83] A. S. (Ed.), *Encyclopedia of nonlinear science* (Taylor and Francis Group, New York, 2005).

[84] F. Family and D. L. (Eds.), *Kinetics of Aggregation and Gelation* (Elsevier Science, Amsterdam and New York, 1984).

[85] P. Flory, *Principles of Polymer Chemistry* (Cornell University Press, Ithica, 1953).

[86] H. Galina and J. Lechowicz, Advances in Polymer Science **137**, 135 (1998).

[87] F. Leyvraz, Phys. Rep. **383**, 95 (2003).

[88] J. Norris, Annals of Applied Probability **9**, 78 (1999).

[89] P. van Dongen and M. Ernst, J. Stat. Phys. **50**, 295 (1988).

[90] R. Kayser and J. Raveche, Phys. Rev. A **17**, 2067 (1978).

[91] A. Ahmadi, T. Liverpool, and M. Marchetti, Phys. Rev. E **72**, 060901(R) (2005).

[92] T. Liverpool and M. Marchetti, Phys. Rev. Lett. **97**, 268101 (2006).

[93] B. Szabó *et al.*, Phys. Rev. E **74**, 061908 (2006).

[94] R. Voituriez, J. Joanny, and J. Prost, Phys. Rev. Lett. **96**, 028102 (2006).

[95] K. Kruse *et al.*, Phys. Rev. Lett. **92**, 078101 (2004).

[96] D. Helbing, I. Farkas, and T. Vicsek, Phys. Rev. Lett. **77**, 2129 (1996).

[97] A. Sokolov, I. Aranson, J. Kessler, and R. Goldstein, Phys. Rev. Lett. **98**, 158102 (2007).

[98] J. Bonner, Proc. Natl. Acad. Sci. USA **95**, 9355 (1998).

[99] M. Laub and W. Loomis, Mol. Biol. Cell **9**, 3521 (1998).

[100] F. Peruani, A. Deutsch, and M. Bär, Phys. Rev. E **74**, 030904(R) (2006).

[101] P. Lebwohl and G. Lasher, Phys. Rev. A **6**, 426 (1972).

[102] M. Nagy, I. Daruka, and T. Vicsek, Physica A **373**, 445 (2007).

[103] M. Aldana *et al.*, Phys. Rev. Lett. **98**, 095702 (2007).

[104] J. Kosterlitz and D. Thouless, J. Phys. C **6**, 1181 (1973).

[105] J. Kosterlitz, J. Phys. C **7**, 1146 (1974).

[106] P. Archambault *et al.*, J. Appl. Phys. **83**, 7234 (1998).

[107] M. C. Largomasino, M. Dogterom, and M. Dijkstra, J. Chem. Phys. **112**, 10034 (2000).

[108] F. Peruani and L. Morelli, Phys. Rev. Lett. **99**, 010602 (2007).

[109] L. Tsimring *et al.*, Phys. Rev. Lett. **75**, 1859 (1995).

[110] M. Brenner, L. Levitov, and E. Budrene, Biophys. J. **74**, 1677 (1998).

[111] H. Riedel, K. Kruse, and J. Howard, Science **309**, 300 (2005).

[112] F. Nédélec, T. Surrey, A. Maggs, and S. Leibler, Nature (London) **389**, 305 (1997).

[113] Y. Tu, J. Toner, and M. Ulm, Phys. Rev. Lett. **80**, 4819 (1998).

[114] E. Bertin, M. Droz, and G. Grégoire, Phys. Rev. E **74**, 022101 (2006).

[115] S. Strogatz, Physica D **143**, 1 (2000).

[116] A. Mogilner and L. Edelstein-Keshet, Physica D **89**, 346 (1996).

Eidesstattliche Versicherung

Hiermit versichere ich an Eides statt, daß ich die vorliegende Arbeit ohne unzulässige Hilfe Dritter und ohne Benutzung anderer als der angegebenen Hilfsmittel angefertigt habe; die aus fremden Quellen direkt oder indirekt übernommenen Gedanken sind als solche kenntlich gemacht. Die Arbeit wurde bisher weder im Inland noch im Ausland in gleicher oder ähnlicher Form einer anderen Prüfungsbehörde vorgelegt.

Die vorliegende Doktorarbeit wurde am Max-Planck-Institut für Physik komplexer Systeme (Dresden), an der Technischen Universität Dresden, und an der Physikalischen Technische Bundesanstalt angefertigt und vom Prof. Dr. Markus Bär betreut.

Die Promotionsordnung der Technischen Universität Berlin wird anerkannt.

Fernando M. Peruani San Román